Jet mixing noise model based on geometrical acoustics for the prediction of installation effects

Yann Martelet

N° d'ordre NNT: 2020LYSEC12

THÈSE de DOCTORAT DE L'UNIVERSITÉ DE LYON
opérée au sein de l'École Centrale de Lyon

École Doctorale N° 162
Mécanique Énergétique Génie Civil Acoustique

Spécialité de doctorat : Acoustique

Soutenue publiquement le 05/03/2020, par
Yann Martelet

Jet mixing noise model based on geometrical acoustics for the prediction of installation effects

---

Devant le jury composé de:

Bailly, Christophe	Professeur	École Centrale de Lyon	Directeur de thèse
Balin, Nolwenn	Ingénieure	AIRBUS	Examinatrice
Bodard, Guillaume	Ingénieur	SAFRAN	Invité
Gervais, Yves	Professeur	Université de Poitiers	Président du jury
Ghorbaniasl, Ghader	Professeur	Vrije Universiteit Brussel	Rapporteur
Huet, Maxime	Ingénieur de recherche	ONERA	Examinateur
Miller, Steven A. E.	Professeur assistant	University of Florida	Rapporteur

Résumé

Un modèle de prédiction du bruit de jet de mélange est développé dans l'objectif d'obtenir une estimation précise des effets de l'installation du moteur sur l'aile tout en maintenant un temps de calcul faible. Le modèle de prédiction de Tam et Auriault est utilisé comme point de départ. L'écoulement est simplifié en assimilant le jet à un milieu uniforme connecté au milieu ambiant, lui aussi uniforme, par une couche de mélange infiniment mince. La propagation des ondes sonore depuis le jet jusqu'à un observateur situé en champ lointain est ici simulée grâce à l'acoustique géométrique, utilisée dans ce milieu homogène par morceau. Le nouveau modèle est nommé TAGA pour Tam Auriault - Geometrical Acoustics.

Le modèle TAGA est d'abord appliqué sur un cas académique, un jet simple sans gradient de température, placé à proximité d'une plaque plane. Le bruit de jet est prédit sur toute la gamme d'azimut, à un plan axial coïncidant avec la sortie de la tuyère. Moyennant une correction sur le niveau absolu, les résultats obtenus pour les microphones situés sous la plaque correspondent aux données expérimentales. Pour des observateurs positionnés au dessus de la plaque, les prédictions sont proches des mesures pour la gamme de fréquence correspondant au maximum du spectre. L'effet de masquage de la plaque est surestimé pour les plus hautes fréquences. Les résultats avec TAGA sont ensuite présentés d'une manière différente. La différence entre les spectres installés et isolés est ajoutée au spectre isolé mesuré. Cette méthode de mise à l'échelle permet d'obtenir une forme de spectre plus fidèle aux mesures. Un écart maximal, entre les prédictions et les données expérimentales, de 1 dB pour toutes les fréquences au dessus de 1 kHz est obtenu. L'étude permet aussi la compréhension d'un pic secondaire observé dans les mesures. Ce phénomène est effectivement expliqué par l'interférence entre des rayons réfractés et réfléchis.

Une seconde étude est menée sur un jet coaxial. Le cône de silence dû aux effets de réfraction est observé à une valeur proche de sa position théorique. Malgré les différences entre l'écoulement réel et sa modélisation dans TAGA, des résultats encourageants sont observés pour une large partie de la plage d'angles polaires. La méthode de mise à l'échelle est aussi utilisée pour la prédiction des effets de chevrons. L'augmentation du bruit à haute fréquence est bien estimée par le modèle TAGA. La réduction à basse fréquence n'est pas obtenue avec la formulation actuelle du modèle.

Mots clés : bruit de jet; acoustique géométrique; effets d'installation.

Abstract

A jet mixing noise prediction model is developed with the objective of obtaining an accurate estimate of installation effects while maintaining a low computing time. The Tam and Auriault prediction model is used as a starting point for the source term of the new formulation. The base flow is simplified by modelling the jet as a uniform medium connected to a uniform external medium through an infinitely thin mixing layer. The propagation of sound waves from the jet to an observer located in the far field is here simulated using geometrical acoustics. The new model developed is called TAGA for Tam Auriault - Geometrical Acoustics.

The TAGA model is first applied to an academic configuration, a single jet without temperature gradient placed near a flat plate. Jet noise is predicted over the entire azimuth range, at an axial plane coinciding with the nozzle outlet. With an absolute level correction, the results obtained for the microphones under the plate match the experimental data. For observer positions above the plate, the predictions are close to measurements for the frequency range corresponding to the maximum of the spectrum. The shielding effect of the plate is however overestimated for the highest frequencies. The TAGA results are then reported in a different way. The difference between the installed and isolated spectra is added to the measured isolated spectrum. This scaling method allows a more accurate spectrum shape to be obtained. A maximum deviation, between predictions and experimental data, of 1 dB for all frequencies above 1 kHz is then obtained. The study also allows to understand a secondary peak observed in the measurements. This phenomenon is indeed explained by the interference between refracted and reflected rays.

A second study is conducted on a coaxial jet. The cone of silence due to refraction effects is observed at a value close to its theoretical position. Despite the differences between the jet flow and its modelling in TAGA, encouraging results are observed for a large part of the polar angle range. The scaling method is also used to predict chevrons effects. The increase in high frequency noise is well estimated by the TAGA model. The reduction at low frequency is not found by the current formulation of the model.

Keywords : jet noise; geometrical acoustics; installation effects.

Remerciements

Cette thèse a été réalisée dans le cadre d'une collaboration entre le groupe Acoustique du Laboratoire de Mécanique des Fluides et d'Acoustique (LMFA) de l'École Centrale de Lyon et le département d'acoustique d'Airbus, de février 2018 à mars 2020.

Je souhaite tout d'abord remercier mes encadrants pour leur soutien tout au long de la thèse. Merci Christophe pour tes conseils avisés et pour ta patience envers ma prose perfectible ; Greg pour ton enthousiasme contagieux, ta disponibilité et la demi-tonne de RANS utilisés ces trois ans ; Jean-Yves pour ton implication, en particulier sur la partie analytique. Je voudrais aussi remercier les personnes qui m'ont aidé quand j'en ai eu besoin: Jérôme pour les discussions sur toute la partie physique ; Nolwenn pour la prise en main d'Acti-HF et JP pour la production des CAD. Un énorme merci à Toufic, Ahmed et Kieran de IMACS pour leur investissement sur les modifications apportées au code d'Acti-HF. Votre efficacité a contribué sans aucun doute à la qualité de ces travaux. J'ai aussi une pensée pour Fabien qui aura été le premier à me faire confiance et qui aura su se battre avec l'ANRT et Airbus pour monter cette CIFRE. J'en profite pour remercier le reste d'EPA6, traîtres compris, pour leur accueil et pour les gigas d'images du groupe WhatsApp qui polluent mon téléphone.

Le bon déroulement de cette thèse n'aurait pu être garanti sans le support moral de mes amis. Je remercie d'abord ceux qui me suivent depuis 10, 15 ou même 20 ans, la belle population du Dolbistan. Merci Alex, Jérôme, Jonathan, Julien, Nicolas et Romain. Je ne sais honnêtement pas par où commencer, merci d'être là chaque jour malgré la distance et merci d'être aussi bêtes que moi. Je remercie aussi le pentanôme version TGGS: Zgaygsou, Jospeh et Dr Lulux. Merci pour les soirées Fifafou, les maillots moches et votre nullité à l'EBPL. Merci aussi à Ceschito, dernier membre du pentanôme, pour la garde de la fameuse bouteille de vin ; Secoach pour la perte d'audition partielle dans mon oreille droite et à Olivier pour la confiture. Merci aux tenanciers de l'Ibis Lapujade, Joanne et Thomas, pour tous les weekends à Toulouse et au reste de la team Gorgonzola qui répond toujours présent pour une petite bière (avec ou sans marathon) quand je suis de passage dans la ville rose.

Je tiens aussi à remercier mes "collègues" doctorants et post-doctorants de m'avoir supporté, dans tous les sens du terme, pendant ces 3 ans. Merci au coach Simon pour les séances Berthom (toujours pas remboursées par la sécu) ; Damien pour sa fascination pour l'anthropologie ; mon cher camarade croix-roussien Pierre pour nos soirées Pinte Douce (RIP) hebdomadaires. Merci Étienne pour ces précieuses discussions sur le bruit de jet (Jones!) et sur la plume de notre

ami Chris, une partie de la qualité de cette thèse t'est due. Danny, j'avais un truc spécial pour toi, malheureusement j'ai pas trouvé le package LaTeXpour insérer les emojis. Merci Léo, mon partenaire de limbo ; Elina, je te taquine mais c'était pas si mal de partager le bureau avec toi ; Ariane qui m'aura appris qu'il n'y avait pas de haine chez elle, d'ailleurs désolé pour mes métaphores filées ; Mathieu qui aura été plus assidu sur l'apprentissage de la pissette que l'entretien de la machine à café ; Mohcene, le futur du ski algérien et Gabriele, le plus grand fan des gâteaux du vendredi. Efkharisto magka mou. Merci Vianney qui contre toute attente n'est pas parti construire des murs à Tahiti, au passage, désolé pour la quiche lorraine ; Marion qui n'aura pas pris assez de bulles au baby. Merci Bertrand pour les debriefs Top Chef ; Paul pour sa finesse en défense ; Miguel pour les péniches et Rafael, le Usain Bolt portugais, pour les sprints. Merci David d'avoir pris soin de mon portable et Thomas d'avoir été mon partenaire de Fifalcool, dans les défaites comme les matchs nuls. Merci aussi à ceux que je n'ai pas eu la chance de plus côtoyer: Thomas, Yuanyuan, Antoni, Jean, Courtney et Sarah. Et pour finir, merci Maxime, petit ange parti trop tôt rejoindre les (rm) étoiles.

Je remercie enfin mes parents, mon frère et ma sœur qui continuent d'être là pour moi, épreuves après épreuves.

J'veux du taga pour mon anniv'

VALD

Contents

Nomenclature

Acronyms

CHE	Convected Helmholtz equation
DES	Detached Eddy Simulation
DNS	Direct Numerical Simulation
LEE	Linearised Euler equation
LES	Large Eddy Simulation
PSD	Power Spectral Density
RANS	Reynolds-Averaged Navier-Stokes
TAGA	Tam Auriault Geometrical Acoustics

Greek characters

$\bar{\rho}$	Mean density
$\bar{\tau}_{ij}$	Viscous stress tensor
ϵ	Turbulent dissipation
γ	Specific heat ratio
μ_t	Turbulent dynamic viscosity
ω	Pulsation
τ_s	Decay time of the fine scale turbulence
θ	Polar angle in the cylindrical frame centered on the nozzle exit plane

Latin characters

$\bar{u}_i$	Mean velocity components
$\hat{p}'^a$	Adjoint Green pressure fluctuations in the Fourier domain

$\hat{u}'^a$	Adjoint Green fluctuating velocity in the Fourier domain
$\tilde{q}_s$	Measure of the intensity of the fluctuation of the kinetic energy of the fine scale turbulence
k_s	Kinetic energy of the fine scale turbulence
k_t	Turbulent kinetic energy
l_s	Length scale of the fine scale turbulence
p	Pressure
p'	Pressure fluctuations
$p'^{(n)}$	Green pressure fluctuations
p_{ref}	Pressure of reference
q_s	Source term driven by the fine scale turbulence
S	Pressure power spectral density
S_{ij}	Deformation tensor
t	Time
$u'^{(n)}$	Green fluctuating velocity
u'_i	Fluctuating velocity components

Superscripts

$'$	Superscript relative to the fluctuating part
$''$	Superscript relative to the Favre fluctuating component
^{a}	Superscript relative to an adjoint Green function
$^{(n)}$	Superscript relative to a Green function

Subscripts

$_M$	Subscript relative to an observer
$_S$	Subscript relative to a source
$_s$	Subscript relative to the the fine scale turbulence

Other

$\bar{}$	Time-average
$\hat{}$	Fourier transform
$\tilde{}$	Favre average component

1 Introduction

1.1 Context of the study

With the development of air traffic, new challenges arose for aircraft manufacturers, and topics that were once put in the background are now driving the engineering process. Among these new problems features the field of acoustics. The ever growing number of flights created a noise pollution issue in the vicinity of airports and led to the creation of thresholds for aircraft noise emission. An evolution of the tightening of the certification process for new aircrafts is presented in Fig 1.1 reproduced from [30]. The objective is to pursue this trend with goals set by FlightPath 2050 [26] of a reduction by 65% of the perceived noise level compared to the standards from 2000.

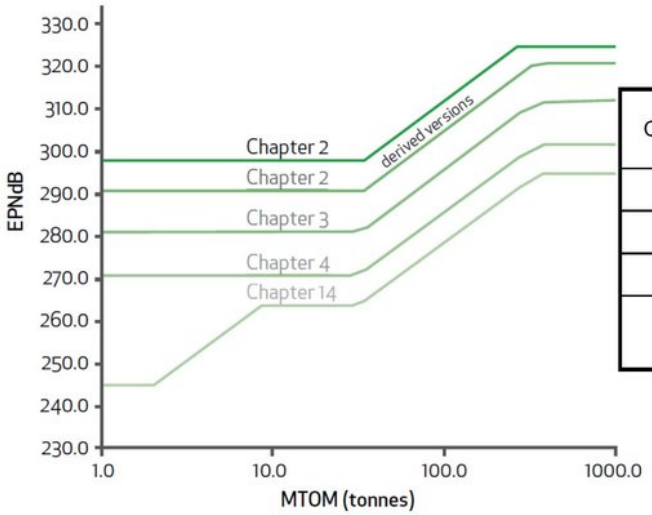

Chapter	Applicable Year	Cum Margin (EPNdB)
2	1972	Ch. 3 ~-16
3	1978	0 (Ref)
4	2006	Ch. 3 +10
14	2017 & 2020	Ch. 3 +17 (Ch. 4 +7)

Figure 1.1: Evolution of the legislation on total aircraft noise, from [30].

Three certification positions were introduced to evaluate the noise generated by an aircraft, as depicted in Fig 1.2. The sideline certification point corresponds to the maximum of the recording at a microphone located 450 m from the runway axis during take-off. The flyover certification point (or cutback) is located 6.5 km away from the brake release point, under the take-off flight path. The approach certification point is set 2 km away from the runway threshold, under the approach flight path. These operating conditions correspond to characteristic flight steps and accurately display the different noise components contained in the total aircraft noise spectrum.

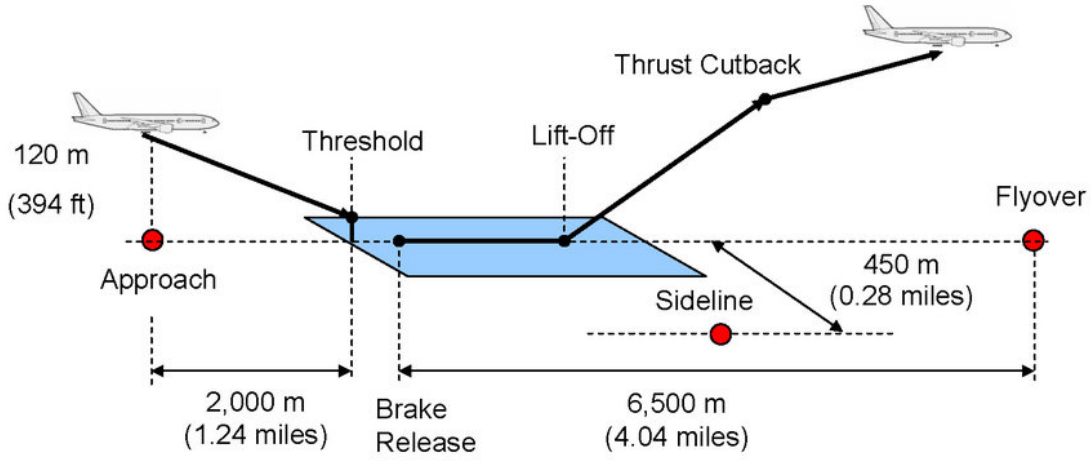

Figure 1.2: Noise certification points, from [45].

Successive improvements on the engines allowed a 23 dB reduction of the total aircraft noise in 50 years [54]. An example of such improvements is the use of turbofan engines which, thanks to a secondary flow, can generate a given thrust with slower jet. The reduction in jet speed decreases turbulence intensity in the mixing layer between the jet plume and the external flow and thus cuts down jet noise. These new geometries also increased the variety of the noise generation mechanism linked to the engine as well as their relative weight. The main impact has been the introduction of fan noise. A distribution of the noise production between these different mechanisms at the three certification points listed above is presented in Table 1.1. This decomposition shows that even though the new generation of engines has reduced the jet noise, it remains a dominant contribution at take-off.

	Approach	Flyover	Sideline
Jet	0 %	20 %	40 %
Combustion	5 %	30 %	20 %
Turbine	10 %	0 %	0 %
Forward fan	45 %	15 %	5 %
Rearward fan	40 %	35 %	35 %

Table 1.1: Distribution of the different noise contributions for a typical CFMI engine, from [24].

The evolution in engine geometries and the emergence of disruptive technologies have boosted research activities in aeroacoustics. Three related objectives drive the scientific community, namely the need of a global understanding of the different noise generating mechanisms, the development of noise reduction techniques and of noise prediction methods. Aircraft manufacturers do not produce the engines themselves but are responsible of their integration into the aircraft and are accountable for the aircraft noise to the airworthiness authorities. In that context, the development of accurate noise prediction methods constitutes a real challenge.

Research in jet noise prediction began in 1952 with the publication of the first acoustic analogy by Lighthill [46]. Since then, the understanding of this noise component has been pushed to

new heights, especially so with the advancement of technology in both the experimental and computational domains. The increased comprehension of turbulent flows allowed the identification of several sub-mechanisms in jet noise each driven by particular flow factors and each featuring specific spectral features. But although this domain of acoustics has come a long way over the last 70 years, a lot remains to be understood. Nowadays, researchers rely on jet flow simulations of ever growing complexity to gain access to previously unavailable details. Despite the advancement of modern computers, the escalation of simulation's complexity is still followed by a rise of the restitution time and overall cost. This evolution, however, does not fit the industrial requirements. Engine and aircraft manufacturers therefore need to bring forward methods that can find the best ratio between precision and cost. This issue is addressed in this thesis with the development and the validation of a new jet mixing noise prediction model.

1.2 Outline of the manuscript

The document is organised as follows. The second Chapter first presents the jet mixing noise from fine scale turbulence and the specifications set by Airbus for the desired method. A review of the literature on prediction models of the range of interest is then given. Acoustic analogies are described, highlighting the similarities in the final expression of the power spectral density in each case and in particular the presence of two key elements: the source modelling and a term accounting for the propagation. An overview of the different methods available in the literature for the statistical modelling of the source terms is given along with the commonly used inputs. In a second time the propagation of the sound waves is addressed with the introduction of several methods. In particular, the degree of details included in each of them and their restitution time are discussed. Finally, the choices made for the modelling of the sources and the computation of the propagation are given and argued.

The third Chapter contains the mathematical derivation of the equations allowing the computation of the noise spectrum. This part is built around three sections. The first one presents the outline of the CFD/CAA method. The objective is to have a pragmatic understanding of the main elements composing the model before they are analytically derived. The fine scale jet mixing noise model by Tam and Auriault [78] is used as a stepping stone and is therefore analysed and redeveloped in details in the second section. A simplified propagation medium is then introduced to allow for a faster computation of sound wave propagation. The last section explains how the work from Tam and Auriault can be applied to this new flow description and the calculations needed to obtain an expression of the power spectral density are provided.

The different validation studies and application cases performed during the PhD are reported in the fourth Chapter. A first part addresses the practical implementation of the model and in particular the reduction of the continuous propagation medium into two homogeneous parts. The ray tracing tool is also presented with validation elements. Two nozzles are used for the assessment of the accuracy of the noise prediction model. The first is a single cold jet. This configuration is

used to perform computations on the full azimuth range to validate the predictions of installation effects. The second configuration, called EXEJET, is a hot coaxial jet used to investigate the performance of the method on nozzle geometries closer to real engines. Refraction effects are first assessed before using the developed model as a scaling tool to predict the impact of chevrons on jet mixing noise.

In appendix are given reminders about the theory behind Green functions and geometrical acoustics. Parts of the calculations judged too tedious to remain in the main body are also provided. Finally, data regarding the RANS inputs and the full noise predictions are presented.

1.3 Notations convention

A brief explanation of the notations used throughout the manuscript is given below to ensure clarity of the equations later discussed in the thesis.

The presence of the arrow above the character denotes a vector. Its coordinates are given without an arrow but with the corresponding axis as a subscript. Moreover, the role of these vectors is indicated with a subscript. Note that this subscript is not provided in the coordinates to keep the notations light. An S means that it is the location of a source point while an M indicates that it refers to an observer location. This way, we can introduce a source point at $\vec{\xi}_S$ with the following coordinates in a polar frame $(\xi_x, \xi_r, \xi_\theta)$.

A few variables are also present in the equations. Their mean value is highlighted by the presence of a bar whereas their fluctuating part is indicated by the presence of an apostrophe. In the case of vectors, like the velocity, there is no arrow on top of the character but they are written in bold to differentiate them from the points. Similarly, their coordinates are given with their corresponding axis as a subscript. As an example, the mean velocity relative to the jet is noted $\bar{\mathbf{u}}_{\text{jet}}$ with the following coordinates in a generic frame $(\bar{u}_1, \bar{u}_2, \bar{u}_3)$.

Finally, Green functions are distinguishable from their corresponding variables by the presence of the superscript $^{(n)}$ where n is an integer and the superscript ^{a} in the case of adjoint Green functions. The application of a Fourier transform is indicated by the presence of a circumflex. As an illustration, the adjoint Green pressure fluctuations in the Fourier domain is noted $\hat{p}'^{a}$.

2 Statistical modelling of jet mixing noise

2.1 Jet mixing noise

As mentioned in the introduction, various noise generation mechanisms are involved in isolated jet flows. They need to be studied separately. As described by Miller [55], there is

- the jet mixing noise: This is the noise mechanism that will be considered in this thesis. This mechanism is defined by the noise generated by turbulence developing in the mixing layers between the jet and the external flow.
- the BroadBand Shock Associated Noise (BBSAN): This is the noise created by the presence of shock cells in the jet plume due to a static pressure jump between the nozzle exit and the pressure outside the nozzle. The generated noise is broadband and dominant upstream at mid to high frequencies if the Mach of the jet is high enough.
- the screech: This is a tonal noise caused by the interaction between waves impacting the nozzle exit thus creating a perturbation that will generate a second wave thus creating a feedback loop. Tones of high amplitude are thus observed in the acoustic spectra.

Power spectral densities for the total jet noise at three different locations are plotted in Figure 2.1 from Miller [55]. The different contributions are highlighted on this graph. Jet mixing noise is evidently a major contributor in jet noise and especially for subsonic jets.

An in-depth study of the jet mixing noise allows the identification of two separate mechanisms. First, there are small structures with a short lifetime. Such structures are represented in Fig 2.2. They act as compact sources and generate a broadband noise that dominates the spectrum at a polar angle of 90° and upstream as explained in Tam, Golebiowski and Seiner [80]. There is no intrinsic directivity, but propagation effects can be observed. There are also some larger structures, more coherent than the smaller ones. They exist over a longer lifetime and can be seen travelling downstream. Such structures are represented in Fig 2.3. They also generate a broadband noise but with a sharper peak centered at a slightly lower frequency. Because these structures are more coherent, they will have an intrinsic directivity. This component will dominate the spectrum mainly for an observer located downstream [80]. The focus of this study

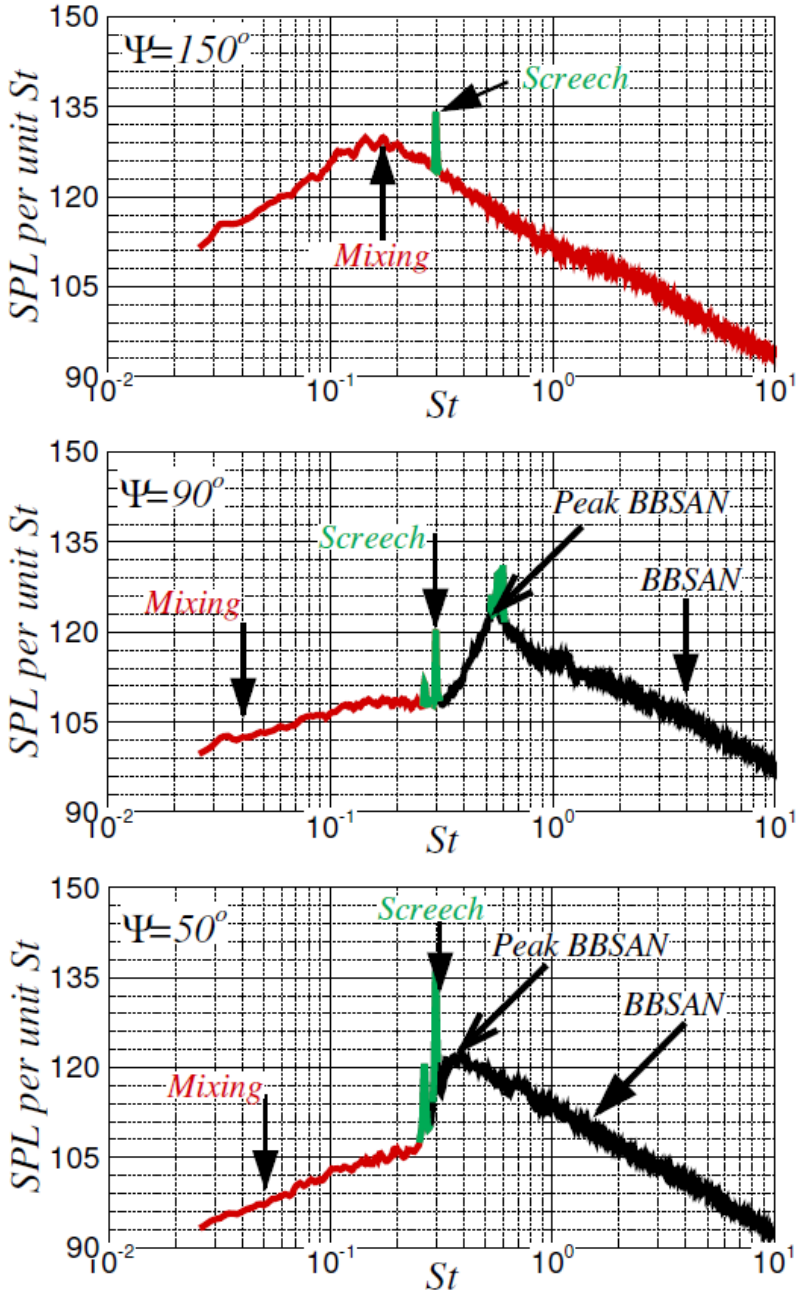

Figure 2.1: Sound pressure level per unit Strouhal number resulting from a $M_d = 1.00$, $M_j = 1.50$, and $TTR = 1.00$ jet. The red lines represent the noise that is dominated by turbulent mixing, black lines represent noise that is dominated by BBSAN, and green lines represent noise that is dominated by discrete tones (screech). Ψ is the angle from the upstream jet axis to the observer centered about the nozzle exit at $R/D = 100$. From Miller [55]

is the noise of fine scale turbulence. The dominance of these two different sources at 90° and downstream is illustrated in Fig 2.4 from [83] where the similarity spectra introduced by Tam *et al.* [80] are fitted on the experiments. The black symbols show the large scale dominated spectrum downstream and the white symbols show the fine scale dominated spectrum at 90°.

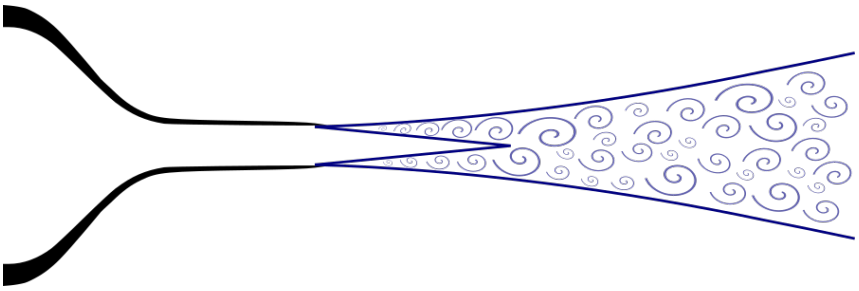

Figure 2.2: Representation of fine scale turbulent structures within a jet plume

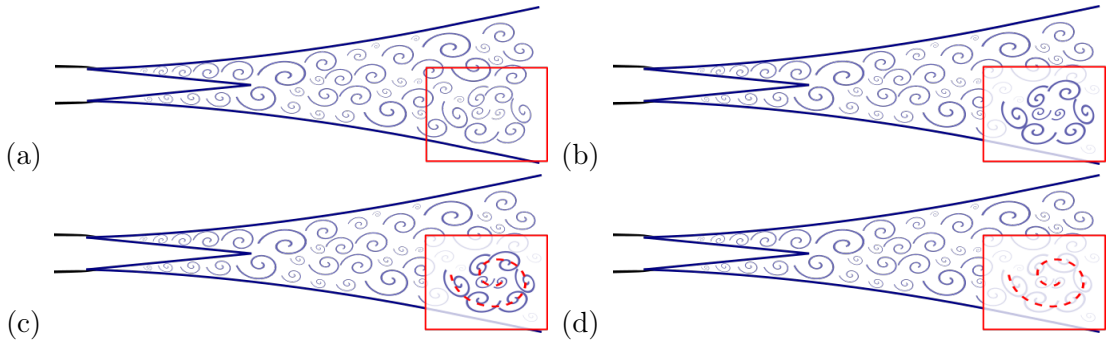

Figure 2.3: Representation of a large scale turbulent structure within a jet plume

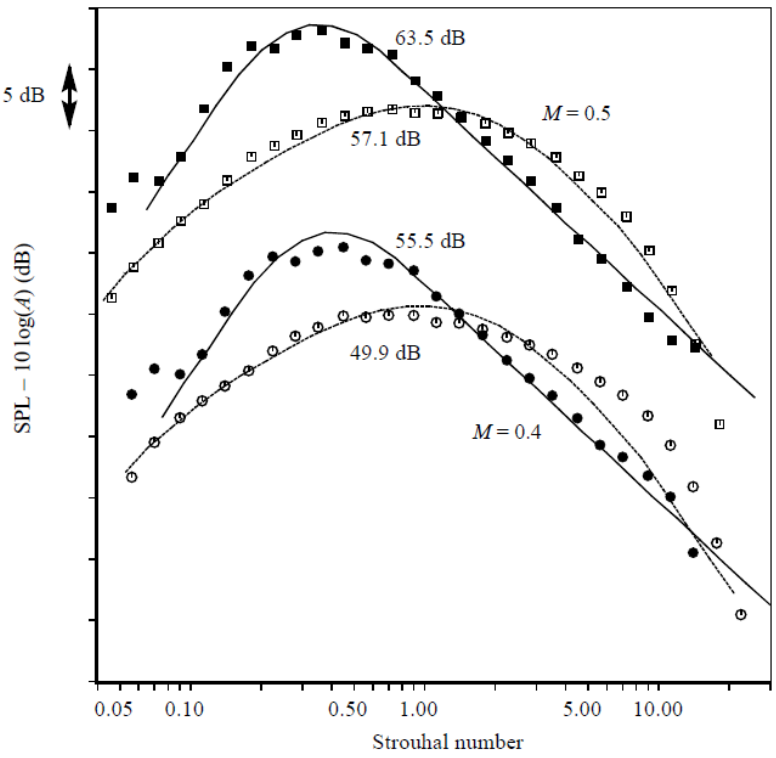

Figure 2.4: Comparison of measured spectra with similarity spectra of unheated jets. The black symbols are from measurements at 155° and the white symbols are from measurements at 90°. From Viswanathan [83]

2.2 Specifications of the prediction method

In terms of precision, the jet mixing noise prediction method should

- Take into account refraction effects caused by the propagation of the wave through the mixing layer between the jet an the external medium.
- Take also into account the possible installation effects such as reflection of acoustic waves on the wing or on the contrary its blockage, called shielding effect. In addition, the diffraction of the incident acoustic field by the wing edges should also be predicted.

This work is first of all motivated by an industrial need which means that the end product is intended to be used by Airbus engineers and thus need to comply with a few practical aspects. First, the method should allow the computation of noise predictions within a reasonable time. In practice the target for the maximum restitution time lies at around ten hours for the noise prediction, given that all the desired inputs are available. This aspect should drive the development of the method almost as much as the other precision-oriented objectives. Moreover, because the intention is to use the present work within a design loop, the nature of the input and the means necessary to obtain them should also be taken into consideration. In the framework of this thesis, the use of RANS-based prediction methods appears to be appropriate. They consist of the use of RANS CFD simulations to feed analytical and empirical models to predict the far-field noise. They give relatively accurate results compared to their limited computing needs. Because of the time-averaging of the turbulence inherent of the RANS model, the simulated turbulent field does not represent a realistic flow. This statistical description of the turbulence represents fine scale structures. Considering the importance of the instantaneous evolution of the large coherent structures in the noise production mechanism, RANS-based method are expected to show weaknesses regarding that noise component. Other noise prediction techniques could have been considered. However, they include heavy scale-resolving methods such as direct numerical simulations (DNS) [34], large eddy simulations (LES) [15] or detached eddy simulations (DES) [60]. Because of the strong objectives in terms of restitution time, these other methods will be left aside from this review.

2.3 Acoustic analogies

In recent years, numerous jet mixing noise prediction methods have been developed; all of which based on acoustic analogies. This concept is described in the following subsection along with a few examples covering most of the existing different RANS-based models.

2.3.1 Lighthill's analogy

Lighthill [46] introduced the concept of the acoustic analogy in 1952. The idea is to build an equation to describe the radiation of aeroacoustic sources. In this equation, the left hand side is a

differential equation accounting for the propagation of the wave and the right hand side describes the sources in the flow. As a starting point, he uses the continuity and momentum equations.

$$\frac{\partial \rho}{\partial t} + \frac{\partial (\rho u_i)}{\partial x_i} = 0 \tag{2.1}$$

$$\frac{\partial (\rho u_i)}{\partial t} + \frac{\partial (\rho u_i u_j + P_{ij})}{\partial x_j} = 0 \tag{2.2}$$

where $P_{ij} = p\delta_{ij} - \tau_{ij}$ with τ_{ij} the viscous stresses and δ_{ij} the Kronecker delta function. Both equations are combined to form the following wave equation

$$\frac{\partial^2 \rho}{\partial t^2} - \frac{\partial^2 (\rho u_i u_j + P_{ij})}{\partial x_i \partial x_j} = 0 \tag{2.3}$$

The term $-c_0^2 \nabla^2 \rho$ is added on both sides giving

$$\frac{\partial^2 \rho}{\partial t^2} - c_0^2 \nabla^2 \rho = \frac{\partial^2 (\rho u_i u_j + P_{ij} - c_0^2 \rho_{ij})}{\partial x_i \partial x_j} \tag{2.4}$$

and classicaly rewritten

$$\frac{\partial^2 \rho}{\partial t^2} - c_0^2 \nabla^2 \rho = \frac{\partial^2 T_{ij}}{\partial x_i \partial x_j} \tag{2.5}$$

with $T_{ij} = \rho u_i u_j - \tau_{ij} + (p - c_0^2 \rho)\delta_{ij}$ referred to as the Lighthill stress tensor. The Lighthill equation is a recombination of the equations of fluid mechanics and is therefore exact at this step. Eq (2.5) is comparable to the classical wave equation and the problem can then be seen as the propagation of sources of strength T_{ij} in a homogeneous medium at rest. In such a medium, the mean pressure $\bar{p}$ and mean density $\bar{\rho}$ are constant. Therefore, if the fluctuations of pressure $p' = p - \bar{p}$ and the fluctuations of density $\rho' = \rho - \bar{\rho}$ are introduced, Eq (2.5) can be rewritten as

$$\frac{\partial^2 \rho'}{\partial t^2} - c_0^2 \nabla^2 \rho' = \frac{\partial^2 T_{ij}}{\partial x_i \partial x_j} \tag{2.6}$$

The analytical solution of Eq (2.6) is known. It is obtained by convolution with a Green function, which yields

$$\rho'(\vec{x}_M, t) = \int_{\vec{\xi}_S} \int_{t_1} G(\vec{\xi}_S, \vec{x}_M; t, t_1) \frac{\partial^2 T_{ij}\left(\vec{\xi}_S, t_1\right)}{\partial \xi_i \partial \xi_j} \mathrm{d}\vec{\xi}_S \mathrm{d}t_1 \tag{2.7}$$

with the Green function in free space

$$G(\vec{\xi}_S, \vec{x}_M; t, t_1) = \delta\left(t_1 - t + \left|\vec{x}_M - \vec{\xi}_S\right| / c_0\right) / \left(4\pi c_0^2 \left|\vec{x}_M - \vec{\xi}_S\right|\right) \tag{2.8}$$

substituted into Eq (2.7) and the integration according to τ is achieved, giving

$$\rho'(\vec{x}_M,t)=\frac{1}{4\pi c_0^2}\int_{\vec{\xi}_S}\frac{1}{\left|\vec{x}_M-\vec{\xi}_S\right|}\frac{\partial^2}{\partial\xi_i\partial\xi_j}T_{ij}\left(\vec{\xi}_S,t-\left|\vec{x}_M-\vec{\xi}_S\right|/c_0\right)\mathrm{d}\vec{\xi}_S \tag{2.9}$$

and

$$p'(\vec{x}_M,t)=\frac{1}{4\pi}\int_{\vec{\xi}_S}\frac{1}{\left|\vec{x}_M-\vec{\xi}_S\right|}\frac{\partial^2}{\partial\xi_i\partial\xi_j}T_{ij}\left(\vec{\xi}_S,t-\left|\vec{x}_M-\vec{\xi}_S\right|/c_0\right)\mathrm{d}\vec{\xi}_S \tag{2.10}$$

In the far-field, the differentiation can be recast as

$$p'(\vec{x}_M,t)=\frac{1}{4\pi c_0^2}\int_{\vec{\xi}_S}\frac{(x_i-\xi_i)(x_j-\xi_j)}{\left|\vec{x}_M-\vec{\xi}_S\right|^3}\frac{\partial^2 T_{ij}}{\partial t^2}\left(\vec{\xi}_S,t-\frac{\left|\vec{x}_M-\vec{\xi}_S\right|}{c_0}\right)\mathrm{d}\vec{\xi}_S \tag{2.11}$$

By definition, the power spectral density of the pressure fluctuations is given by

$$\hat{S}(\vec{x}_M,\omega)=\frac{1}{2\pi}\int_{-\infty}^{\infty}\left\langle p'(\vec{x}_M,t)p'(\vec{x}_M,t+\tau)\right\rangle e^{i\omega\tau}\mathrm{d}\tau \tag{2.12}$$

In this formula, the brackets $\langle..\rangle$ denote a statistical average. For an ergodic process, one has

$$\left\langle p'(\vec{x}_M,t)p'(\vec{x}_M,t+\tau)\right\rangle=\lim_{T\to\infty}\frac{1}{T}\int_{-T}^{T}p'(\vec{x}_M,t)p'(\vec{x}_M,t+\tau)\mathrm{d}t \tag{2.13}$$

Inserting Eq (2.11) in Eq (2.12) gives

$$\begin{aligned}\hat{S}(\vec{x}_M,\omega)=\frac{1}{32\pi^3c_0^4}\int_{\tau}\int_{\vec{\xi}_S}\int_{\vec{\zeta}_S}&\frac{(x_i-\xi_i)(x_j-\xi_j)(x_k-\zeta_k)(x_l-\zeta_l)}{\left|\vec{x}_M-\vec{\xi}_S\right|^3\left|\vec{x}_M-\vec{\zeta}_S\right|^3}\\&\left\langle\frac{\partial^2T_{ij}}{\partial t^2}\left(\vec{\xi}_S,t_\xi\right)\frac{\partial^2T_{kl}}{\partial t^2}\left(\vec{\zeta}_S,t_\zeta+\tau\right)\right\rangle e^{i\omega\tau}\mathrm{d}\tau\mathrm{d}\vec{\xi}_S\mathrm{d}\vec{\zeta}_S\end{aligned} \tag{2.14}$$

with the following change of variables

$$t_\xi=t-\frac{\left|\vec{x}_M-\vec{\xi}_S\right|}{c_0},\text{ and }t_\zeta=t-\frac{\left|\vec{x}_M-\vec{\zeta}_S\right|}{c_0} \tag{2.15}$$

In order to simplify the notation, the fourth-order correlation tensor is introduced

$$R_{ijkl}(\vec{\xi}_S,\vec{s},\tau)=\left\langle\frac{\partial^2T_{ij}}{\partial t^2}\left(\vec{\xi}_S,t\right)\frac{\partial^2T_{kl}}{\partial t^2}\left(\vec{\xi}_S+\vec{s},t+\tau\right)\right\rangle \tag{2.16}$$

with $\vec{s}=\vec{\zeta}_S-\vec{\xi}_S$. Giving for the power spectral density,

$$\hat{S}(\vec{x}_M,\omega)=\frac{1}{32\pi^3 c_0^4}\int_\tau\int_{\vec{\xi}_S}\int_{\vec{\zeta}_S}\frac{(x_i-\xi_i)(x_j-\xi_j)(x_k-\zeta_k)(x_l-\zeta_l)}{\left|\vec{x}_M-\vec{\xi}_S\right|^3\left|\vec{x}_M-\vec{\zeta}_S\right|^3}R_{ijkl}(\vec{\xi}_S,\vec{s},\tau)e^{i\omega\tau}\mathrm{d}\tau\mathrm{d}\vec{\xi}_S\mathrm{d}\vec{\zeta}_S \tag{2.17}$$

In addition, the following approximations can be done in the far-field:

$$\begin{aligned} x_j-\xi_j &\simeq x_j \\ \left|\vec{x}_M-\vec{\xi}_S\right| \simeq \left|\vec{x}_M-\vec{\zeta}_S\right| &\simeq |\vec{x}_M| \end{aligned} \tag{2.18}$$

The power spectral density in Eq (2.17) is finally recast in the following compact form

$$\hat{S}(\vec{x}_M,\omega)=\frac{1}{32\pi^3 c_0^4}\frac{x_i x_j x_k x_l}{|\vec{x}_M|^6}\int_\tau\int_{\vec{\xi}_S}\int_{\vec{s}}R_{ijkl}(\vec{\xi}_S,\vec{s},\tau)e^{i\omega\tau}\mathrm{d}\tau\mathrm{d}\vec{\xi}_S\mathrm{d}\vec{s} \tag{2.19}$$

Two main drawbacks arise from this acoustic analogy. First, even though the analogy is an exact description of the physics, the sound propagation is done for a homogeneous medium at rest. Flow effects are therefore formally included in the source term. Second, the Lighthill stress tensor is not readily obtained and needs to be modelled. In an effort to properly separate the source terms and the propagation terms, successive formulations were introduced using the work performed by Lighthill.

2.3.2 Goldstein's analogy from 1976

Goldstein's analogy [35] is a slight variation of Lighthill's formulation. The starting point is Eq (2.5) applied in a shifted frame $\tilde{x}_i = x_i - \delta_{ix}\bar{u}_x\tau$ where a uniform mean flow $\bar{u}_x$ is considered in the $\vec{x}$ direction. With this change of variable, a convected wave equation is obtained

$$\frac{\mathrm{D}^2\rho'}{Dt^2}-c_0^2\nabla^2\rho'=\frac{\partial^2\tilde{T}_{ij}}{\partial x_i\partial x_j} \tag{2.20}$$

with the material differentiation along the mean flow defined as $\dfrac{\mathrm{D}}{\mathrm{D}t}=\dfrac{\partial}{\partial t}+\bar{u}_x\dfrac{\partial}{\partial x_x}$ and the modified Lighthill stress tensor

$$\tilde{T}_{ij}=\rho\tilde{u}_i\tilde{u}_j-\tau_{ij}+(p-c_0^2\rho)\delta_{ij} \tag{2.21}$$

where $\tilde{u}_i = u_i - \delta_{ix}\bar{u}_x$. Although the wave operator has increased in complexity, a solution can still be analytically obtained because the left hand side is the convected Helmholtz equation. The Green function solution of Eq (2.21) is noted G_{CHE}. The pressure fluctuation field is given by

$$p'(\vec{x}_M,t)=\int_{\vec{\xi}_S}\int_{t_1}G_{\mathrm{CHE}}(\vec{x}_M,\vec{\xi}_S;t,t_1)\frac{\partial^2\tilde{T}_{ij}}{\partial\xi_i\partial\xi_j}(\vec{\xi}_S,t_1)\mathrm{d}\vec{\xi}_S\mathrm{d}t_1 \tag{2.22}$$

Eq (2.22) is inserted in Eq (2.12) to obtain the power spectral density. That gives,

$$\hat{S}(\vec{x}_M,\omega) = \frac{1}{2\pi}\int_\tau\int_{t_1}\int_{\vec{\xi}_S}\int_{\vec{s}} G_{\mathrm{CHE}}(\vec{x}_M,\vec{\xi}_S;t,t_1)G_{\mathrm{CHE}}(\vec{x}_M,\vec{\xi}_S+s;t,t_1+\tau) \\ \tilde{R}_{ijkl}(\vec{\xi}_S,\vec{s},\tau)e^{i\omega\tau}\mathrm{d}\tau\mathrm{d}t_1\mathrm{d}\vec{\xi}_S\mathrm{d}\vec{s} \tag{2.23}$$

with

$$\tilde{R}_{ijkl}(\vec{\xi}_S,\vec{s},\tau) = \left\langle \frac{\partial^2\tilde{T}_{ij}}{\partial\xi_i\partial\xi_j}\left(\vec{\xi}_S,t\right)\frac{\partial^2\tilde{T}_{kl}}{\partial\xi_k\partial\xi_l}\left(\vec{\xi}_S+\vec{s},t+\tau\right)\right\rangle \tag{2.24}$$

Only the modified Lighthill stress tensor $\tilde{T}_{ij}$ remains part of the autocorrelation function $\tilde{R}_{ijkl}$. Because the Green function G_{CHE} is deterministic, it can be taken out of the statistical average.

Thanks to the work from Goldstein, a first step has been done in the improvement of Lighthill's analogy. By transferring the terms linked to the mean axial velocity $\bar{u}_x$ from the right to the left hand side, the convective effects have successfully been included in the wave operator.

2.3.3 Lilley's analogy

Phillips [62] introduced a new analogy in which the convective effects are included in the wave operator. The addition of these effects is embodied by the presence of a material differentiation in place of the time differentiation. The tedious calculations can be simplified by introducing a new variable $\pi' = \ln(p'/p_0)$. The updated form of the analogy is

$$\frac{\mathrm{D}^2\pi'}{\mathrm{D}t^2} - \frac{\partial}{\partial x_i}\left(\bar{c}^2\frac{\partial\pi'}{\partial x_i}\right) = \gamma\frac{\partial u_i}{\partial x_j}\frac{\partial u_j}{\partial x_i} + \gamma\frac{\mathrm{D}}{\mathrm{D}t}\left(\frac{1}{c_p}\frac{\mathrm{D}s}{\mathrm{D}t}\right) - \frac{\partial}{\partial x_i}\left(\frac{\gamma}{\rho}\frac{\partial\tau_{ij}}{\partial x_j}\right) \tag{2.25}$$

with the material differentiation along the mean flow defined as $\dfrac{\mathrm{D}}{\mathrm{D}t} = \dfrac{\partial}{\partial t} + \bar{u}_x\dfrac{\partial}{\partial x_x}$. Here, s is the specific entropy, c_p is the heat capacity at constant pressure and $\bar{c}$ is the mean sound velocity in the flow. A part of refraction effects is unfortunately still missing in the wave operator. Lilley [48] successfully incorporated the remaining term in the left hand side by applying an additional time differentiation, thus forming a third-order differential equation. The Lilley operator is expressed as

$$\frac{\partial}{\partial t}\left[\frac{\mathrm{D}^2\pi'}{\mathrm{D}t^2} - \frac{\partial}{\partial x_i}\left(\bar{c}^2\frac{\partial\pi'}{\partial x_i}\right)\right] - 2\gamma\frac{\partial\bar{u}_i}{\partial x_j}\frac{\partial}{\partial x_i}\left(\bar{c}^2\frac{\partial\pi'}{\partial x_i}\right) = \Lambda(\vec{x},t) \tag{2.26}$$

where Λ regroups all of the remaining terms, forming the source term of Lilley's analogy. While this additional derivation adds a layer of complexity in terms of both solving and interpreting this equation, it allows for the inclusion of the refraction effects. Λ contains only non linear terms, the source and propagation-related terms are therefore fully separated in this formulation.

There is however no analytical Green function. The propagation has to be numerically performed or simplifications have to be done to obtain a solvable form of Lilley's operator. Balsa [8] and Goldstein [35] introduced asymptotic solutions at low and high frequencies using Green functions. Therefore, with similar calculations as with Goldstein's analogy, the power spectral density can be written using the Green function G_L, asymptotic solution of Lilley's equation.

$$\begin{aligned}\hat{S}(\vec{x}_M,\omega) = \frac{1}{2\pi}\int_\tau\int_{t_1}\int_{\vec{\xi}_S}\int_{\vec{s}} G_L(\vec{x}_M,\vec{\xi}_S;t,t_1)G_L(\vec{x}_M,\vec{\xi}_S+\vec{s};t,t_1+\tau) \\ R_\Lambda(\vec{\xi}_S,\vec{s},\tau)e^{i\omega\tau}\mathrm{d}\tau\mathrm{d}t_1\mathrm{d}\vec{\xi}_S\mathrm{d}\vec{s}\end{aligned} \tag{2.27}$$

with

$$R_\Lambda(\vec{\xi}_S,\vec{s},\tau) = \Big\langle \Lambda(\vec{\xi}_S,t)\Lambda(\vec{\xi}_S+\vec{s},t+\tau)\Big\rangle \tag{2.28}$$

Only the source term Λ stays in the autocorrelation function R_Λ. The Green function G_L is taken out of the statistical average.

Lilley successfully introduced an exact equation in which the left hand side accounts for the propagation of the wave and the right hand side contains only the exciting source terms. Bailly *et al.* [5] showed that the linearised Euler equations, if associated with the appropriate source terms, could be recast into Lilley's equation. As such, the computation of the propagation using the LEE or Lilley's operator holds the same level of accuracy.

2.3.4 Tam and Auriault's analogy

Tam and Auriault developed a semi empirical model [78] in which a tailored source term is added to the linearised Euler equation. This source term is the gradient of $q_s = 2/3\rho\hat{k}_s$ where $\hat{k}_s$ is associated with the kinetic energy of fine scale turbulence. These equations are joined with the continuity equation with no forcing term. That gives

$$\begin{aligned}\bar{\rho}\left[\frac{\partial u_i'}{\partial t} + \bar{u}_j\frac{\partial u_i'}{\partial x_j} + u_j'\frac{\partial \bar{u}_i}{\partial x_j}\right] + \frac{\partial p'}{\partial x_i} = -\frac{\partial q_s}{\partial x_i} \\ \frac{\partial p'}{\partial t} + \bar{u}_j\frac{\partial p'}{\partial x_j} + \gamma\bar{p}\frac{\partial u_j'}{\partial x_j} = 0\end{aligned} \tag{2.29}$$

Tam and Auriault used a vectorial adjoint Green function to solve the LEE and showed that the power spectral density, given in Eq (2.12), can be reduced to

$$\begin{aligned}\hat{S}(\vec{x}_M,\omega) = \int_{\omega_1}\int_{\vec{\xi}_S}\int_{\vec{\zeta}_S}\int_{t_1}\int_{t_2}\hat{p}'^a(\vec{\xi}_S,\vec{x}_M;\omega_1)\hat{p}'^a(\vec{\zeta}_S,\vec{x}_M;\omega)\left\langle\frac{\mathrm{D}q_s(\vec{\xi}_S,t_1)}{\mathrm{D}t_1}\frac{\mathrm{D}q_s(\vec{\zeta}_S,t_2)}{\mathrm{D}t_2}\right\rangle \\ e^{-i(\omega_1+\omega)t+i\omega_1t_1+i\omega t_2}\mathrm{d}\omega_1\mathrm{d}\vec{\xi}_S\mathrm{d}\vec{\zeta}_S\mathrm{d}t_1\mathrm{d}t_2\end{aligned} \tag{2.30}$$

Here again, only the q_s-dependent terms remain within the brackets, for the same reason as in the previous analogies. The correlation term can be written as

$$R_s(\vec{\xi}_S, \vec{\zeta}_S, t_1, t_2) = \left\langle \frac{\mathrm{D}q_s(\vec{\xi}_S, t_1)}{\mathrm{D}t_1} \frac{\mathrm{D}q_s(\vec{\zeta}_S, t_2)}{\mathrm{D}t_2} \right\rangle \tag{2.31}$$

Just like Lilley's acoustic analogy, the pressured field cannot be analytically obtained because $\hat{p}'^a$ is unknown. Some simplifications or a numerical computation are required. This can be done in numerous ways and Tam and Auriault decided to solve numerically the problem after some simplifications.

Although the formulation of the problem cannot be considered as exact, in the sense that these equations are not obtained from fluid mechanics equations, Tam and Auriault argued that the new source modelling gives a more precise representation of the noise generation mechanism. Indeed, Tam questions the Lighthill analogy [76], claiming that the so-called quadrupole sources do not describe accurately the sources of jet noise. However, Morris and Farassat [58] showed the equivalence of Lighthill's analogy and Tam and Auriault's model when applied in a homogeneous medium at rest. Moreover, and as previously mentioned, using Lilley's operator or the LEE does not change the level of accuracy on the sound propagation. Under these considerations, Tam and Auriault's model can be seen as a modern formulation of the propagation of sound waves in a sheared flow.

2.3.5 Generic structure of the power spectral density

Comparing Eq (2.19), (2.23), (2.27) and (2.30) highlights a similar structure for the expression of the power spectral density $\hat{S}(\vec{x}_M, \omega)$ regardless of the chosen analogy. This generic structure is reminded below,

$$\hat{S}(\vec{x}_M, \omega) = \frac{1}{2\pi} \int_\tau \int_{t_1} \int_{\vec{\xi}_S} \int_{\vec{s}} G(\vec{x}_M, \vec{\xi}_S; t, t_1) G(\vec{x}_M, \vec{\xi}_S + \vec{s}; t, t_1 + \tau) R(\vec{\xi}_S, \vec{s}, \tau) e^{i\omega\tau} \mathrm{d}\tau \mathrm{d}t_1 \mathrm{d}\vec{\xi}_S \mathrm{d}\vec{s} \tag{2.32}$$

The formulation of the PSD can be split in two parts with first the Green function G handling the propagation, and second the two-point space-time correlation of the source term R taking care of the source modelling. The expression of the latter, more than the detailed behaviour of the source term itself, is required for the computation. The next subsection gives a review of the methods developed to obtain both parts.

2.4 Source modelling

The description of the sources within the jet is addressed in two independent steps. The first part is the use of a mathematical representation of these sources and the second is the use of inputs to compute their strength. The mathematical formulation of the autocorrelation of the

source terms is first addressed. An example of experimental data of this correlation, made by Davies *et al.* [27], is pictured in Fig 2.5. The exact values of these terms in the whole jet plume is often unknown and a statistical approach is used to provide these correlations to the model functions. A review of different ways the correlation term R has been modelled is first presented. This review aims at highlighting what exactly is included in the source model and the domain of application of each formulation. Using a statistical description of the turbulence implies the introduction of scaling parameters. These are described in a second subsection and formulations used to model them are presented. Finally, different input options for the computation of R are given.

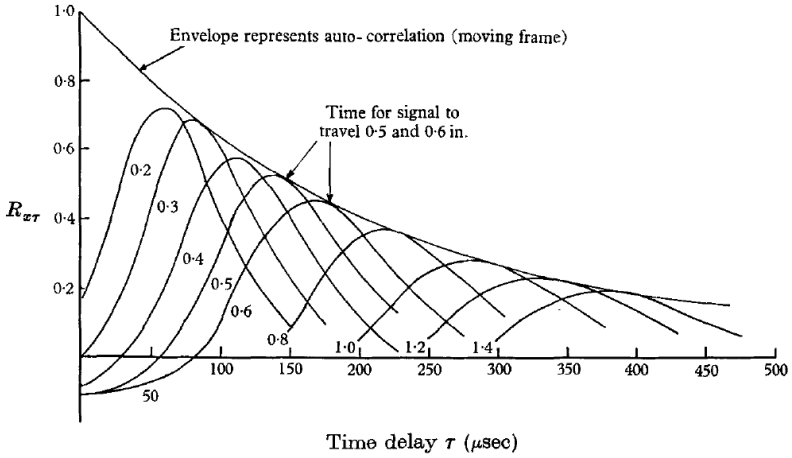

Figure 2.5: Cross correlation of axial velocity fluctuations with downstream wire separation every 0.1 in. From Davies *et al.* [27]

2.4.1 Statistical model

Khavaran *et al.* [43] were among the first to introduce a jet mixing noise prediction method of the range of interest here. They considered that the noise spectrum would be dominated by the unsteady momentum stress meaning that $T_{ij} \simeq \rho u_i u_j$ and therefore $R_{ijkl} \simeq \rho^2 \langle u_i u_j u_k u_l \rangle$. Citing Ribner [68], they argue that the space and time factors of the correlation decay could be separated. The space factor is established using a homogeneous isotropic turbulence model from Batchelor [11] whereas the time factor is introduced as a Gaussian decay. Hence

$$R_{ijkl}(\vec{\xi}_S, \vec{s}, \tau) = R_{ijkl}(\vec{\xi}_S, 0, 0) \exp\left(-\frac{\tau^2}{\tau_0^2}\right) \left[\left(f + \frac{1}{2}|\vec{s}|\, f'\right) \delta_{ij} - \frac{1}{2} f' \frac{s_i s_j}{|\vec{s}|}\right] \tag{2.33}$$

where the longitudinal correlation function f is approximated by a Gaussian function following Lilley [47] and $f' = df/ds_i$.

$$f(|\vec{s}|) = \exp\left(-\frac{\pi|\vec{s}|^2}{l^2}\right) \tag{2.34}$$

For the full computation of this model function, the three scaling elements $R_{ijkl}(\vec{\xi_S}, 0, 0)$, τ_0 and l have to be defined. They are respectively the magnitude of the autocorrelation, a time scale and a length scale. The next subsection goes more in details regarding these parameters. Later, Khavaran [41] went one step further by introducing a new formulation for its correlation model function by considering an axisymmetric turbulence instead of an isotropic state, using Chandrasekhar [25] with good results. Later, Khavaran *et al.* [42] extended their work to hot jets by adding a modelling of the enthalpy source term in the Lighthill stress tensor independently of the already included momentum source term. Tam and Auriault used results from Davies *et al.* [27]. Experimentally, it was found that the spatial decay can be assimilated to a Gaussian function whereas the time decay fits an exponential decrease. These observations translates mathematically to a correlation function of the following form

$$\begin{aligned} R_s(\vec{\xi_S}, \vec{\zeta_S}, t_1, t_2) = \frac{I_s^2}{\tau_s^2}\exp\left(-\frac{|\xi_x - \zeta_x|}{\bar{u}_x\tau_s}\right) \\ \exp\left(-\frac{\ln 2}{l_s^2}\left[[(\xi_x - \zeta_x) - \bar{u}_x(t_1 - t_2)]^2 + (\xi_y - \zeta_y)^2 + (\xi_z - \zeta_z)^2\right]\right) \end{aligned} \tag{2.35}$$

where τ_s and l_s are respectively the time and length scale of the fine scale turbulence. Tam and Auriault's work was nevertheless limited to isothermal jets while also neglecting the density gradient. To make up for these effects, Tam *et al.* [81] introduced an updated version of their model function with an additional term based on the measurements of Doty and McLaughlin [31]. Improved results were observed when applied to hot jets, compared to the previous theory. Morris and Boluriaan [57] also started from the LEE like Tam and Auriault [78] but included more terms in the right hand side of the momentum equation citing Morris and Farassat [58]. They also added an equivalent dilatation rate source term to the continuity equation. These source terms are in fact the remainders from the linearisation of the Euler equation. It is assumed that the two-point correlation functions of both source terms follow the same decay pattern as in Eq (2.35) albeit some minor changes. It is also assumed that they are uncorrelated with each other. Self [71] [72] followed the same assumption as Khavaran *et al.* [43] regarding the expression of T_{ij}. He however modelled directly the cross-spectral density, that is the Fourier transform of the space-time correlation function. This was motivated by the observation that the characteristic scales involved are function of the frequency [37]. The model function introduced is of the following form

$$\hat{R}_s(\vec{\xi}_S, \vec{s}, \omega) = u^4 2\sqrt{\pi}\tau_s \exp\left(-\frac{\omega^2(1 - M_c\cos\theta)^2\tau_s^2}{4}\right)\exp\left(-\frac{s_x^2}{l_x^2} - \frac{s_y^2}{l_y^2} - \frac{s_z^2}{l_z^2}\right) \tag{2.36}$$

where u is a characteristic velocity of the turbulence, τ_s and l_i are time and length scales, M_c is the jet Mach number and θ is the polar angle of the observer. The relation between the frequency and the scaling parameters is explicited in the next subsection. Semiletov and Karabasov [74] chose yet another formulation for R_{ijkl} with the same asumption on $T_{ij} \simeq \rho u_i u_j$ as done by Khavaran *et al.* [43]. Citing [36], they write

$$R_{ijkl}(\vec{\xi}_S, \vec{s}, \omega) = R_{ijkl}(\vec{\xi}_S, 0, 0)\exp\left(-\sqrt{\left[\frac{|U_c\tau|}{l_\tau}\right]^2 + \left[\frac{|s_x - U_c\tau|}{l_x}\right]^{2.5} + \left[\frac{|s_y|}{l_y}\right]^{2.5} + \left[\frac{|s_z|}{l_z}\right]^{2.5}}\right) \tag{2.37}$$

where l_τ and l_i are length scales whose values are obtained through a fit with measurements. Their formulation showed good agreements with the experimental data of R_{1111} and R_{2222}.

To sum up, there is a wide range of possibilities in terms of model functions and the fact that these formulations are still used in parallel shows that there is no consensus on a general expression. Given the inherent level of accuracy of RANS-based methods, it is arguable that any of these statistical descriptions would lead to similar results.

2.4.2 Calibration of the model

A number of variables are required to compute the model functions for the two-point correlation presented in the previous subsection. Some are readily available because related to basic flow data but a few scaling parameters also appear as time scales, length scales and turbulence strengths. The present subsection gives ways to get either directly the exact value of these turbulent scales, or how to reconstruct them using RANS CFD simulations. Khavaran *et al.* [43] and Bailly *et al.* [7] suggested that the time and length scales in Eq (2.33) could be obtained using the turbulent kinetic energy k_t and the turbulent dissipation ϵ with

$$\begin{aligned} \tau_0(\vec{\xi}_S) =& c_\tau \frac{k_t(\vec{\xi}_S)}{\epsilon(\vec{\xi}_S)} \\ l(\vec{\xi}_S) =& c_l \frac{k_t^{3/2}(\vec{\xi}_S)}{\epsilon(\vec{\xi}_S)} \end{aligned} \tag{2.38}$$

Khavaran *et al.* [43] added the following expression for the magnitude of the two-point correlation function

$$R_{ijkl}(\vec{\xi}_S, 0, 0) = A\rho^2(\vec{\xi}_S)k_t^2(\vec{\xi}_S) \tag{2.39}$$

with ρ being the density. These formulations are often referred as classical scales and are widely used by numerous research groups. As a reminder to previously cited papers, Tam and Auriault [78], Morris and Boluriaan [57] used these scales. However, alternative expressions have also been proposed. Self [71] [72] introduced a frequency dependency on the time scale to match with the observations of Harper-Bourne [37]. The work was extended with a new formulation by Self and Azarpeyvand [73] using the rate energy transfers in which the frequency does not appear explicitly, thus reducing the empiricism of the previous. A simplified version of this formulation was inserted in Eq (2.33) by Azarpeyvand and Self [4]. Predictions using these scales showed better results than when using Eq (2.38). These improved results were attributed to a better representation of the underlying physics. Raizada and Morris [66] also introduced a frequency dependence but here applied on the length scale, which also led to improved predictions compared to the traditional scales. In addition to an updated two-point space-time correlation function for the study of hot jets, Tam *et al.* [81] also introduced a perturbation term to the different scaling variables, as proposed by Tam and Ganesan [79]. This term is linked to the density gradient.

2.4.3 Inputs

As early as 1994, Bailly *et al.* [7] and Khavaran *et al.* [43] used Reynolds-Averaged Navier-Stokes (RANS) simulation based on a $k-\epsilon$ model to feed local values to the source models. Since then, the use of RANS simulations has been very popular for jet mixing noise predictions due to the relatively short restitution time of the method. However, the results are often not considered satisfactory as is and the characteristic scales are fitted on experimental results [43][78][55] through an optimisation of the value of c_l, c_τ and A. Ideally the testcase used for the simulation and the predictions should match, as done by Khavaran *et al.* [43]. Under some assumptions, the fit could still be done with another jet. For example, Tam and Auriault [78] proposed a generic set of coefficients obtained by fitting the model function on experimental data using jets with a wide range of temperature ratio and jet speeds. Karabasov *et al.* [40] broke ground by using data from a large eddy simulation instead of farfield measurements to calibrate the scaling parameters. They indeed obtained the correlation shapes from a LES and then performed a Gaussian fit to extract the coefficients of the classical scales. Not only did this method show good results, but they also obtained good agreements downstream where the large scale spectrum dominates without the addition of another source. Depuru-Mohan *et al.* [28] reproduced the same process on jet noise from chevron nozzles [18] with good results. Since the fit is done prior to the noise predictions the robustness of the method is increased, there is however a need of a rather costly LES. In the same way, experimental data could be used for this calibration. And even though this is more complicated because of the large quantity of data required and because of the difficulty to obtain clean data in all the flow, some have succeeded. Bridges and Wernet [19] measured a substantial portion of the two-point space-time velocity correlation in hot, high-speed turbulent jets using Particle Image Velocimetry (PIV). From this, the length and timescales can be computed and used for the constant fit. In conclusion a RANS simulation is not enough to perform the noise

predictions, it has to be joined by a constant set appropriately chosen.

2.5 Resolution of the propagation

Once the source has been modelled, the noise has to be propagated to the observer. This subsection presents some options for the execution of this step along with their main advantages and drawbacks.

2.5.1 Analytical resolution

The analytical resolution of the differential equations governing the propagation is both the fastest and the most accurate from a mathematical point of view. This is however only possible when using Lighthill's or Goldstein's analogy. This option is interesting both in terms of computing time and power and it was chosen by numerous school of thought within the jet noise community. As an example, one can cite the MGBK model, developped first by Mani-Gliebe-Balsa in [51] [10] and [9] and completed by Khavaran *et al.* [43] and Khavaran [41]. This model uses as a starting point Lighthill's analogy. Similarly, Self [71] [72], Self and Azarpeyvand [73] and Azarpeyvand and Self [4] used Goldstein's approach. But these analogies do not account for refraction effects. It is however possible to include the reflection effects, as it has been done by Lyu *et al.* [50] by solving the differential equation with the introduction of boundary conditions. The LEE or Lilley operator contain more propagation effects but do not have a solution readily available. Balsa [8] and Goldstein [35] introduced however asymptotic versions of Lilley's analogy at high and low frequencies that allow for analytical resolutions using Green functions. In parallel, Morris and Boluriaan [57] showed that when considering a parallel axisymmetric mean flow, the LEE could be simplified. In this new form, the Lilley operator can be introduced. By linking both fomulations, they also linked the LEE solution to the asymptotic solutions of Lilley's equation. Further simplifying the problem, Brouwer and Nijboer [20] applied the work of Tam and Auriault [78] in a homogeneous medium thus reducing the LEE to a convected Helmholtz equation. Incidentally, they could use the analytical formulation of the adjoint Green's function of the CHE.

2.5.2 Numerical resolution

The LEE or Lilley operator might also be treated using a numerical approach to fully solve differential equation without simplifying the problem. Bechara *et al.* [12] and Bailly and Juve [6] solved the LEE in their primitive form in the frame of the Stochastic Noise Generation and Radiation (SNGR) model. The introduction of the adjoint problem has shown great improvement regarding the numerical resolution compared to the direct problem. Indeed, by inverting the roles of the sources and the observers, the number of points in which Green functions need to be computed is considerably reduced. Tam and Auriault [78] and Miller [55] used this solution. Beyond the numerical gains of the adjoint method, it also helped Tam and Auriault [78] reduce the number of Green function to calculate at each source point from three to only one.

2.5.3 Geometrical acoustics

Finally, another propagation model based on geometrical acoustics has to be addressed. As described by Candel [22], if the acoustic wavelength is quite small compared to the characteristic lengthscale of the propagation medium, here the jet radius, waves can be considered locally plane waves. In this approximation, the solution can be sought as $\mathbf{u}(\vec{x},t) = \mathbf{A}(\vec{x},t)\exp\left(i\psi(\vec{x},t)\right)$ where $\mathbf{A}$ is an amplitude vector and ψ is the phase. From this comes a dispersion relation allowing the computation of the propagation of the ray through the propagation medium. The conservation of energy given by the Blokhintzev invariant [13] is then used on the ray path to obtain the amplitude. In the frame of geometrical acoustics, the characteristic length and characteristic time of the propagation medium are considered greatly superior to respectively the wavelength and the period of the considered wave [22]. The ray is computed step by step from the source, there are thus no guarantee that it will reach the desired observer. This eigen-ray is found by convergence using successive ray-shooting steps. Depending on the complexity of the problem and the number of sources, this iterative process might lead to heavy computing times. There is a possible simplification of the model by considering that the propagation medium is homogeneous by part with infinitely thin interfaces. In this case, the ray changes its path only when reaching an interface instead of every infinitesimal variation in the fluid properties. The reduction in complexity of the wave path induces a simplification of the search for the eigen rays. The change of amplitude linked to a refraction or a reflection on a curved surface has been calculated by Deschamps [29]. Such a method has been proposed already for corrections applied to experimental experiments in case of open jet wind tunnels by Amiet [2]. This was extended for sources located off the jet axis by Morfey and Joseph [56] and later by McLaughlin *et al.* [52] to model the jet-blockage for installed jets using image sources. These methods do not predict noise spectra but correct existing spectra to obtain predictions in other configurations. The diffraction of the waves on edges was not included in these methods. Candel [23] introduced a similar method where a sheared flow is discretised into stratified homogeneous flows. Although this method is not linked with geometrical acoustics, it shows that this simplification of the propagation medium has already been done for jet noise.

2.6 Solution used for the noise predictions

An overview of statistical methods for jet mixing noise predictions has been presented. A choice regarding the source and propagation models needs to be done to address our requirements that are reminded here.

- Take into account refraction effects when passing through the jet mixing layer, the reflections on the surrounding boundaries, i.e. a pylon, a wing and flaps as well as the diffraction on edges.
- Be able to tackle a realistic 3D geometry such as an installed jet.

- Be able to produce results within a reasonable computing time as the process should be usable within design loops.

The compromise between the savings of computing resources and the inclusion of propagation effects is the core of the study. On the contrary, the choice of the source model appears to be less critical. Lighthill's and Goldstein's analogy do not match the requirements considering the lack of propagation effects included. On the contrary, the LEE and Lilley's equation fit the desired framework. Ray tracing techniques and approximated analytical solutions as done by Morris and Boluriaan [57] are appropriate options while a numerical resolution of the propagation is expected to be too computer heavy, especially if done on industrial meshes. There is not a unique solution to address the problematic set in this thesis so the convenience of the implementation of this new model should play a role. One of the method used by Airbus for jet mixing noise predictions is based on the work from Tam and Auriault [78] and Brouwer and Nijboer [20] on 2D RANS CFD simulations and shows encouraging results. Additionally, a ray tracing tool named Acti-HF is available. Historically it was developed for electromagnetism problems and therefore uses homogeneous media. It can tackle refractions, reflections and diffractions on edges which matches the requirements in terms of propagation effects while being faster than what was proposed by Candel [22]. Considering the existing solutions within Airbus' numerical toolbox and the requirements for the newly developed model it is chosen to use Tam and Auriault's [78] formulation and their source model as a starting point. Their flow description is simplified as to introduce homogeneous media in order to solve the propagation using simplified ray tracing techniques.

3 Development of the mixing noise model

The objective of this Chapter is to introduce a fine scale jet mixing noise prediction method. In Section 2.5, the choice of a coupling between a source model based on the Tam and Auriault study [78] and the use of geometrical acoustics in a simplified medium was justified. The mathematical development for the binding of these two theories into a legitimate prediction model is presented in the following sections. First, the global skeleton of a CFD/CAA method is detailed in order to highlight its main components. The choice of source and propagation model by Tam and Auriault [78] is first reminded before introducing the new propagation method based on geometrical acoustics.

3.1 Presentation of the outline of a CFD/CAA method

A CFD/CAA prediction method is a method where a numerical simulation, here a RANS computation, is used as input to obtain the different data needed to predict the full noise spectrum. It was shown in Section 2.3 that the spectral density in $\vec{x}_M$ and at a pulsation of ω can be written in the simplified form

$$\hat{S}(\vec{x}_M,\omega) = \int_{\vec{\zeta}_S} A_S(\vec{\zeta}_S,\omega) P_S(\vec{x}_M,\vec{\zeta}_S,\omega) \mathrm{d}\vec{\zeta}_S \tag{3.1}$$

A closer inspection of Eq (3.1) shows the different elements leading to the noise spectrum. The amplitude of the source A_S is computed using the flow data at the location of a source point $\vec{\zeta}_S$ and the studied pulsation ω. The propagation P_S of the wave from a source point $\vec{\zeta}_S$ to an observer written as $\vec{x}_M$ is computed using the location of these two points as well as the pulsation. The convolution product of these two terms represents the contribution for one source in the total spectrum. This is then done at each source location and all the contributions are integrated. The steps leading to noise prediction are the following:

- Discretisation of the volumic source domain into a cloud of elementary sources using the CFD mesh
- Use of the flow data at each source/cell to compute the source amplitude

- Use of the position of the sources and the position of the observer to compute the propagation of each wave

First, the jet is discretised using the mesh from a RANS computation. This step is illustrated in Fig 3.1 going from a real jet in (a) to a numerical simulation in (b). Once the simulation is done, using a source model presented in Section 2.4 and the local flow data, the sources amplitude A_S can be computed as shown in (c). At this point all the cells in the jet plume are considered as sources. Because the local data is used to compute the source amplitude, A_S is null in some locations. It means that the source is shut down and do not contribute to the noise spectrum.

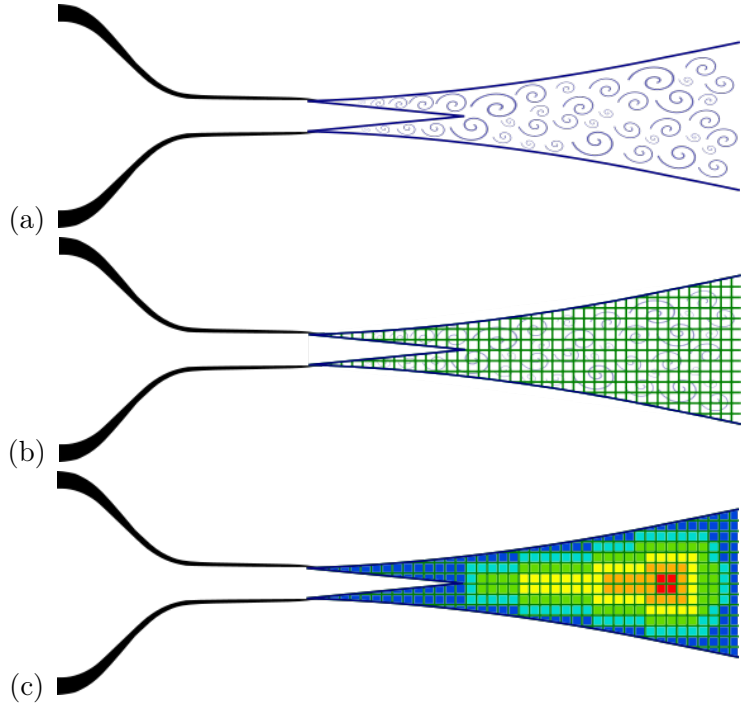

Figure 3.1: Modelling of the source term using a RANS CFD computation

Once A_S is obtained, the propagation is taken care of, as shown in Fig 3.2. As explained, each cell of the mesh is considered to be a source (a), thus creating a cloud of sources (b). Using a propagation method from Section 2.4, the noise is propagated to an observer $\vec{x}_M$ as pictured in (c) and P_S is obtained at each source point $\vec{\zeta}_S$. Given that the source amplitude was found in the previous step, each source is here considered unitary and will only be linked to their amplitude later on.

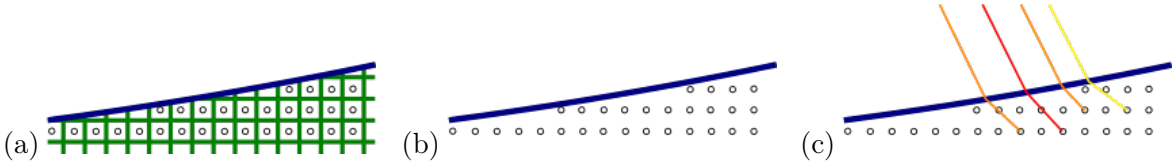

Figure 3.2: Computation of the propagation using each cell of the mesh as a source

A_S and P_S are now known at each elementary source $\vec{\zeta}_S$ of the full source domain, the

contributions can be integrated on the whole jet and $\hat{S}$ can be obtained.

3.2 Jet mixing noise prediction model

In Section 3.1, the outline of a generic CFD/CAA method has been presented. The model developed by Tam and Auriault [78] is explicited in this section to highlight the main steps.

3.2.1 Formulation of the problem

The first step is to write the equations governing the problem. Tam and Auriault use a direct approach to set the problem. An acoustic analogy is built by combining two sets of equation. The left hand side of the system is the wave operator and the right hand side as a source term. The Favre average variables [32] are introduced with the following decomposition

$$f = \tilde{f} + f'' \tag{3.2}$$

where $\tilde{f}$ and f'' are respectively the Favre average and Favre fluctuating components, with $\tilde{f}$ defined as $\tilde{f} = \overline{\rho f}/\bar{\rho}$. Tam and Auriault rederive the transport equation using the Favre average variables, giving

$$\bar{\rho}\left[\frac{\partial \tilde{u}_i}{\partial t} + \tilde{u}_j \frac{\partial \tilde{u}_i}{\partial x_j}\right] + \frac{\partial p'}{\partial x_i} = \frac{\partial}{\partial x_j}(-\overline{\rho u_i'' u_j''} + \bar{\tau}_{ij}) \tag{3.3}$$

Following the classical RANS approach, the Boussinesq closure for the Reynolds stresses is adopted, giving

$$-\overline{\rho u_i'' u_j''} = 2\mu_t \left(S_{ij} - \frac{1}{3} S_{kk}\delta_{ij}\right) - \frac{2}{3}\bar{\rho} k_s \delta_{ij} \tag{3.4}$$

where μ_t is the turbulent dynamic viscosity and S_{ij} is the deformation tensor, expressed as

$$S_{ij} = \frac{1}{2}\left(\frac{\partial \tilde{u}_i}{\partial x_j} + \frac{\partial \tilde{u}_j}{\partial x_i}\right) \tag{3.5}$$

In addition, the kinetic energy of the fine scale turbulence per unit mass k_s is defined as

$$\overline{\rho u_i'' u_i''} = 2\bar{\rho} k_s \tag{3.6}$$

$\bar{\rho}$ is the mean density; p' is the fluctuating pressure; $\bar{\tau}_{ij}$ and $-\overline{\rho u_i'' u_j''}$ are respectively the viscous and Reynolds stresses. The Einstein notation is used, that is an implicit summation on dummy indices. In addition, the subscript i is implicitly associated with the space dimensions, meaning that $i = [1, 2, 3]$.

Next, Tam and Auriault consider the linearised form of Eq (3.3). These authors also argue that both the molecular and viscosity terms can be ignored because they would only have a small influence on the source term intensity, leaving only the term in $\bar{\rho}k_s$, in the right hand side of the system. Finally they consider that the acoustic field is only due to the time-dependent part of k_s, denoted $\hat{k}_s$. The transport equation (3.7) simplifies to

$$\bar{\rho}\left[\frac{\partial u_i'}{\partial t} + \bar{u}_j\frac{\partial u_i'}{\partial x_j} + u_j'\frac{\partial \bar{u}_i}{\partial x_j}\right] + \frac{\partial p'}{\partial x_i} = -\frac{\partial q_s}{\partial x_i} \tag{3.7}$$

$\bar{u}_i$ and u_i' are respectively the mean and fluctuating velocity components in Cartesian coordinates;
with

$$q_s = \frac{2}{3}\bar{\rho}\hat{k}_s \tag{3.8}$$

The system is completed with the linearised continuity and energy equations. The final system of four first-order differential equations is the following

$$\begin{gathered}\bar{\rho}\left[\frac{\partial u_i'}{\partial t} + \bar{u}_j\frac{\partial u_i'}{\partial x_j} + u_j'\frac{\partial \bar{u}_i}{\partial x_j}\right] + \frac{\partial p'}{\partial x_i} = -\frac{\partial q_s}{\partial x_i} \\ \frac{\partial p'}{\partial t} + \bar{u}_j\frac{\partial p'}{\partial x_j} + \gamma\bar{p}\frac{\partial u_j'}{\partial x_j} = 0\end{gathered} \tag{3.9}$$

The wave operator is developed in cylindrical coordinates (x, r, ϕ) and simplified using the locally parallel flow approximations. In this frame, the velocity components are denoted $\bar{\mathbf{u}} = (\bar{u}_x, \bar{u}_r, \bar{u}_\phi)$ for the mean velocity and $\mathbf{u}' = (u_x', u_r', u_\phi')$ for the fluctuating field. For a sheared mean flow, $\bar{u}_x$ and $\bar{\rho}$ are function of r only; $\bar{u}_r$ and $\bar{u}_\phi$ are null and $\bar{p}$ is constant. These assumptions translate to the following relations

$$\begin{aligned}\bar{u}_x &= \bar{u}_x(r) \\ \bar{u}_r &= \bar{u}_\phi = 0 \\ \bar{\rho} &= \bar{\rho}(r) \\ \bar{p} &= \bar{p}_\infty\end{aligned} \tag{3.10}$$

The system (3.9) is simplified to

$$
\begin{aligned}
\bar{\rho}\left[\frac{\partial u'_x}{\partial t}+\bar{u}_x\frac{\partial u'_x}{\partial x_x}+u'_r\frac{\partial \bar{u}_x}{\partial x_r}\right]+\frac{\partial p'}{\partial x_x}&=-\frac{\partial q_s}{\partial x_x}\\
\bar{\rho}\left[\frac{\partial u'_r}{\partial t}+\bar{u}_x\frac{\partial u'_r}{\partial x_x}\right]+\frac{\partial p'}{\partial x_r}&=-\frac{\partial q_s}{\partial x_r}\\
\bar{\rho}\left[\frac{\partial u'_\phi}{\partial t}+\bar{u}_x\frac{\partial u'_\phi}{\partial x_x}\right]+\frac{1}{x_r}\frac{\partial p'}{\partial x_\phi}&=-\frac{1}{x_r}\frac{\partial q_s}{\partial x_\phi}\\
\frac{\partial p'}{\partial t}+\bar{u}_x\frac{\partial p'}{\partial x_x}+\gamma\bar{p}_\infty\left[\frac{\partial u'_x}{\partial x_x}+\frac{1}{x_r}\frac{\partial (x_r u'_r)}{\partial x_r}+\frac{1}{x_r}\frac{\partial u'_\phi}{\partial x_\phi}\right]&=0
\end{aligned}
\tag{3.11}
$$

The wave operator is now established with Eq (3.11). The next step is to solve this linear system to obtain the expression of the fluctuating pressure. This is done using Green functions. A reminder of the theory behind such functions can be found in Appendix A. A vectorial Green function $\left(u_x'^{(n)}, u_r'^{(n)}, u_\phi'^{(n)}, p'^{(n)}\right)$ is introduced.

$$
\begin{aligned}
\bar{\rho}\left[\frac{\partial u_x'^{(n)}}{\partial t}+\bar{u}_x\frac{\partial u_x'^{(n)}}{\partial x_x}+u_r'^{(n)}\frac{1}{x_r}\frac{\partial (x_r\bar{u}_x)}{\partial x_r}\right]+\frac{\partial p'^{(n)}}{\partial x_x}&=-\delta(\vec{x}_M-\vec{\xi}_S)\delta(t-t_1)\delta_{n1}\\
\bar{\rho}\left[\frac{\partial u_r'^{(n)}}{\partial t}+\bar{u}_x\frac{\partial u_r'^{(n)}}{\partial x_x}\right]+\frac{\partial p'^{(n)}}{\partial x_r}&=-\delta(\vec{x}_M-\vec{\xi}_S)\delta(t-t_1)\delta_{n2}\\
\bar{\rho}\left[\frac{\partial u_\phi'^{(n)}}{\partial t}+\bar{u}_x\frac{\partial u_\phi'^{(n)}}{\partial x_x}\right]+\frac{1}{x_r}\frac{\partial p'^{(n)}}{\partial x_\phi}&=-\delta(\vec{x}_M-\vec{\xi}_S)\delta(t-t_1)\delta_{n3}\\
\frac{\partial p'^{(n)}}{\partial t}+\bar{u}_x\frac{\partial p'^{(n)}}{\partial x_x}+\gamma\bar{\rho}\left[\frac{\partial u_x'^{(n)}}{\partial x_x}+\frac{1}{x_r}\frac{\partial (x_r u_r'^{(n)})}{\partial x_r}+\frac{1}{x_r}\frac{\partial u_\phi'^{(n)}}{\partial x_\phi}\right]&=0
\end{aligned}
\tag{3.12}
$$

The vectorial Green function is related to the state vector $\left(u'_x, u'_r, u'_\phi, p'\right)$ where $n=[1,2,3]$ is associated with the three different source terms shown in the equation above. There are no source term in the fourth equation in System (3.11) so there is no need to introduce a fourth system of equations in (3.12). The pressure fluctuations is expressed as a function of the three Green pressure fluctuations $p'^{(1)}$, $p'^{(2)}$, $p'^{(3)}$ and the source terms in Sys (3.11) using (A.7). The position of the observer $\vec{x}_M=(x_x,x_r,x_\phi)$ and the position of a source point $\vec{\xi}_S=(\xi_x,\xi_r,\xi_\phi)$ are introduced. The pressure fluctuations are then given by

$$p'(\vec{x}_M,t) = \int_{\vec{\xi}_S}\int_{t_1}\Bigg[- p'^{(1)}(\vec{x}_M,\vec{\xi}_S;t,t_1)\frac{\partial q_s}{\partial \xi_x} - p'^{(2)}(\vec{x}_M,\vec{\xi}_S;t,t_1)\frac{\partial q_s}{\partial \xi_r} - p'^{(3)}(\vec{x}_M,\vec{\xi}_S;t,t_1)\frac{1}{\xi_r}\frac{\partial q_s}{\partial \xi_\phi}\Bigg]\mathrm{d}\vec{\xi}_S\mathrm{d}t_1 \tag{3.13}$$

A Fourier transform is applied to switch into the frequency domain from the t_1 time component. The following convention has been chosen

$$p'^{(n)}(\vec{x}_M,\vec{\xi}_S;t,t_1) = \int_{-\infty}^{\infty} \hat{p}'^{(n)}(\vec{x}_M,\vec{\xi}_S;\omega)e^{-i\omega t}e^{i\omega t_1}\mathrm{d}\omega \tag{3.14}$$

$$\hat{p}'^{(n)}(\vec{x}_M,\vec{\xi}_S;\omega)e^{-i\omega t} = \frac{1}{2\pi}\int_{-\infty}^{\infty} p'^{(n)}(\vec{x}_M,\vec{\xi}_S;t,t_1)e^{-i\omega t_1}\mathrm{d}t_1 \tag{3.15}$$

The dependency in t has been taken out of the Fourier transform of the pressure fluctuations. This is done so that the time difference appears explicitly in equations. The integral expression of the pressure field is finally expressed as

$$p'(\vec{x}_M,t) = \int_{\omega}\int_{\vec{\xi}_S}\int_{t_1}\Bigg[- \hat{p}'^{(1)}(\vec{x}_M,\vec{\xi}_S;\omega)\frac{\partial q_s}{\partial \xi_x} - \hat{p}'^{(2)}(\vec{x}_M,\vec{\xi}_S;\omega)\frac{\partial q_s}{\partial \xi_r} - \hat{p}'^{(3)}(\vec{x}_M,\vec{\xi}_S;\omega)\frac{1}{\xi_r}\frac{\partial q_s}{\partial \xi_\phi}\Bigg]e^{-i\omega(t-t_1)}\mathrm{d}\omega\mathrm{d}\vec{\xi}_S\mathrm{d}t_1 \tag{3.16}$$

3.2.2 Adjoint problem

The direct computation of the vectorial Green functions $p'^{(n)}$ is not done. Instead, the adjoint problem is introduced to obtain the expression of the pressure fluctuations by searching for only one Green function rather than three. A presentation of the concept of adjoint Green functions can also be found in Appendix A. By introducing the adjoint problem using Eq (A.9), Tam and Auriault [77] presented a new system with a source term in the continuity equation but no source term in the momentum equations, making it lighter than Sys (3.11). Using as variable the adjoint Green vector in the Fourier domain $(\hat{u}'^a_x, \hat{u}'^a_r, \hat{u}'^a_\phi, \hat{p}'^a)$, the adjoint system is

$$
\begin{aligned}
\bar{\rho}\left[i\omega\hat{u}_x'^a + \bar{u}_x\frac{\partial\hat{u}_x'^a}{\partial\xi_x}\right] + \gamma\bar{\rho}\frac{\partial\hat{p}'^a}{\partial\xi_x} &= 0 \\
\bar{\rho}\left[i\omega\hat{u}_r'^a + \bar{u}_x\frac{\partial\hat{u}_r'^a}{\partial\xi_x} + \hat{u}_x'^a\frac{\partial\bar{u}}{\partial\xi_r}\right] + \gamma\bar{\rho}\frac{\partial\hat{p}'^a}{\partial\xi_r} &= 0 \\
\bar{\rho}\left[i\omega\hat{u}_\phi'^a + \bar{u}_x\frac{\partial\hat{u}_\phi'^a}{\partial\xi_x}\right] + \gamma\bar{\rho}\frac{1}{\xi_r}\frac{\partial\hat{p}'^a}{\partial\xi_\phi} &= 0 \\
i\omega\hat{p}'^a + \bar{u}_x\frac{\partial\hat{p}'^a}{\partial\xi_x} + \left[\frac{\partial\hat{u}_x'^a}{\partial\xi_x} + \frac{1}{\xi_r}\frac{\partial(\xi_r\hat{u}_r'^a)}{\partial\xi_r} + \frac{1}{\xi_r}\frac{\partial\hat{u}_\phi'^a}{\partial\xi_\phi}\right] &= -\frac{1}{2\pi}\delta(\vec{x}_M - \vec{\xi}_S)
\end{aligned}
\tag{3.17}
$$

Future calculations will show that only the last equation in Sys (3.17) is used in this work, namely

$$
i\omega\hat{p}'^a + \bar{u}_x\frac{\partial\hat{p}'^a}{\partial\xi_x} + \left[\frac{\partial\hat{u}_x'^a}{\partial\xi_x} + \frac{1}{\xi_r}\frac{\partial(\xi_r\hat{u}_r'^a)}{\partial\xi_r} + \frac{1}{\xi_r}\frac{\partial\hat{u}_\phi'^a}{\partial\xi_\phi}\right] = -\frac{1}{2\pi}\delta(\vec{x}_M - \vec{\xi}_S) \tag{3.18}
$$

This equation can be rewritten using the vector notation $\hat{\mathbf{u}}'^a = (\hat{u}_x'^a, \hat{u}_r'^a, \hat{u}_\phi'^a)$ as

$$
i\omega\hat{p}'^a + \bar{u}_x\frac{\partial\hat{p}'^a}{\partial\xi_x} + \nabla\cdot\hat{\mathbf{u}}'^a = -\frac{1}{2\pi}\delta(\vec{x}_M - \vec{\xi}_S) \tag{3.19}
$$

Additionally, Tam and Auriault used the following relations, obtained citing the Appendix A of reference [77],

$$
\begin{aligned}
\hat{p}'^{(1)}(\vec{x}_M, \vec{\xi}_S; \omega) &= \hat{u}_x'^a(\vec{\xi}_S, \vec{x}_M; \omega) \\
\hat{p}'^{(2)}(\vec{x}_M, \vec{\xi}_S; \omega) &= \hat{u}_r'^a(\vec{\xi}_S, \vec{x}_M; \omega) \\
\hat{p}'^{(3)}(\vec{x}_M, \vec{\xi}_S; \omega) &= \hat{u}_\phi'^a(\vec{\xi}_S, \vec{x}_M; \omega)
\end{aligned}
\tag{3.20}
$$

Note the inversion of the spatial variables $\vec{x}_M$ and $\vec{\xi}_S$ on each side of the equations. Eq (3.16) and Eq (3.20) are then combined to obtain

$$
p'(\vec{x}_M, t) = \int_\omega\int_{\vec{\xi}_S}\int_{t_1}\left(-\hat{u}_x'^a\frac{\partial q_s}{\partial\xi_x} - \hat{u}_r'^a\frac{\partial q_s}{\partial\xi_r} - \hat{u}_\phi'^a\frac{1}{\xi_r}\frac{\partial q_s}{\partial\xi_\phi}\right)e^{-i\omega(t-t_1)}\mathrm{d}\omega\mathrm{d}\vec{\xi}_S\mathrm{d}t_1 \tag{3.21}
$$

With the vector notation $\hat{\mathbf{u}}'^a = (\hat{u}_x'^a, \hat{u}_r'^a, \hat{u}_\phi'^a)$, the previous equation is rewritten as

$$
p'(\vec{x}_M, t) = -\int_\omega\int_{\vec{\xi}_S}\int_{t_1}\hat{\mathbf{u}}'^a\cdot\nabla q_s e^{-i\omega(t-t_1)}\mathrm{d}\omega\mathrm{d}\vec{\xi}_S\mathrm{d}t_1 \tag{3.22}
$$

Using the fact that $\nabla\cdot[\hat{\mathbf{u}}'^a q_s] = q_s\nabla\cdot\hat{\mathbf{u}}'^a + \hat{\mathbf{u}}'^a\cdot\nabla q_s$, it gives

$$p'(\vec{x}_M,t) = -\int_\omega \int_{\vec{\xi}_S} \int_{t_1} \left(\nabla\cdot[\hat{\mathbf{u}}'^a q_s] - q_s \nabla\cdot\hat{\mathbf{u}}'^a\right) e^{-i\omega(t-t_1)} \mathrm{d}\omega \mathrm{d}\vec{\xi}_S \mathrm{d}t_1 \tag{3.23}$$

$$p'(\vec{x}_M,t) = -\int_\omega \int_{\vec{\xi}_S} \int_{t_1} \nabla\cdot[\hat{\mathbf{u}}'^a q_s] e^{-i\omega(t-t_1)} \mathrm{d}\omega \mathrm{d}\vec{\xi}_S \mathrm{d}t_1 + \int_\omega \int_{\vec{\xi}_S} \int_{t_1} q_s \left(\nabla\cdot\hat{\mathbf{u}}'^a\right) e^{-i\omega(t-t_1)} \mathrm{d}\omega \mathrm{d}\vec{\xi}_S \mathrm{d}t_1 \tag{3.24}$$

The divergence theorem is then applied on the first integral. That leads to

$$p'(\vec{x}_M,t) = -\int_\omega \oiint_S \int_{t_1} \left(\hat{\mathbf{u}}'^a\cdot\vec{n}\right) q_s e^{-i\omega(t-t_1)} \mathrm{d}\omega dS \mathrm{d}t_1 + \int_\omega \int_{\vec{\xi}_S} \int_{t_1} q_s \left(\nabla\cdot\hat{\mathbf{u}}'^a\right) e^{-i\omega(t-t_1)} \mathrm{d}\omega \mathrm{d}\vec{\xi}_S \mathrm{d}t_1 \tag{3.25}$$

with $\vec{n}$ the outward normal vector to the surface S. If S is chosen as the surface containing the whole jet, the first integral is null as there is no source on S, $q_s = 0$. The expression of the pressure fluctuation is simplified to

$$p'(\vec{x}_M,t) = \int_\omega \int_{\vec{\xi}_S} \int_{t_1} q_s \left(\nabla\cdot\hat{\mathbf{u}}'^a\right) e^{-i\omega(t-t_1)} \mathrm{d}\omega \mathrm{d}\vec{\xi}_S \mathrm{d}t_1 \tag{3.26}$$

Eq (3.19) is used for an observer located outside of the jet flow, that is $\vec{x}_M \neq \vec{\xi}_S$. In this case the delta function is set to 0 and the equation is reduced to

$$\nabla\cdot\hat{\mathbf{u}}'^a = -\left(i\omega + \bar{u}_x \frac{\partial}{\partial\xi_x}\right)\hat{p}'^a \tag{3.27}$$

Inserting the previous equation in (3.26) gives

$$p'(\vec{x}_M,t) = -\int_\omega \int_{\vec{\xi}_S} \int_{t_1} q_s \left(i\omega + \bar{u}_x \frac{\partial}{\partial\xi_x}\right)\hat{p}'^a e^{-i\omega(t-t_1)} \mathrm{d}\omega \mathrm{d}\vec{\xi}_S \mathrm{d}t_1 \tag{3.28}$$

and in the time domain

$$p'(\vec{x}_M,t) = -\int_{\vec{\xi}_S} \int_{t_1} q_s \left(\frac{\partial}{\partial t_1} + \bar{u}_x \frac{\partial}{\partial\xi_x}\right) p'^a \mathrm{d}\vec{\xi}_S \mathrm{d}t_1 \tag{3.29}$$

An integration by parts according to the convective derivative is done, followed by a Fourier transform on p'^a, leading to

$$p'(\vec{x}_M,t) = \int_\omega \int_{\vec{\xi}_S} \int_{t_1} \frac{\mathrm{D}q_s}{\mathrm{D}t_1} \hat{p}'^a(\vec{\xi}_S,\vec{x}_M;\omega) e^{-i\omega(t-t_1)} \mathrm{d}\omega \mathrm{d}\vec{\xi}_S \mathrm{d}t_1 \tag{3.30}$$

with the convective derivative in the axial direction defined as

$$\frac{\mathrm{D}}{\mathrm{D}t_1} = \frac{\partial}{\partial t_1} + \bar{u}_x \frac{\partial}{\partial \xi_x} \tag{3.31}$$

Having obtained an expression of the pressure, the power spectral density of the radiated pressure field can be computed using the following formula

$$\hat{S}(\vec{x}_M, \omega) = \frac{1}{2\pi} \int_{-\infty}^{\infty} \left\langle p'(\vec{x}_M, t) p'(\vec{x}_M, t+\tau) \right\rangle e^{i\omega\tau} \mathrm{d}\tau \tag{3.32}$$

In this formula the brackets $\langle .. \rangle$ stands for the mathematical expectation. By substituting Eq (3.30) in Eq (3.32) above, the power spectral density is

$$\hat{S}(\vec{x}_M, \omega) = \frac{1}{2\pi} \int_\tau \int_{\omega_1} \int_{\omega_2} \int_{\vec{\xi}_S} \int_{\vec{\zeta}_S} \int_{t_1} \int_{t_2} \hat{p}'^a(\vec{\xi}_S, \vec{x}_M; \omega_1) \hat{p}'^a(\vec{\zeta}_S, \vec{x}_M; \omega_2) \left\langle \frac{\mathrm{D}q_s(\vec{\xi}_S, t_1)}{\mathrm{D}t_1} \frac{\mathrm{D}q_s(\vec{\zeta}_S, t_2)}{\mathrm{D}t_2} \right\rangle$$
$$e^{-i\omega_1(t-t_1)} e^{-i\omega_2((t+\tau)-t_2)} e^{i\omega\tau} \mathrm{d}\tau \mathrm{d}\omega_1 \mathrm{d}\omega_2 \mathrm{d}\vec{\xi}_S \mathrm{d}\vec{\zeta}_S \mathrm{d}t_1 \mathrm{d}t_2 \tag{3.33}$$

Only the term in q_s stays in the autocorrelation function because it contains the random part, the other terms have a deterministic feature and can be taken out. The mathematical expectation handles the integration according to the time, but t still appears in the exponents in the equation above. A change of variable $t_1 = t_1 - t$ and $t_2 = t_2 - t$ was omitted. The corrected version is

$$\hat{S}(\vec{x}_M, \omega) = \frac{1}{2\pi} \int_\tau \int_{\omega_1} \int_{\omega_2} \int_{\vec{\xi}_S} \int_{\vec{\zeta}_S} \int_{t_1} \int_{t_2} \hat{p}'^a(\vec{\xi}_S, \vec{x}_M; \omega_1) \hat{p}'^a(\vec{\zeta}_S, \vec{x}_M; \omega_2) \left\langle \frac{\mathrm{D}q_s(\vec{\xi}_S, t_1)}{\mathrm{D}t_1} \frac{\mathrm{D}q_s(\vec{\zeta}_S, t_2)}{\mathrm{D}t_2} \right\rangle$$
$$e^{i\omega_1 t_1} e^{-i\omega_2(\tau - t_2)} e^{i\omega\tau} \mathrm{d}\tau \mathrm{d}\omega_1 \mathrm{d}\omega_2 \mathrm{d}\vec{\xi}_S \mathrm{d}\vec{\zeta}_S \mathrm{d}t_1 \mathrm{d}t_2 \tag{3.34}$$

The Fourier transform of the Dirac function can be recognised in the equation above with the classical identity

$$\int_\tau e^{i(\omega-\omega_2)\tau} \mathrm{d}\tau = 2\pi\delta(\omega - \omega_2) \tag{3.35}$$

allowing the integration according to τ and subsequently according to ω_2. $\hat{S}$ is then simplified to

$$\hat{S}(\vec{x}_M, \omega) = \int_{\omega_1} \int_{\vec{\xi}_S} \int_{\vec{\zeta}_S} \int_{t_1} \int_{t_2} \hat{p}'^a(\vec{\xi}_S, \vec{x}_M; \omega_1) \hat{p}'^a(\vec{\zeta}_S, \vec{x}_M; \omega) \left\langle \frac{\mathrm{D}q_s(\vec{\xi}_S, t_1)}{\mathrm{D}t_1} \frac{\mathrm{D}q_s(\vec{\zeta}_S, t_2)}{\mathrm{D}t_2} \right\rangle$$
$$e^{i\omega_1 t_1 + i\omega t_2} \mathrm{d}\omega_1 \mathrm{d}\vec{\xi}_S \mathrm{d}\vec{\zeta}_S \mathrm{d}t_1 \mathrm{d}t_2 \tag{3.36}$$

The calculations cannot be pushed further yet. The next step is the introduction of a statistical modelling for fine scale turbulence.

3.2.3 Source modelling

The correlation function for the full convective derivative has not yet been measured but Davies *et al.* [27] and Fleury *et al.* [33] among others studied and measured the two-point space-time correlation of the fluctuating axial velocity component in jets. Tam and Auriault argued that the autocorrelation function needed should be similar to the one from Davies et al [27]. The model function used for the autocorrelation is the following

$$\left\langle \frac{\mathrm{D}q_s(\vec{\xi}_S,t_1)}{\mathrm{D}t_1}\frac{\mathrm{D}q_s(\vec{\zeta}_S,t_2)}{\mathrm{D}t_2}\right\rangle = \frac{\tilde{q}_s^2}{c^2\tau_s^2} \exp\left(-\frac{|\xi_x-\zeta_x|}{\bar{u}_x\tau_s}-\frac{\ln 2}{l_s^2}\left[[(\xi_x-\zeta_x)-\bar{u}_x(t_1-t_2)]^2+(\xi_y-\zeta_y)^2+(\xi_z-\zeta_z)^2\right]\right) \tag{3.37}$$

So when $\vec{\xi}_S \to \vec{\zeta}_S$ and $t_1 \to t_2$

$$\left\langle \left(\frac{\mathrm{D}q_s(\vec{\xi}_S,t)}{\mathrm{D}t}\right)^2\right\rangle = \frac{\tilde{q}_s^2}{c^2\tau_s^2} = \frac{I_s^2}{\tau_s^2} \tag{3.38}$$

In this expression, a few key terms need to be defined

$$\begin{aligned} \frac{\tilde{q}_s}{c} &= Aq = A\frac{2}{3}\bar{\rho}k_t = I_s \\ l_s &= c_l\frac{k_t^{3/2}}{\epsilon} \\ \tau_s &= c_\tau\frac{k_t}{\epsilon} \end{aligned} \tag{3.39}$$

Here, k_t is the turbulent kinetic energy, ϵ is the turbulent dissipation and c is a constant controlling the kinetic energy of the fine scale turbulence; l_s is the length scale of the fine scale turbulence; τ_s is the decay time; $\tilde{q}_s$ is a measure of the intensity of the temporal fluctuation of the kinetic energy of the fine scale tubulence. The adjustment constants are set by Tam and Auriault [78] to be $A = 1.5855$, $c_l = 0.256$ and $c_\tau = 0.233$. I_s, l_s and τ_s can be computed using a RANS simulation. Even though it was explained earlier with the definition of q_s in Eq (3.8) that the turbulent kinetic energy k_s used was only the one responsible for fine scale turbulence, the value used for the modelling of the sources in Eq (3.39) is directly the one given by the RANS simulation and does not take any kind of filtering on the size of the turbulent structure. Tam and Auriault argue that k_s and k_t should be proportional, hence the introduction of the adjustment constants.

The autocorrelation function presented above can be assimilated to a Gaussian function in four dimensions. It can be separated in two parts, the height of the curve's peak expressed in Eq (3.38) and the attenuation factor being the exponent. What is expressed here is that the

correlation of two source points at two given time is a function of the difference in distance between these two points and the difference between the two time-steps.

A smaller spatial difference leads to a higher correlation with a maximum being expressed in Eq. (3.38) and on the contrary a higher spatial difference will drive the correlation function to zero. The rate at which the correlation function will decrease is controled by the choice of the length scale l_s. Here this length scale is the one from the fine scale turbulence. Note that the term "fine scale" corresponds to the definition introduced by Tam and not the one from Kolmogorov. Using l_s as the length scale means that only sources within a single structure are coherent. That describes the physics well because as explained in [82], the sources responsible for the fine scale turbulence jet mixing noise is a compact source. Note that the use of Gaussian functions to describe the evolution of the coherence depending on the distance between the source points is justified empirically with measurements presented in [27]. The same analysis can be done concerning the correlation in time while noting the difference in rate of the decrease with the time difference. This is also motivated by the results of experiments presented in [27] showing that the effect on the correlation could be assimilated to an exponential decrease and not a Gaussian function. Morris and Boluriaan [57] and Miller [55] introduced similar expressions of the time-space correlation function. Despite the difference in the formulation, the modelling of the autocorrelation of the sources remains a Gaussian fit.

As for the amplitude of this correlation function, this is nothing else than a scaling of the kinetic energy over a time scale which here would be the lifetime of turbulent structures or, as describe by Tam, the decay time. Although q_s is evaluated at two separated position and time in the left hand side of Eq (3.37), $\tilde{q}_s$, τ_s and l_s are evaluated at an unspecified position and time in the right hand side. Using the compactness of sources, if two source points are close enough that their correlation is not null, the value of both the decay time and the kinetic energy should be very close. That would justify evaluating I_s, τ_s and l_s in either $(\vec{\xi}_S, t_1)$ or $(\vec{\zeta}_S, t_2)$.

The source model in Eq (3.37) is now substituted in Eq (3.36) in order to carry on with the calculations. The power spectral density $\hat{S}$ is now expressed as

$$\begin{aligned}\hat{S}(\vec{x}_M,\omega) = &\int_{\omega_1}\int_{\vec{\xi}_S}\int_{\vec{\zeta}_S}\int_{t_1}\int_{t_2} \hat{p}'^a(\vec{\xi}_S,\vec{x}_M;\omega_1)\hat{p}'^a(\vec{\zeta}_S,\vec{x}_M;\omega)\frac{I_s^2}{\tau_s^2} \\ &\exp\left(-\frac{|\xi_x-\zeta_x|}{\bar{u}_x\tau_s} - \ln 2\left[\frac{[(\xi_x-\zeta_x)-\bar{u}_x(t_1-t_2)]^2}{l_s^2}+\frac{(\xi_y-\zeta_y)^2}{l_s^2}+\frac{(\xi_z-\zeta_z)^2}{l_s^2}\right]\right) \\ &e^{i\omega_1 t_1+i\omega t_2}\mathrm{d}\omega_1\mathrm{d}\vec{\xi}_S\mathrm{d}\vec{\zeta}_S\mathrm{d}t_1\mathrm{d}t_2\end{aligned} \tag{3.40}$$

The integration according to t_1, t_2 and ω_1 is performed in Appendix C.1. A simplified expression of $\hat{S}$ is finally obtained,

$$\hat{S}(\vec{x}_M,\omega) = 2\pi\left(\frac{\pi}{\ln 2}\right)^{1/2}\int_{\vec{\xi}_S}\int_{\vec{\zeta}_S}\frac{I_s^2 l_s}{\tau_s^2\bar{u}_x}\hat{p}'^a(\vec{\xi}_S,\vec{x}_M;-\omega)\hat{p}'^a(\vec{\zeta}_S,\vec{x}_M;\omega)$$
$$\exp\left[-\frac{\omega^2 l_s^2}{(4\ln 2)\bar{u}_x^2}-\frac{|\xi_x-\zeta_x|}{\bar{u}_x\tau_s}\right]$$
$$\exp\left[-\ln 2\left[\frac{(\xi_y-\zeta_y)^2}{l_s^2}+\frac{(\xi_z-\zeta_z)^2}{l_s^2}\right]-\frac{i\omega(\xi_x-\zeta_x)}{\bar{u}_x}\right]\mathrm{d}\vec{\xi}_S\mathrm{d}\vec{\zeta}_S \tag{3.41}$$

If $\hat{p}'^a$ is known, the whole spectrum can then be computed. But this might be expensive because it would be necessary to implement a double space integration. To solve that issue, Tam and Auriault presented an approximation that will avoid the computation of the double integration and simplify it to a single integration.

3.2.4 Far-field and compactness approximations

The objective is now to introduce a way to perform analytically one of the two space integrations in order to save a lot of computing time and power. For that, two properties of the problem are used by Tam and Auriault. First, using the fact that the observer is in the far-field, one could argue that for two source points relatively close to each other, the propagation of sound waves through the shear layers would be very similar. Using geometrical acoustics, the propagation can be drawn, as pictured in Figure 3.3.

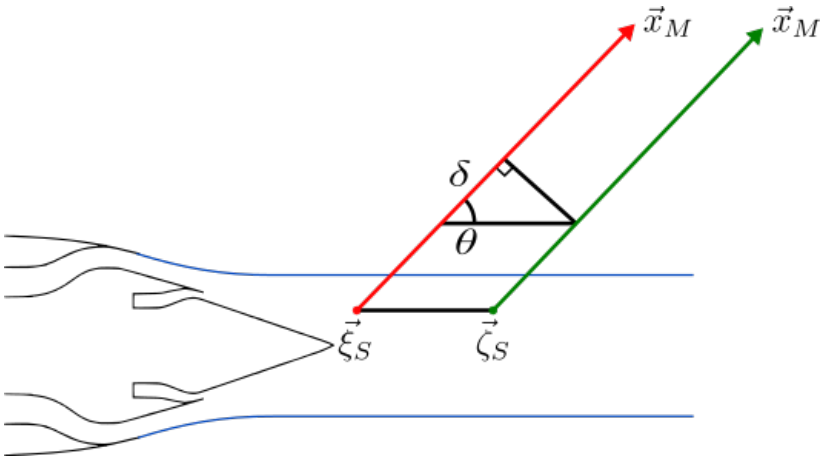

Figure 3.3: Schematic diagram showing the difference δ in ray paths between source points $\vec{\xi}_S$ and $\vec{\zeta}_S$

Noting that the propagation paths could be assimilated to be parallel, the difference between the red and green ray paths can be calculated using the difference of position of the sources in the axial direction and the polar angle θ of the observer. This difference reads $\delta = (\xi_x - \zeta_x)\cos\theta$.

In terms of propagation this difference in ray length translates to a difference of phase. From this comes the following relation between the adjoint pressure fluctuation for two nearby source points.

$$\hat{p}'^a(\vec{\xi}_S, \vec{x}_M; -\omega) = \hat{p}'^a(\vec{\zeta}_S, \vec{x}_M; -\omega) \exp\left[i \frac{\omega}{c_{ext}} \cos\theta (\xi_x - \zeta_x) \right] \tag{3.42}$$

with c_{ext} the speed of sound in the far field at $\vec{x}_M$. By the property of the Fourier transform, there is

$$\mathcal{F}\left[p'^a(\vec{\zeta}_S, \vec{x}_M; t) \right] = \hat{p}'^a(\vec{\zeta}_S, \vec{x}_M; \omega) \tag{3.43}$$

and

$$\mathcal{F}\left[p'^{a*}(\vec{\zeta}_S, \vec{x}_M; t) \right] = \hat{p}'^{a*}(\vec{\zeta}_S, \vec{x}_M; -\omega) \tag{3.44}$$

Using the fact that p'^a is real and thus $p'^{a*}(\vec{\zeta}_S, \vec{x}_M; t) = p'^a(\vec{\zeta}_S, \vec{x}_M; t)$, the two equations above are equal. The following relation is established

$$\hat{p}'^a(\vec{\zeta}_S, \vec{x}_M; \omega) = \hat{p}'^{a*}(\vec{\zeta}_S, \vec{x}_M; -\omega) \tag{3.45}$$

and with a change of variable on the pulsations

$$\hat{p}'^a(\vec{\zeta}_S, \vec{x}_M; -\omega) = \hat{p}'^{a*}(\vec{\zeta}_S, \vec{x}_M; \omega) \tag{3.46}$$

The product of adjoint pressure fluctuations can finally be simplified, giving

$$\hat{p}'^a(\vec{\xi}_S, \vec{x}_M; -\omega)\hat{p}'^a(\vec{\zeta}_S, \vec{x}_M; \omega) = |\hat{p}'^a(\vec{\zeta}_S, \vec{x}_M; \omega)|^2 \exp\left[i \frac{\omega}{c_{ext}} \cos\theta (\xi_x - \zeta_x) \right] \tag{3.47}$$

Even though this approximation is only true for two nearby source points, it can be generalised to the whole source domain. By using the compactness of the sources, the exponent in Eq (3.41) is null for two source points far from each other. The error in the propagation term is therefore rendered irrelevant because multiplied by zero. By removing the dependence in one of the source point, it allows the analytical calculation of the integral according to $\vec{\xi}_S$.

3.2.5 Propagation to the far field

The spatial integration according to $\vec{\xi}_S$ can now be performed in order to obtain a compact formulation of the noise spectrum. Eq (3.42), provided by the previous subsection, is substituted in Eq (3.41). The simplified form of the power spectral density reads

$$\hat{S}(\vec{x}_M,\omega) = 2\pi\left(\frac{\pi}{\ln 2}\right)^{1/2}\int_{\vec{\xi}_S}\int_{\vec{\zeta}_S}\frac{I_s^2 l_s}{\tau_s^2\bar{u}_x}|\hat{p}'^a(\vec{\zeta}_S,\vec{x}_M;\omega)|^2\exp\left[i\frac{\omega}{c_{ext}}\cos\theta(\xi_x-\zeta_x)\right]$$
$$\exp\left[-\frac{\omega^2 l_s^2}{(4\ln 2)\bar{u}_x^2}-\frac{|\xi_x-\zeta_x|}{\bar{u}_x\tau_s}\right]$$
$$\exp\left[-\ln 2\left[\frac{(\xi_y-\zeta_y)^2}{l_s^2}+\frac{(\xi_z-\zeta_z)^2}{l_s^2}\right]-\frac{i\omega(\xi_x-\zeta_x)}{\bar{u}_x}\right]\mathrm{d}\vec{\xi}_S\mathrm{d}\vec{\zeta}_S \tag{3.48}$$

The three integrations along the coordinates of $\vec{\xi}_S$ are performed in Appendix C.2. Eq (3.48) is finally recast as

$$\hat{S}(\vec{x}_M,\omega) = 4\pi\left(\frac{\pi}{\ln 2}\right)^{3/2}\int_{\vec{\zeta}_S}\frac{I_s^2 l_s^3}{\tau_s}|\hat{p}'^a(\vec{\zeta}_S,\vec{x}_M;\omega)|^2\frac{\exp\left[-\dfrac{\omega^2 l_s^2}{4\ln 2\bar{u}_x^2}\right]}{1+\left(1-\dfrac{\bar{u}_x}{c_{ext}}\cos\theta\right)^2\omega^2\tau_s^2}\mathrm{d}\vec{\zeta}_S \tag{3.49}$$

Eq (3.49) can be compared with the simplified form Eq (3.1), reminded below,

$$\hat{S}(\vec{x}_M,\omega) = \int_{\vec{\zeta}_S} A_S(\vec{\zeta}_S,\omega)P_S(\vec{x}_M,\vec{\zeta}_S,\omega)\mathrm{d}\vec{\zeta}_S \tag{3.50}$$

By identification, A_S and P_S can be expressed as

$$A_S(\vec{x}_M,\vec{\zeta}_S,\omega) = 4\pi\left(\frac{\pi}{\ln 2}\right)^{3/2}\frac{I_s^2 l_s^3}{\tau_s}\frac{\exp\left[-\dfrac{\omega^2 l_s^2}{4\ln 2\bar{u}_x^2}\right]}{1+\left(1-\dfrac{\bar{u}_x}{c_{ext}}\cos\theta\right)^2\omega^2\tau_s^2} \tag{3.51}$$
$$P_S(\vec{x}_M,\vec{\zeta}_S,\omega) = |\hat{p}'^a(\vec{\zeta}_S,\vec{x}_M;\omega)|^2$$

The source term can be determined from the flow properties at the source location, the pulsation and the polar angle θ of the observer. As stated above in this section, the source amplitude A_S can be computed using a RANS simulation. If an appropriate way of obtaining the adjoint pressure fluctuations is found, the propagation term P_S can also be computed and the power spectral density (PSD) in dB/Hz and as a function of the frequency would be finally obtained with

$$\hat{S}(\vec{x}_M, f) = 10 \log \left(\frac{4\pi \hat{S}(\vec{x}_M, \omega)}{p_{ref}^2} \right) \tag{3.52}$$

The main issue here is that there are no numerical tool to obtain the value of $\hat{p}'^a$ readily available and the implementation of a solver that would account for the propagation in a realistic medium would require a computing time that might not fit the industrial requirements. A new propagation model is now introduced to compute P_S in place of the adjoint approach proposed by Tam and Auriault.

3.3 Sound propagation using geometrical acoustics

Tam and Auriault provided a near-complete method for fine scale jet mixing noise prediction. However, $\hat{p}'^a$ needs to be found in order to properly obtain the noise spectra. The idea is therefore to keep the general structure of the development of the method presented in Section 3.2 but to simplify the physics in order to make it easier to compute the propagation part. First, a new description of the propagation medium is presented. Then, a new set of equation is developed, setting the ground for the introduction of geometrical acoustics. Finally the calculations are carried on to obtain a usable formula for the noise spectrum.

3.3.1 Reduction of the continuous propagation medium to two homogeneous media

One of the main challenges in solving sound propagation in a realistic medium is that every little change in terms of flow velocity and temperature has an impact on sound waves. This kind of resolution is heavy and does not comply with the requirements set in this study. At the other extreme, the medium can be simplified heavily so that the propagation can be straightforward. As an example, Brouwer and Nijboer [20] used Tam and Auriault method and applied it on a homogeneous medium. They then performed the propagation using the convected Helmholtz equation (CHE). In this case, the propagation term P_S is obtained analytically but will not account for numerous required propagation effects such as the refraction through the mixing layer or the reflection on the wing. A middle ground has to be found.

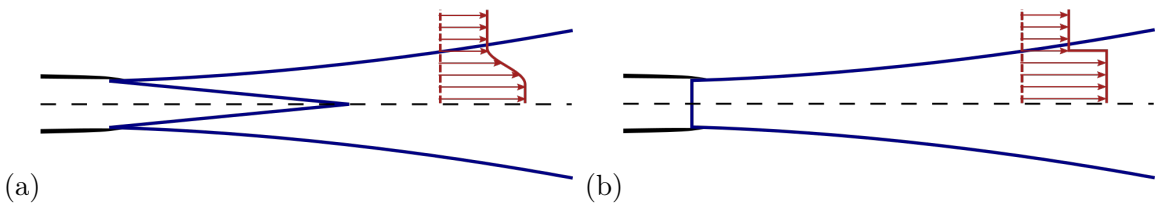

Figure 3.4: Reduction of the problem from a continuous medium to two homogeneous media

As a first estimation, two main domains of the propagation medium can be identified namely

the jet plume where the source are located and the external flow where the flight effects take place. They are separated by a smooth shear layer. A first step in the simplification of the problem is to consider these two regions as two separated media. The waves coming from sources in the jet cross an infinitely thin layer and reach the observer located in the external flow. The second part of the simplification is to consider that both media are homogeneous with their own properties and their own uniform flow. The transition from the first, realistic description of the problem to the simplified description is pictured in Fig 3.4.

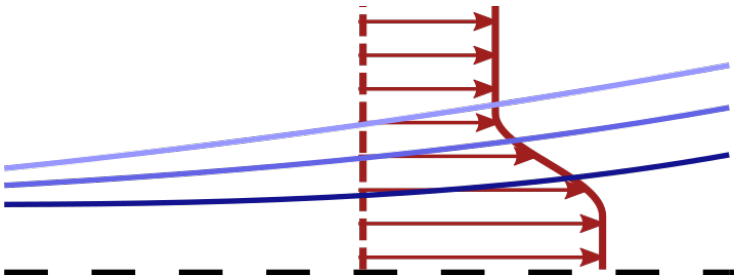

Figure 3.5: Illustration of the difficulty to locate the interface between the two artificial domains

Two main issues arise from this simplification. The first one concerns the interface used to separate the two media. It is clear that in reality the mixing layer is not infinitely thin so a criterion has to be chosen as to where the interface is set. This problem is illustrated in Fig 3.5. All the sources are assumed to be in the domain "jet" and their radiated sound waves have to pass through the mixing layer before reaching the observer. Under this consideration, the surface separating the two domains has to be set so that the whole transition region is contained in the domain "jet". The practical use of this method is explained in more details in Chapter 4.

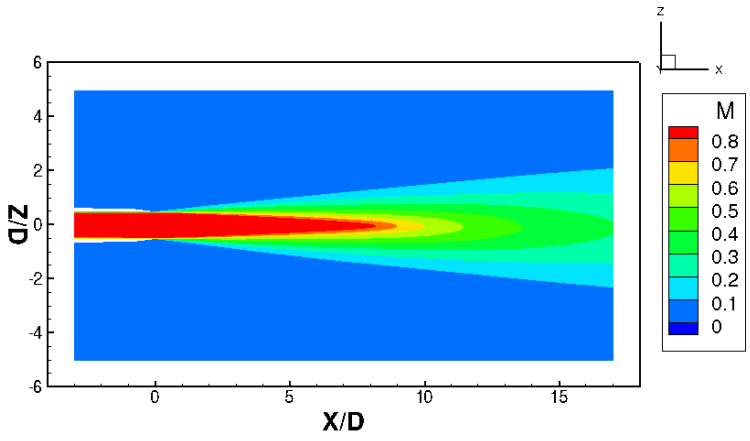

Figure 3.6: Illustration of the wide range of Mach number in the plume of a subsonic jet

The second criticism that can be made on this simplification is the choice to consider the two media to be homogeneous with a uniform mean flow. If the approximation can be easily justified for the external flow, it is hardly the case for the jet plume. Indeed, in both the axial and the radial directions there are major changes in the flow characteristics. As an example, the

map of the Mach number in the jet plume for a single jet nozzle is pictured in Fig 3.6. This might arguably be one of the main drawback of the propagation method that is developed in this section and appropriate values have to be taken as to have a description of the flow as close to reality as possible. This will be again discussed in the next chapter.

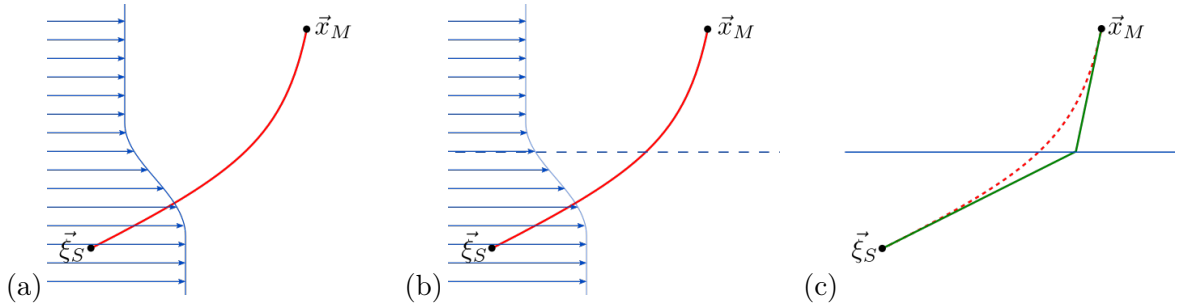

Figure 3.7: Impact on the wave path of the reduction of the problem from a continuous medium to two homogeneous media

Fig 3.7 illustrates the impact of the medium modelling on acoustic propagation. The wave path from a source point $\vec{\xi}_S$ to an observer $\vec{x}_M$ is pictured in red using geometrical acoustics in (a). Picture (b) shows how the medium is then reduced to two homogeneous media. They are separated by an infinitely thin interface located at one edge of the mixing layer as described above. Finally, considering the two new media, the wave path in green is computed. The difference between the real path and the approximated ray is pictured in (c).

Obviously, the frame of application of this method has to be carefully detailed. The theory behind this new set-up is first explained in what follows.

3.3.2 Formulation of the problem in a homogeneous by part medium

As mentioned in the previous subsection, the application of the Tam and Auriault method in a homogeneous medium has already been performed by Brouwer and Nijboer [20]. Their work is used as a starting point here. First, let's consider the jet plume, a homogeneous medium with a uniform mean flow. In the framework of Tam and Auriault study, the linearised Euler equation given by (3.9) are

$$\begin{aligned} \bar{\rho}\left[\frac{\partial u_i'}{\partial t}+\bar{u}_j\frac{\partial u_i'}{\partial x_j}+u_j'\frac{\partial \bar{u}_i}{\partial x_j}\right]+\frac{\partial p'}{\partial x_i}&=-\frac{\partial q_s}{\partial x_i} \\ \frac{\partial p'}{\partial t}+\bar{u}_j\frac{\partial p'}{\partial x_j}+\gamma\bar{p}\frac{\partial u_j'}{\partial x_j}&=0 \end{aligned} \tag{3.53}$$

For a uniform mean flow, the system reduces to

$$\begin{aligned} \bar{\rho}\frac{\mathrm{D}u_i'}{\mathrm{D}t} + \frac{\partial p'}{\partial x_i} &= -\frac{\partial q_s}{\partial x_i} \\ \frac{\mathrm{D}p'}{\mathrm{D}t} + \gamma\bar{p}\frac{\partial u_j'}{\partial x_j} &= 0 \end{aligned} \tag{3.54}$$

where the convective derivative along the mean flow is defined as

$$\frac{\mathrm{D}}{\mathrm{D}t} = \frac{\partial}{\partial t} + \bar{u}_j\frac{\partial}{\partial x_j} = \frac{\partial}{\partial t} + \bar{\mathbf{u}}\cdot\nabla \tag{3.55}$$

Taking the divergence of the momentum equation and the convective derivative of the continuity equation leads to

$$\bar{\rho}\frac{\mathrm{D}}{\mathrm{D}t}\nabla\mathbf{u}' + \nabla^2 p' = -\nabla^2 q_s \tag{3.56}$$

$$\frac{\mathrm{D}^2 p'}{\mathrm{D}t^2} + \bar{\rho}c^2\frac{\mathrm{D}}{\mathrm{D}t}\nabla\mathbf{u}' = 0 \tag{3.57}$$

where $c = \sqrt{\gamma\bar{p}/\bar{\rho}}$ is the mean speed of sound. Substracting Eq (3.56) from Eq (3.57), the convected wave equation is obtained

$$\frac{1}{c_{\text{jet}}^2}\frac{\mathrm{D}^2 p'}{\mathrm{D}t^2} - \nabla^2 p' = \nabla^2 q_s \tag{3.58}$$

with the source term $\nabla^2 q_s$ on the right hand side, and $c = c_{\text{jet}}$, see Fig 3.8.

Now let's introduce a second uniform medium around the jet corresponding to the external flow, without source. A similar development can be done giving another convected equation. It should be noted that the presence of foreign bodies in this medium such as a wing or a pylon could be taken into account by appropriate boundary conditions in a first approximation. This way, this formulation can also be used to characterise installation effects,

$$\frac{1}{c_{\text{ext}}^2}\frac{\mathrm{D}^2 p'}{\mathrm{D}t^2} - \nabla^2 p' = 0 \tag{3.59}$$

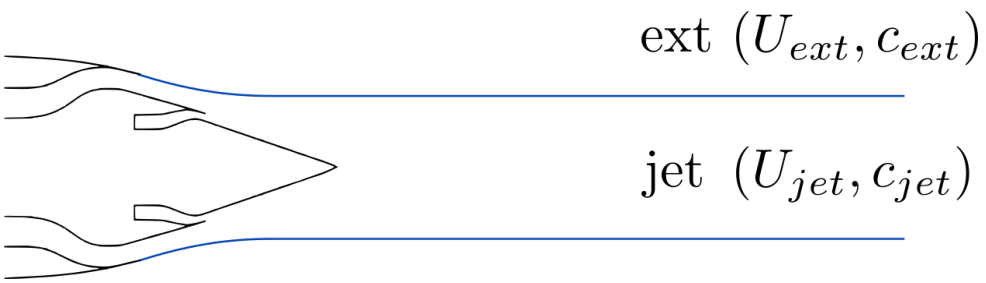

Figure 3.8: Illustration of the two homogeneous media

The association of the two media is pictured in Fig 3.8. The situation described by the

junction of these two convected Helmholtz equations is the sound propagation in a homogeneous by part medium with sources of amplitude $\nabla^2 q_s$. The resolution of this problem can be done using geometrical acoustics as presented in Appendix B. Indeed, if the wavelength is greatly inferior to the characteristic length of the problem, here the radius of the nozzle, the plane-wave approximation can be taken. That means that if $R_{jet} \gg \lambda$ the pressure in the far field can be expressed as

$$p'(\vec{x}_M, t) = \int_\omega \int_{\vec{\xi}_S} \int_{t_1} \hat{G}(\vec{x}_M, \vec{\xi}_S, \omega) e^{-i\omega(t-t_1)} \nabla^2 q_s(\vec{\xi}_S, t_1) \mathrm{d}\omega \mathrm{d}\vec{\xi}_S \mathrm{d}t_1 \tag{3.60}$$

with $\hat{G}$ the transfer function provided by geometrical acoustics. This high frequency approximation allows the asymptotic approach of the Green function to account for refraction and reflections effects and suggests that the diffraction through the mixing layer can be neglected for the considered frequency range.

Eq (3.60) is therefore an application of Eq (B.32), reminded below, for a source amplitude $I = \nabla^2 q_s$.

$$p'(\vec{x}_M, t) = \int_{\vec{\xi}_S} \int_\omega \int_{t_1} I(\vec{\xi}_S, \omega) \hat{G}(\vec{\xi}_S, \vec{x}_M; \omega) e^{-i\omega(t-t_1)} \mathrm{d}\vec{\xi}_S \mathrm{d}\omega \mathrm{d}t_1 \tag{3.61}$$

Now that the propagation part has been presented, its compatibility with the source model has to be justified. The following calculations will show how an analog formula as Eq (3.49) can be obtained. The first step is to obtain an expression similar to Eq (3.30) in order to introduce the source model as given by Tam and Auriault, in particular the following two-point space-time correlation,

$$\left\langle \frac{\mathrm{D}q_s(\vec{\xi}_S, t_1)}{\mathrm{D}t_1} \frac{\mathrm{D}q_s(\vec{\zeta}_S, t_2)}{\mathrm{D}t_2} \right\rangle \tag{3.62}$$

Applying an integration by parts twice in Eq (3.60) gives

$$p'(\vec{x}_M, t) = \int_\omega \int_{\vec{\xi}_S} \int_{t_1} \nabla^2 \hat{G}(\vec{x}_M, \vec{\xi}_S; \omega) e^{-i\omega(t-t_1)} q_s(\vec{\xi}_S, t_1) \mathrm{d}\omega \mathrm{d}\vec{\xi}_S \mathrm{d}t_1 \tag{3.63}$$

Note that the divergence is applied on $\vec{\xi}_S$, the coordinates associated with sources. Because of the high frequency approximation, only plane waves are considered. They are, by definition, solutions of the local wave equation. In this case $\vec{\xi}_S$ is taken inside the jet flow. The wave equation to consider is

$$\frac{1}{c_{jet}^2} \hat{\mathrm{D}}^2 \hat{G} = \nabla^2 \hat{G} \tag{3.64}$$

with the convective derivative in the Fourier domain,

$$\hat{\mathrm{D}} = -i\omega + \bar{\mathbf{u}}_{jet} \cdot \nabla \tag{3.65}$$

and in the time domain

$$\frac{\mathrm{D}}{\mathrm{D}t} = \frac{\partial}{\partial t} + \bar{\mathbf{u}}_{jet} \cdot \nabla \tag{3.66}$$

Inserting (3.64) in Eq (3.63) gives

$$p'(\vec{x}_M, t) = \frac{1}{c_{jet}^2} \int_\omega \int_{\vec{\xi}_S} \int_{t_1} \hat{\mathrm{D}}^2 \hat{G}(\vec{x}_M, \vec{\xi}; \omega) e^{-i\omega(t-t_1)} q_s(\vec{\xi}_S, t_1) \mathrm{d}\omega \mathrm{d}\vec{\xi}_S \mathrm{d}t_1 \tag{3.67}$$

An integration by parts allows to write

$$p'(\vec{x}_M, t) = \frac{1}{c_{jet}^2} \int_\omega \int_{\vec{\xi}_S} \int_{t_1} \hat{\mathrm{D}} \hat{G}(\vec{x}_M, \vec{\xi}_S; \omega) e^{-i\omega(t-t_1)} \frac{\mathrm{D}q_s}{\mathrm{D}t}(\vec{\xi}_S, t_1) \mathrm{d}\omega \mathrm{d}\vec{\xi}_S \mathrm{d}t_1 \tag{3.68}$$

This equation can then be put directly in parallel with Eq (3.30), reminded below,

$$p'(\vec{x}_M, t) = \int_\omega \int_{\vec{\xi}_S} \int_{t_1} \hat{p}'^a(\vec{\xi}_S, \vec{x}_M; \omega) e^{-i\omega(t-t_1)} \frac{\mathrm{D}q_s}{\mathrm{D}t}(\vec{\xi}_S, t_1) \mathrm{d}\omega \mathrm{d}\vec{\xi}_S \mathrm{d}t_1 \tag{3.69}$$

By identification, the adjoint pressure fluctuations $\hat{p}'^a$ is linked to the Green function of geometrical acoustics by

$$\hat{p}'_a(\vec{\xi}_S, \vec{x}_M, \omega) = \frac{1}{c_{jet}^2} \hat{\mathrm{D}} \hat{G}(\vec{x}_M, \vec{\xi}_S; \omega) \tag{3.70}$$

Substituting Eq (3.68) in Eq (3.32) gives the following expression of the power spectral density $\hat{S}$,

$$\begin{aligned} \hat{S}(\vec{x}_M, \omega) = \frac{1}{2\pi} \frac{1}{c_{jet}^4} \int_\tau \int_{\omega_1} \int_{\omega_2} \int_{\vec{\xi}_S} \int_{\vec{\zeta}_S} \int_{t_1} \int_{t_2} & \hat{\mathrm{D}} \hat{G}(\vec{x}_M, \vec{\xi}_S; \omega_1) \hat{\mathrm{D}} \hat{G}(\vec{x}_M, \vec{\zeta}_S; \omega_2) \\ & \left\langle \frac{\mathrm{D}q_s(\vec{\xi}_S, t_1)}{\mathrm{D}t_1} \frac{\mathrm{D}q_s(\vec{\zeta}_S, t_2)}{\mathrm{D}t_2} \right\rangle \\ & e^{i\omega_1 t_1} e^{-i\omega_2(\tau - t_2)} e^{i\omega\tau} \mathrm{d}\tau \mathrm{d}\omega_1 \mathrm{d}\omega_2 \mathrm{d}\vec{\xi}_S \mathrm{d}\vec{\zeta}_S \mathrm{d}t_1 \mathrm{d}t_2 \end{aligned} \tag{3.71}$$

The integration according to τ and ω_2 are performed using the Fourier transform of the Dirac function given in Eq (3.35). A simplified expression of $\hat{S}$ is obtained,

$$\begin{aligned} \hat{S}(\vec{x}_M, \omega) = \frac{1}{c_{jet}^4} \int_{\omega_1} \int_{\vec{\xi}_S} \int_{\vec{\zeta}_S} \int_{t_1} \int_{t_2} & \hat{\mathrm{D}} \hat{G}(\vec{x}_M, \vec{\xi}_S; \omega_1) \hat{\mathrm{D}} \hat{G}(\vec{x}_M, \vec{\zeta}_S; \omega) \left\langle \frac{\mathrm{D}q_s(\vec{\xi}_S, t_1)}{\mathrm{D}t_1} \frac{\mathrm{D}q_s(\vec{\zeta}_S, t_2)}{\mathrm{D}t_2} \right\rangle \\ & e^{i\omega_1 t_1 + i\omega t_2} \mathrm{d}\omega_1 \mathrm{d}\vec{\xi}_S \mathrm{d}\vec{\zeta}_S \mathrm{d}t_1 \mathrm{d}t_2 \end{aligned} \tag{3.72}$$

Eq (B.31) is susbstituted in Eq (3.72) to highlight the ray paths connecting $\vec{\xi}_S$ and $\vec{x}_M$.

$$\hat{S}(\vec{x}_M,\omega)=\frac{1}{c_{jet}^4}\int_{\omega_1}\int_{\vec{\xi}_S}\int_{\vec{\zeta}_S}\int_{t_1}\int_{t_2}\left[\hat{\mathrm{D}}\sum_{r=1}^{N(\vec{\xi}_S)}\hat{G}_r(\vec{x}_M,\vec{\xi}_S;\omega_1)\right]\left[\hat{\mathrm{D}}\sum_{r=1}^{N(\vec{\zeta}_S)}\hat{G}_r(\vec{x}_M,\vec{\zeta}_S;\omega)\right]\left\langle\frac{\mathrm{D}q_s(\vec{\xi}_S,t_1)}{\mathrm{D}t_1}\frac{\mathrm{D}q_s(\vec{\zeta}_S,t_2)}{\mathrm{D}t_2}\right\rangle e^{i\omega_1 t_1+i\omega t_2}\mathrm{d}\omega_1\mathrm{d}\vec{\xi}_S\mathrm{d}\vec{\zeta}_S\mathrm{d}t_1\mathrm{d}t_2 \tag{3.73}$$

Tam and Auriault have introduced a source model using a unique length scale l_s for the three directions. This view is not shared by all the aeroacoutics community. As an example, Fleury *et al.* [33] measured a factor two between the transverse and axial length scales in the case of the isotropic turbulence. The following expression of the autocorrelation function with different length scales is used instead.

$$\left\langle\frac{\mathrm{D}q_s(\vec{\xi}_S,t_1)}{\mathrm{D}t_1}\frac{\mathrm{D}q_s(\vec{\zeta}_S,t_2)}{\mathrm{D}t_2}\right\rangle=\frac{I_s^2}{\tau_s^2}\exp\left(-\frac{|\xi_x-\zeta_x|}{\bar{u}_x\tau_s}-\ln 2\left[\frac{[(\xi_x-\zeta_x)-\bar{u}_x(t_1-t_2)]^2}{l_x^2}+\frac{(\xi_y-\zeta_y)^2}{l_y^2}+\frac{(\xi_z-\zeta_z)^2}{l_z^2}\right]\right) \tag{3.74}$$

Although more advanced modelling have been introduced in Sec 2.4.2, the scaling parameters I_s, l_i and τ_s are computed using the classical formulation presented in Eq (2.38). New formulations could be used in future improvements of the method. The calculations used to go from Eq (3.40) to Eq (3.41), detailed in Appendix C.1, are again performed. Hence,

$$\hat{S}(\vec{x}_M,\omega)=2\pi\left(\frac{\pi}{\ln 2}\right)^{1/2}\int_{\vec{\xi}_S}\int_{\vec{\zeta}_S}\frac{I_s^2 l_x}{\tau_s^2\bar{u}_x c_{jet}^4}\left[\hat{\mathrm{D}}\sum_{r=1}^{N(\vec{\xi}_S)}\hat{G}_r(\vec{x}_M,\vec{\xi}_S;-\omega)\right]\left[\hat{\mathrm{D}}\sum_{r=1}^{N(\vec{\zeta}_S)}\hat{G}_r(\vec{x}_M,\vec{\zeta}_S;\omega)\right]\exp\left[-\frac{\omega^2 l_x^2}{(4\ln 2)\bar{u}_x^2}-\frac{|\xi_x-\zeta_x|}{\bar{u}_x\tau_s}\right]\exp\left[-\ln 2\left[\frac{(\xi_y-\zeta_y)^2}{l_y^2}+\frac{(\xi_z-\zeta_z)^2}{l_z^2}\right]-\frac{i\omega(\xi_x-\zeta_x)}{\bar{u}_x}\right]\mathrm{d}\vec{\xi}_S\mathrm{d}\vec{\zeta}_S \tag{3.75}$$

It is not yet possible to jump forward to Eq (3.49) with the updated propagation term because the simplifications due to the far field and compactness approximations are not straightforward. In this case there are several key differences, one being that the rays are not straight anymore. There might also be several rays from one single source that could reach the observer. Such a

case is pictured in Fig 3.9.

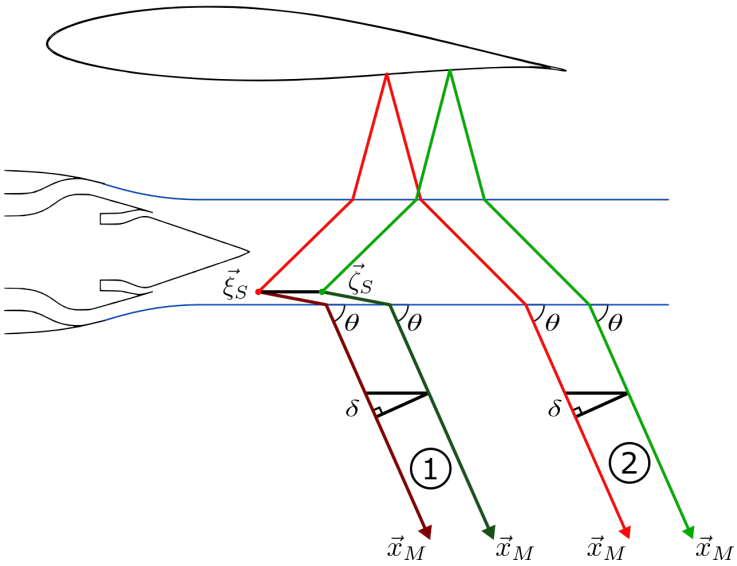

Figure 3.9: Illustration of the difference in multiple ray paths between two source points $\vec{\xi}_S$ and $\vec{\zeta}_S$ perceived by a far-field observer $\vec{x}_M$ in the case of an installed configuration

In this case, it is fair to consider that for two sources close enough to each other, all the rays reaching $\vec{x}_M$ can be paired. This is presented in Fig 3.9 by the pairs between the refracted rays and the reflected rays. For each pair, the paths are of equal lengths except for the last segment. Given that the observer is located in the far field, all the last segments have the same polar angle of θ from the jet axis. Therefore, the path difference for each pair is δ, refer to Fig 3.3.

In Morris and Boluriaan [57], a more general, 3D version of the approximation is proposed.

$$\hat{p}^a(\vec{\xi}_S, \vec{x}_M; -\omega) = \hat{p}^a(\vec{\zeta}_S, \vec{x}_M; -\omega) \exp\left(i \frac{\omega}{c_{ext} \|\vec{x}_M\|} \vec{x}_M \cdot \vec{\eta}_S \right) \tag{3.76}$$

with $\vec{\eta}_S = \vec{\xi}_S - \vec{\zeta}_S$. The developped expression of the phase jump is

$$\begin{aligned} \exp\left(i \frac{\omega}{c_{ext} \|\vec{x}_M\|} \vec{x}_M \cdot \vec{\eta}_S \right) = \exp\Bigg[i \frac{\omega}{c_{ext}} \Big(& \cos\theta(\xi_x - \zeta_x) \\ & + \sin\theta\cos\phi(\xi_y - \zeta_y) \\ & + \sin\theta\sin\phi(\xi_z - \zeta_z) \Big) \Bigg] \end{aligned} \tag{3.77}$$

That expression will be used here. $\hat{G}_1$ and $\hat{G}_2$ are the Green functions of geometrical acoustics associated with respectively the refracted rays noted 1 and the reflected rays noted 2. The relation between the Green functions of two nearby points is expressed as follows.

$$\hat{G}_1(\vec{x}_M, \vec{\xi}_S; -\omega) = \hat{G}_1(\vec{x}_M, \vec{\zeta}_S; -\omega) \exp\left(i \frac{\omega}{c_{ext} \|\vec{x}_M\|} \vec{x}_M \cdot \vec{\eta}_S \right) \tag{3.78}$$

$$\hat{G}_2(\vec{x}_M, \vec{\xi}_S; -\omega) = \hat{G}_2(\vec{x}_M, \vec{\zeta}_S; -\omega) \exp\left(i \frac{\omega}{c_{ext} \|\vec{x}_M\|} \vec{x}_M \cdot \vec{\eta}_S \right) \tag{3.79}$$

$$\begin{aligned} \hat{G}_1(\vec{x}_M, \vec{\xi}_S; -\omega) + \hat{G}_2(\vec{x}_M, \vec{\xi}_S; -\omega) = \left(\hat{G}_1(\vec{x}_M, \vec{\zeta}_S; -\omega) + \hat{G}_2(\vec{x}_M, \vec{\zeta}_S; -\omega) \right) \\ \exp\left(i \frac{\omega}{c_{ext} \|\vec{x}_M\|} \vec{x}_M \cdot \vec{\eta}_S \right) \end{aligned} \tag{3.80}$$

In the general case, one has,

$$\sum_{r=1}^{N(\vec{\xi}_S)} \hat{G}_r(\vec{x}_M, \vec{\xi}_S; -\omega) = \left(\sum_{r=1}^{N(\vec{\zeta}_S)} \hat{G}_r(\vec{x}_M, \vec{\zeta}_S; -\omega) \right) \exp\left(i \frac{\omega}{c_{ext} \|\vec{x}_M\|} \vec{x}_M \cdot \vec{\eta}_S \right) \tag{3.81}$$

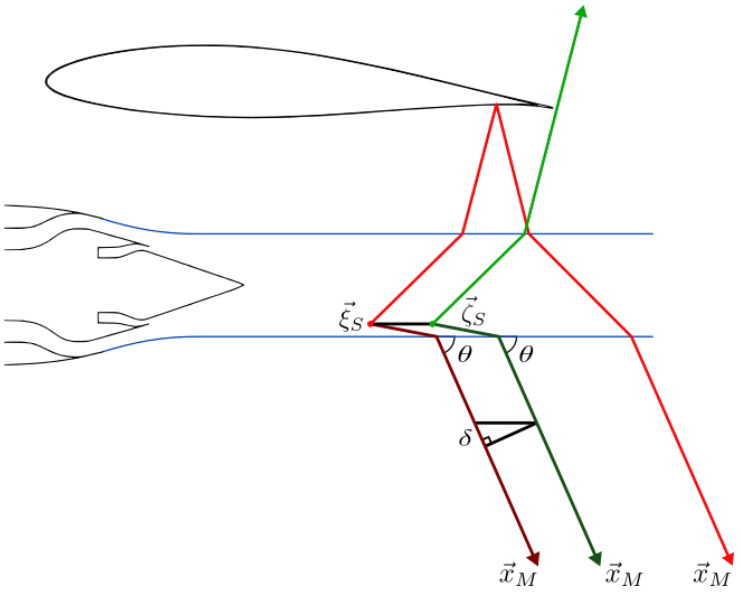

Figure 3.10: Illustration of an extreme case where two sources close to each other do not have matching rays

In some extreme cases, the rays coming from two nearby sources cannot be paired. An example is pictured in Figure 3.10 with the case of one ray reflecting just before the tip of the wing and one ray missing the wing. It is chosen to neglect these particular cases considering the rarity of these events and also the small size of correlation scales. Using the identity established in Eq (3.46)

$$\sum_{r=1}^{N(\vec{\zeta}_S)} \hat{G}_r(\vec{x}_M, \vec{\zeta}_S; -\omega) = \sum_{r=1}^{N(\vec{\zeta}_S)} \hat{G}_r^*(\vec{x}_M, \vec{\zeta}_S; \omega) \tag{3.82}$$

In Eq (3.75), the power spectral density $\hat{S}$ can be expressed using only one source coordinates with

$$\begin{aligned}\hat{S}(\vec{x}_M, \omega) =& 2\pi \left(\frac{\pi}{\ln 2}\right)^{1/2} \int_{\vec{\xi}_S} \int_{\vec{\zeta}_S} \frac{I_s^2 l_x}{\tau_s^2 \bar{u}_x c_{jet}^4} \left| \hat{\mathrm{D}} \sum_{r=1}^{N(\vec{\zeta}_S)} \hat{G}_r(\vec{x}_M, \vec{\zeta}_S; \omega) \right|^2 \\ & \exp\left[i \frac{\omega}{c_{ext}} \left(\cos\theta(\xi_x - \zeta_x) + \sin\theta\cos\phi(\xi_y - \zeta_y) + \sin\theta\sin\phi(\xi_z - \zeta_z) \right) \right] \\ & \exp\left[-\frac{\omega^2 l_x^2}{(4\ln 2)\bar{u}_x^2} - \frac{|\xi_x - \zeta_x|}{\bar{u}_x \tau_s} \right] \\ & \exp\left[-\ln 2 \left[\frac{(\xi_y - \zeta_y)^2}{l_y^2} + \frac{(\xi_z - \zeta_z)^2}{l_z^2} \right] - \frac{i\omega(\xi_x - \zeta_x)}{\bar{u}_x} \right] \mathrm{d}\vec{\xi}_S \mathrm{d}\vec{\zeta}_S \end{aligned} \tag{3.83}$$

The integration according to $\vec{\xi}_S$ is similar to the developments performed in Eq (3.48). The calculations are presented in Appendix C.3. The resulting formula for the PSD of the radiated noise using geometrical acoustics is

$$\begin{aligned}\hat{S}(\vec{x}_M, \omega) = 4\pi \left(\frac{\pi}{\ln 2}\right)^{3/2} & \int_{\vec{\zeta}_S} \frac{I_s^2 l_x l_y l_z}{\tau_s c_{jet}^4} \left| \hat{\mathrm{D}} \sum_{r=1}^{N(\vec{\zeta}_S)} \hat{G}_r(\vec{x}_M, \vec{\zeta}_S; \omega) \right|^2 \\ & \frac{\exp\left[-\frac{\omega^2}{4\ln 2 \bar{u}_x^2} \left(l_x^2 + \frac{\bar{u}_x^2}{c_{ext}^2} [l_y^2 \sin^2\theta\cos^2\phi + l_z^2 \sin^2\theta\sin^2\phi] \right) \right]}{1 + \left(1 - \frac{\bar{u}_x}{c_{ext}}\cos\theta\right)^2 \omega^2 \tau_s^2} \mathrm{d}\vec{\zeta}_S \end{aligned} \tag{3.84}$$

Eq (3.84) can now be put in parallel with the simplified form introduced in Eq (3.1), reminded below,

$$\hat{S}(\vec{x}_M, \omega) = \int_{\vec{\zeta}_S} A_S(\vec{\zeta}_S, \omega) P_S(\vec{x}_M, \vec{\zeta}_S, \omega) \mathrm{d}\vec{\zeta}_S \tag{3.85}$$

The new formulation of the source term is almost identical to the formulation from Tam and Auriault. The minor differences come from the use of a more complete version of the far-field and compactness approximations as well as the use of different length scales of the fine scale

tubulence in the three directions. The source term A_S is, respectively for Tam and Auriault,

$$A_S(\vec{x}_M, \vec{\zeta}_S, \omega) = 4\pi \left(\frac{\pi}{\ln 2}\right)^{3/2} \frac{I_s^2 l_s^3}{\tau_s} \frac{\exp\left[-\dfrac{\omega^2 l_s^2}{4 \ln 2 \bar{u}_x^2}\right]}{1 + \left(1 - \dfrac{\bar{u}_x}{c_{ext}} \cos\theta\right)^2 \omega^2 \tau_s^2} \tag{3.86}$$

and its updated form,

$$\begin{aligned} A_S(\vec{x}_M, \vec{\zeta}_S, \omega) =& 4\pi \left(\frac{\pi}{\ln 2}\right)^{3/2} \frac{I_s^2 l_x l_y l_z}{\tau_s} \\ & \frac{\exp\left[-\dfrac{\omega^2}{4 \ln 2 \bar{u}_x^2} \left(l_x^2 + \dfrac{\bar{u}_x^2}{c_{ext}^2} [l_y^2 \sin^2\theta \cos^2\phi + l_z^2 \sin^2\theta \sin^2\phi]\right)\right]}{1 + \left(1 - \dfrac{\bar{u}_x}{c_{ext}} \cos\theta\right)^2 \omega^2 \tau_s^2} \end{aligned} \tag{3.87}$$

As for the propagation

$$P_S(\vec{x}_M, \vec{\zeta}_S, \omega) = |\hat{p}^a(\vec{\zeta}_S, \vec{x}_M; \omega)|^2 \tag{3.88}$$

and its new form, using geometrical acoustics,

$$P_S(\vec{x}_M, \vec{\zeta}_S, \omega) = \frac{1}{c_{jet}^4} \left| \hat{\mathrm{D}} \sum_{r=1}^{N(\vec{\zeta}_S)} \hat{G}_r(\vec{x}_M, \vec{\zeta}_S; \omega) \right|^2 = \frac{1}{c_{jet}^4} \left| \hat{\mathrm{D}} \hat{G}(\vec{x}_M, \vec{\zeta}_S; \omega) \right|^2 \tag{3.89}$$

A new method for the prediction of fine scale jet mixing noise has been developed. In the framework of the model established by Tam and Auriault, the adjoint Green function has been replaced by a numerical calculation based on geometrical acoustics. It will be shown in the next chapter that the implementation of the ray tracing to determine P_S can be very efficient.

4 Application of the TAGA model

A new model for jet mixing noise has been developed in the previous chapter. It has been chosen to name it **TAGA** since its formulation is based on the **T**am and **A**uriault source model and **G**eometrical **A**coustics for the propagation. The objective of this chapter is to evaluate the accuracy of noise predictions provided by the TAGA model. A description of the implementation of the model is first presented. Then, a study on installation effects is performed for a cold jet. Finally, the model is used on a more realistic nozzle to study refraction effects and the impact of chevrons.

4.1 Implementation

In this section, the practical application of the TAGA model is described. In particular are discussed the assumptions used in Chapter 3 to build the model. The ray tracing tool Acti-HF is also presented as well as some validation.

4.1.1 Reduction of the problem to two homogeneous media

In Sec 3.3 was presented how the propagation medium is reduced to two homogeneous media. Two issues have been raised. The interface location between the jet and the external medium is first addressed, then the homogenisation of both media is explained.

4.1.1.1 Introduction of the artificial jet surface

The mixing layer is seen as the surface containing all the sources and is built following this definition. This choice is justified by the fact that if sources are outside of this surface, their acoustic field will not be attenuated by the refraction through the interface. Poor results are then obtained. Fig 4.1 shows all the sources contributing for at least one frequency in the noise spectrum. This domain is contained in a surface of revolution shown in green in Fig 4.2. For now the surface is manually created for each case. This process must be automated.

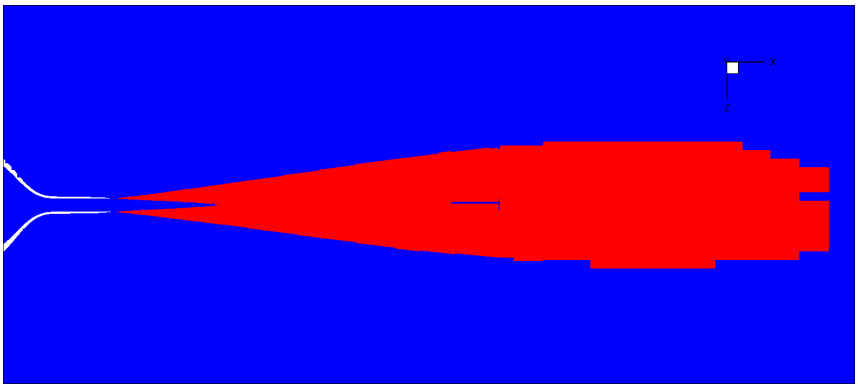

Figure 4.1: Representation of the filtered source domain in red

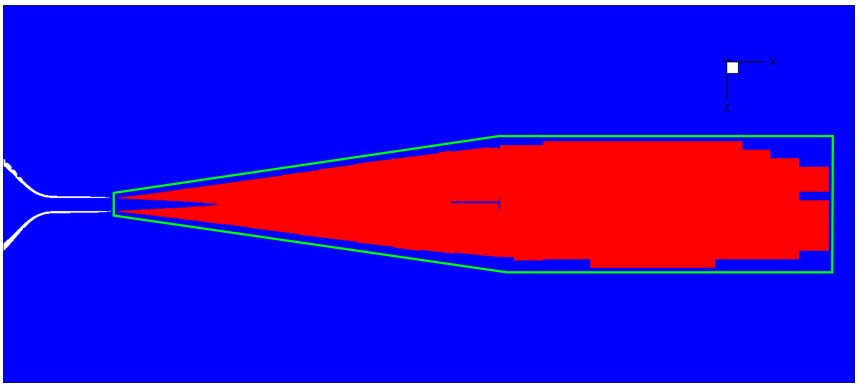

Figure 4.2: Representation of the artificial jet mixing layer in green containing the source domain in red

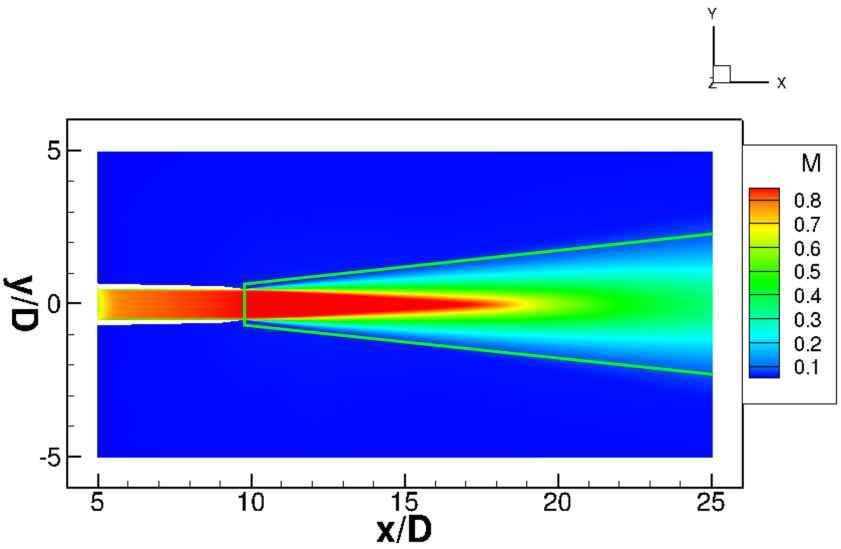

Figure 4.3: Mach number in the flow

4.1.1.2 Definition of the homogeneous jet plume

The second issue concerns the approximation of the jet flow by homogeneous media. Fig 4.3 shows the Mach number of a subsonic jet determined by a RANS computation, the solid line marks the delimitation between the two media. The simplification of the external medium is straightforward because external flow is assumed to be homogeneous. In the second medium, the flow is not homogeneous and varies over short distances. For example, the Mach number at the nozzle exhaust is 0.9 but decreases to about 0.5 after the potential core.

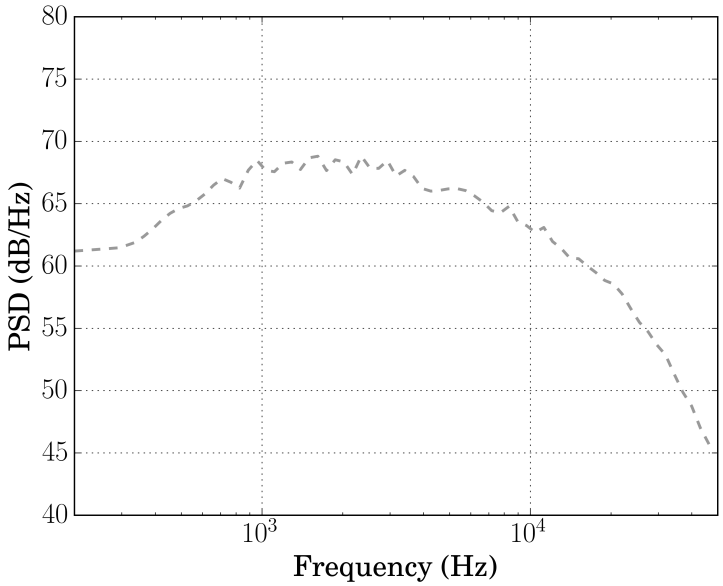

Figure 4.4: Experimental measurements of the PSD at $\theta = 90°$ and $\phi = 180°$ for the isolated case at $M = 0.9$

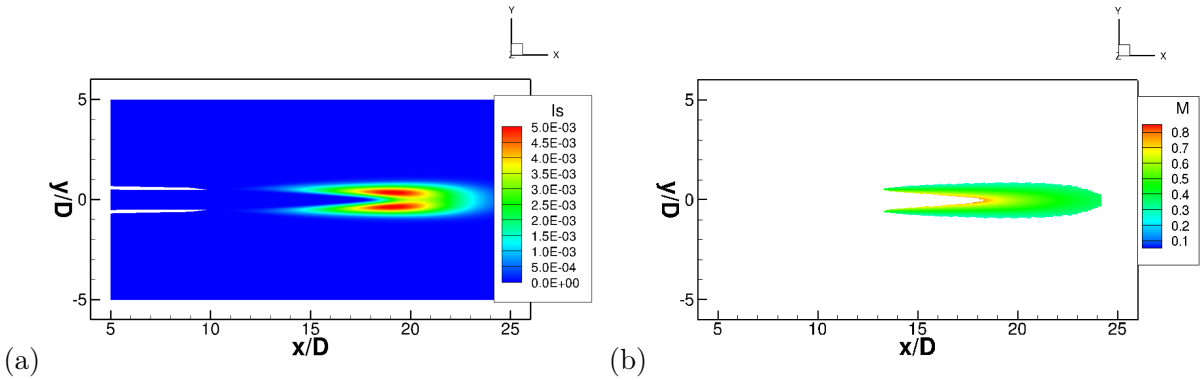

Figure 4.5: (a) Sources amplitude at $f = 2000\,\text{Hz}$ (b) Corresponding Mach number in the source domain

In order to assign one single value for the Mach number in the inner domain, the most valuable part of the jet plume is identified. Fig 4.4 shows an example of spectrum for the single jet configuration in the isolated case at $M = 0.9$ with an observer located at $\theta = 90°$ and $\phi = 180°$. The top of the curve is located at 2000 Hz. The source domain at this peak frequency is shown in

Fig 4.5 (a). Picture (b) shows the Mach number M in this source domain. At this location, M is relatively constant at around $M \simeq 0.5$. It is naturally chosen to define a homogeneous medium, with a flow at $M = 0.5$ in the $\vec{x}$ direction.

4.1.2 Numerical computation of the rays

4.1.2.1 Introduction of Acti-HF

Acti-HF is a tool tracing rays inside media that are homogeneous by parts. Each medium is described by a prescribed value for the pressure, the temperature and the velocity in each direction.

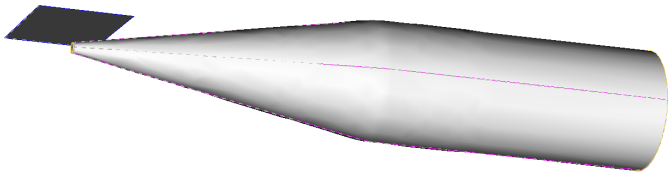

Figure 4.6: Example of an Acti-HF project set up with two surfaces: a jet and a flat plate.

Surfaces and edges are introduced to model interfaces between media or to model solid entities. The surfaces are defined according to their nature and interactions allowed with rays. For example, the surface corresponding to a wing is set as perfectly reflective. The surface corresponding to the mixing layer is however set as permeable but non reflective to neglect the latter contribution. The edges can themselves be set as diffracting or not. Fig 4.6 provides an illustration with two surfaces for the jet and a plate.

For simplicity the term event is used to designate either a reflection (R), refraction (T) or diffraction (D). The rays are computed using predetermined path instructions imposing the nature and the order of the events during the propagation. For example, if the path T is taken into account, only the rays encountering a unique refraction are computed. That corresponds to the isolated case. If the path T*R is also included, the rays passing through the mixing layer and then reflecting on the wing are taken into account. This would be used in an installed configuration. Any number of events and in any particular order can be instructed but computing time increases exponentially with the number of events.

The sources are introduced using their position, amplitude, phase and directivity. In this model, the source description is handled by the source term A_S obtained using Tam and Auriault [78]. The sources are set as monopoles of unitary amplitude. The observers are finally introduced by their coordinates.

Acti-HF does not provide access to the intermediate value of $\hat{G}$ but directly to the value of $\hat{p}$. Using Eq (B.16), if I is set to 1, the value of $\hat{p}$ and $\hat{G}$ are equal baring a change in units.

A numerical convective derivative is then applied to $\hat{G}$ to obtain the value of P_S, based on Eq (3.89).

4.1.2.2 Validation of Acti-HF

The ray tracing module is validated with two academic cases. The refracted angles θ_t given by Acti-HF are compared with the predictions by the Snell Law (B.3). In the second case, the reflected angles θ_r given by Acti-HF are compared with the theoretical value $\theta_r = \theta_i$.

The first case is built using a cylinder of diameter D in the $\vec{x}$ direction separating two media. The medium inside the cylinder is denoted "jet" and the medium outside, "ext". Four configurations are considered with the velocities and speed of sound either equal or different between the two media. In the full case, $V_{\text{jet}} = 291\,\text{m}\,\text{s}^{-1}$ and $V_{\text{ext}} = 91\,\text{m}\,\text{s}^{-1}$ for the jet and the external flow both in the $\vec{x}$ direction. The speed of sound used are respectively $c_{\text{jet}} = 368\,\text{m}\,\text{s}^{-1}$ and $c_{\text{ext}} = 333\,\text{m}\,\text{s}^{-1}$. This gives the Mach numbers $M_{\text{jet}} = 0.79$ and $M_{\text{ext}} = 0.28$, which are realistic values for a jet at take-off. Planes of sources are introduced at several axial positions and a polar arc of observers is also taken. There are between 250 and 300 rays depending on the case. The maximum of the error between the predicted refracted angle θ_t and their respective value as given by the Snell law are is given in Table 4.1. A very good agreement is found for all cases with a maximum error of less than 0.1°.

	$c_{\text{jet}} = c_{\text{ext}}$ $V_{\text{jet}} = V_{\text{ext}}$	$c_{\text{jet}} = c_{\text{ext}}$ $V_{\text{jet}} \neq V_{\text{ext}}$	$c_{\text{jet}} \neq c_{\text{ext}}$ $V_{\text{jet}} = V_{\text{ext}}$	$c_{\text{jet}} \neq c_{\text{ext}}$ $V_{\text{jet}} \neq V_{\text{ext}}$
$\Delta\theta_{\max}$	0.0025	0.025	0.06	0.08

Table 4.1: Maximum error in degrees between the predicted refracted angle and the theoretical one

The second test case is built using the same source and observer distribution without cylinder. A flat plate is introduced at $2\,D$. Two configurations are considered with a case at rest, meaning $V_{\text{ext}} = 0$ and a case with an external flow with $V_{\text{ext}} = 91\,\text{m}\,\text{s}^{-1}$, $c_{\text{ext}} = 333\,\text{m}\,\text{s}^{-1}$, giving $M_{\text{ext}} = 0.28$. IThe maximum of the error between the predicted reflected angle θ_r and their respective incident angle θ_i are plotted in Table 4.1. There is a good agreement for every ray considered with a maximum error of less than 10^{-4} °.

	$V_{\text{ext}} = 0$	$V_{\text{ext}} \neq 0$
$\Delta\theta_{\max}$	0.0001	0.0001

Table 4.2: Maximum error in degrees between the predicted reflected angle and the theoretical one

Acti-HF is compared to the analytical solution in free field. The same test case used to validate the refraction angle is used as a reference. The medium jet is set equal to the external medium while still separated by an interface. The agreement is very good for every ray with a maximum error of less than 10^{-7}%.

No comparison was performed against other noise prediction tools, due to prior validations of the code [49]. Comparisons with predictions made using SAbrinA [67] from ONERA have been carried out. The test case aimed at the study of the refraction of sound through a plane interface between two moving media. Additional evaluations were performed on a benchmark problem done in collaboration with ISVR [65]. The topic of the scattering of sound by a uniform jet was studied. Although these two test cases do not describe exactly the configuration addressed here, it is believed that the ray tracing computations is well validated.

4.2 Cold jet from a single convergent nozzle

4.2.1 Isolated subsonic jet

4.2.1.1 Description of the configuration

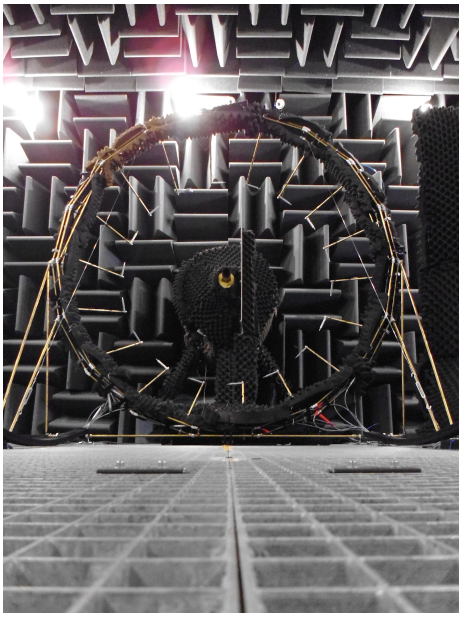

Figure 4.7: Experimental setup of the installed jet at the PPRIME Institute.

The configuration used is an isothermal jet associated with a flat plate, see Fig 4.7. The experiments were conducted in the Bruit et Vent anechoic facility of the PPRIME Institute, Poitiers, France. The jet nozzle diameter is $D = 0.05\,\mathrm{m}$ The flat plate is rectangular with a span of $15\,D$ and a chord of $9\,D$. The plate is positioned, in the axial direction, from $x_{\min} = -5\,D$ to $x_{\max} = 4\,D$ and in the radial direction, at $2\,D$ from the jet centerline, towards the azimuthal angle $\phi = 90°$. At this distance the plate is not interacting with the jet flow. An azimuthal array of microphones along an arc of radius $14.2\,D$ is used with a discretisation of $\Delta\phi = 20°$. The array ranges from $x_{\min} = -2.5\,D$ to $x_{\max} = 39\,D$. The equivalent span is $\theta_{\min} = 80°$ and $\theta_{\max} = 160°$. The orientation of the polar angle is defined using the convention provided in Fig 4.8. For an observer $\vec{x}_M$, $\theta = 180°$ if $x_r = 0$ and $x_x > 0$. Measurements are available for $M_{\text{jet}} = [0.4; 0.6; 0.8; 0.9]$. The speed of sound is $347\,\mathrm{m\,s^{-1}}$. More details can be found in

Piantanida *et al.* [63].

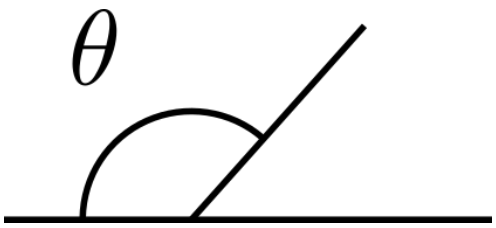

Figure 4.8: Convention for the definition of the polar angle θ.

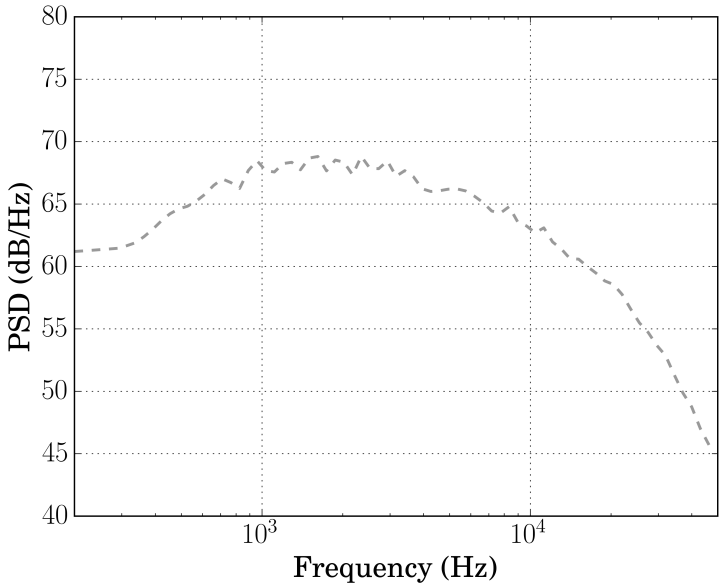

Figure 4.9: Experimental measurements of the PSD at $\theta = 90°$ and $\phi = 180°$ for the isolated case at $M = 0.9$.

The theoretical limit of the application of geometrical acoustics is $R_{\text{jet}} \gg \lambda$ which would translate in terms of frequency to $f \gg 14\,\text{kHz}$. Fig 4.9 shows an example of spectrum for the isolated configuration at $M = 0.9$ with an observer located at $\theta = 90°$ and $\phi = 180°$. The top of the curve is located approximately at $f = 2\,\text{kHz}$, equivalent to $St = 0.32$. If the high frequency criterion is applied as is, the propagation method is not valid on the frequency range of interest here. This frequency criterion is however very restrictive in practice and geometrical acoustics appears to be valid over a larger frequency range [70] [39]. In the present work, the propagation step is performed with geometrical acoustics on the whole frequency range. Weaknesses are thus to be expected at low frequencies. Let's define a criterion coefficient . It can be assumed that the accuracy of the propagation model is linked to how small $\epsilon_\lambda = \lambda / R_{\text{jet}}$ is. The present study also tries to evaluate the maximum value for the high frequency criterion for which the developed method still holds.

4.2.1.2 RANS inputs

The RANS solver used to compute the base flows is FLUSEPA [1]. It is the unstructured finite-volume solver developed for 30 years by the ArianeGroup company to calculate compressible, multidimensional, unsteady, viscous and reactive flows over bodies in relative motion. The space integration is based on a Godunov's type unstructured finite volume method suitable for highly compressible turbulent scale-resolving simulations around complex geometries and constructed by using a successive correction technique [16]. The conservative Chimera body fitted meshing technique based on geometrical intersections used in the solver allows to adress complex geometries efficiently and to perform parametric studies [64]. In the present study, the k-ω SST model [53] is used to close RANS equations. The temporal integration for the time-marching procedure is a first order Newton GMRES-QR algorithm. Comparison with measurements are provided in Appendix D.1. The simulations were performed by Grégoire Pont at Airbus. The post treatments are done using Antares [3].

The following convention is used for the presentation of spectra. The experimental data is plotted in grey and the predicted spectra in black. The isolated configuration is represented with dashed lines and the installed one with full lines.

	Measurements	TAGA
Isolated case	- - -	- - -
Installed case	——	——

Table 4.3: Convention used for the plots presented in this section.

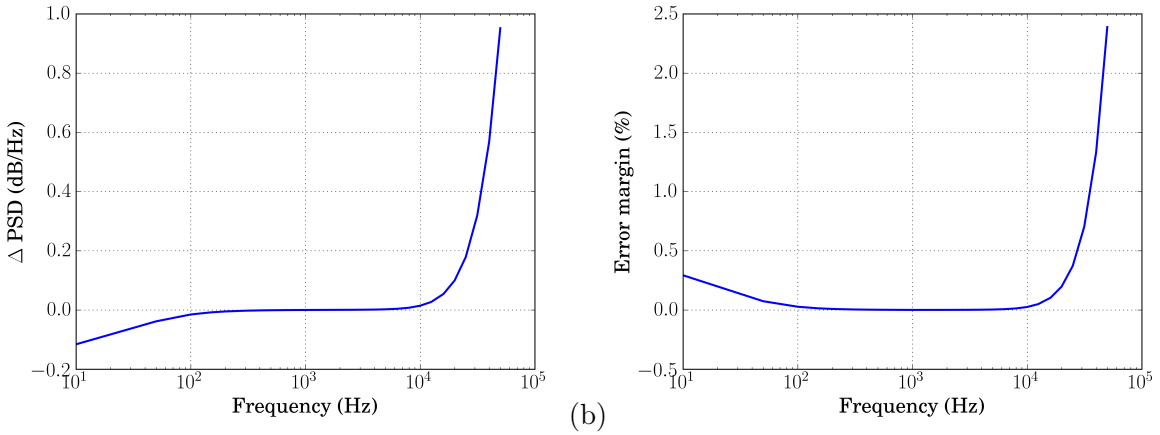

Figure 4.10: Difference between the PSD using Acti-HF and using the analytical solution. (a) Absolute error (b) Error margin.

A validation of the refinement of the mesh has been carried out with the comparison of results given by geometrical acoustics to the analytical solution of the propagation in free field. Although the quality of the mesh has no impact on the computation of $\hat{G}$ with Acti-HF, it plays a role in the obtention of P_S through the numerical derivation. As done in Section 4.1, the medium jet is set equal to the external medium. The difference in dB is plotted in Fig 4.10 (a) and the

equivalent error margin is plotted in Fig 4.10 (b). The agreement between the two predicted noise levels is very good between 100 Hz and 10 kHz, and acceptable up to 50 kHz. In terms of Strouhal number, it corresponds respectively to $St = 0.016$, $St = 1.6$ and $St = 8$. There are some discrepancies outside of this range.

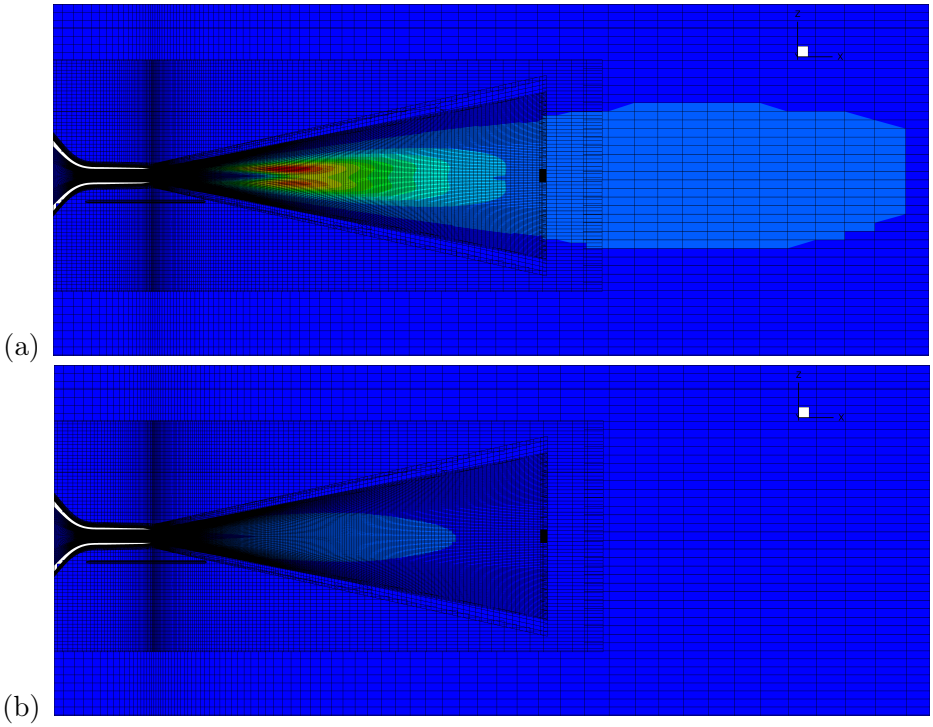

Figure 4.11: Source domain at (a) 50 Hz and (b) 5 kHz on the CFD mesh.

The differences at high frequencies are caused by the mesh, not fine enough for the given frequency range. The mesh is pictured alongside the source domain in Fig 4.11 for (a) 50 Hz ($St = 0.08$) and (b) 5 kHz ($St = 0.8$). The mesh is coarser downstream but only the lowest frequencies are impacted because their corresponding source domains are located downstream enough to be in this unrefined area. Overall, the resulting error is negligible, less than 2.5% and for frequency bands outside of the range of interest, see Fig 4.9.

In Sections 3.2 and 3.3 were introduced the far-field and compactness approximations. Eq (3.37) states that for two points far from each other, the autocorrelation is null. The associated correlation length scale is estimated. The model function in Eq (3.37) is simplified keeping only the axial distance between the two source points. This function is referred as E and is expressed as,

$$E = \exp\left(-\frac{\ln 2}{l_s^2}(\xi_x - \zeta_x)^2\right) \tag{4.1}$$

E takes the form of a Gaussian function with a standard deviation $\sigma = l_s/\sqrt{\ln 2}$. With such functions, there is $E(3\,\sigma) \simeq 0.01$. If $\xi_x - \zeta_x > 3\,\sigma$ it can be considered that E is small enough to be approached by zero, meaning that the correlation is null. The criterion $L = 3\,\sigma = 3l_s/\sqrt{\ln 2}$

is therefore introduced to evaluate the distance for which two source points are uncorrelated.

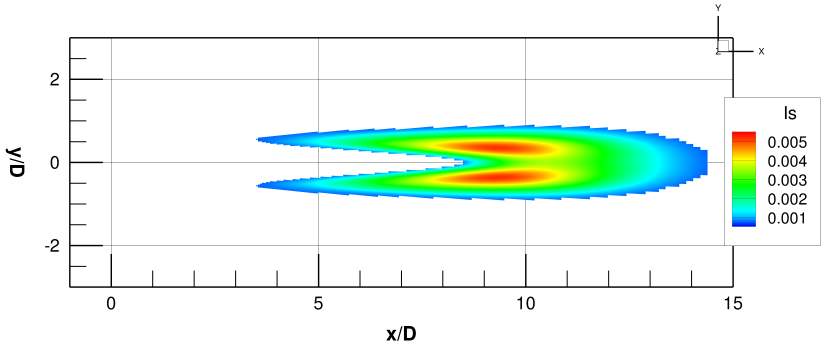

Figure 4.12: Representation of the source amplitude I_s of Eq (3.38) in the source domain for 2kHz.

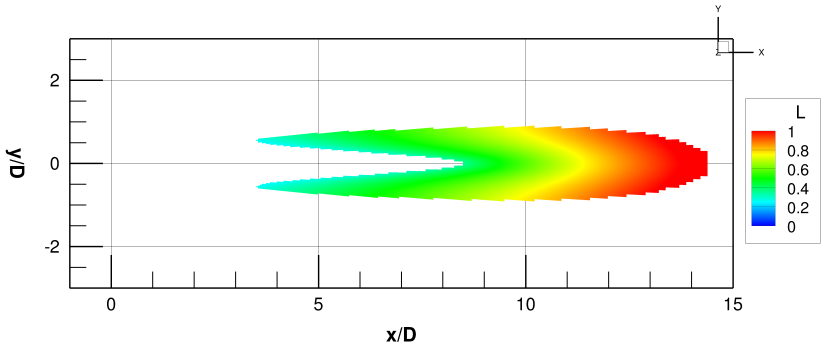

Figure 4.13: Representation of the length scale L, normalised by the nozzle diameter D in the source domain for 2 kHz.

The length scale L is plotted in Fig 4.13 for the peak frequency. The distance of correlation is always less than one diameter overall and is of the order of $0.5\,D$ at the maximum of I_s, at $x \simeq 9\,D$. As a reminder of the different characteristic lengths in this study, the observer is located at $14.2\,D$, the flat plate has a span of $15\,D$ and a chord of $9\,D$ and the wavelength at 2kHz is $\lambda \sim 3.5\,D$. The same study is done at 200 Hz and 20 kHz, respectively frequencies before and after the peak. The results are shown in Table 4.4. Over the whole spectrum, L is inferior or greatly inferior to the different length scales governing the studied configuration. The far-field and compactness approximations are therefore validated.

	200 Hz	2 kHz	20 kHz
λ	$35\,D$	$3.5\,D$	$0.35\,D$
L	$1\,D$	$0.5\,D$	$0.05\,D$

Table 4.4: Estimate of the wavelength λ and the scale length L normalised by the jet nozzle diameter.

4.2.1.3 Normalisation of the predictions

Fig 4.14 (a) shows the OASPL level of the measurements and the predictions. Although the relative difference between the isolated and installed configurations seems right, the absolute levels do not match. Since there is a good agreement between the computed turbulent kinetic energy and experimental data, see comparisons in Appendix D.1, this difference is likely due to the erroneous computation of the scaling parameters in Eq (3.39). A fit of the constants A, c_l and c_τ could fix this discrepancy. Instead, a constant noise level correction based on the OASPL in the isolated configuration is introduced,

$$\Delta_{\mathrm{OASPL}} = \overline{\mathrm{OASPL}}_{\mathrm{iso,exp}} - \overline{\mathrm{OASPL}}_{\mathrm{iso,TAGA}} \tag{4.2}$$

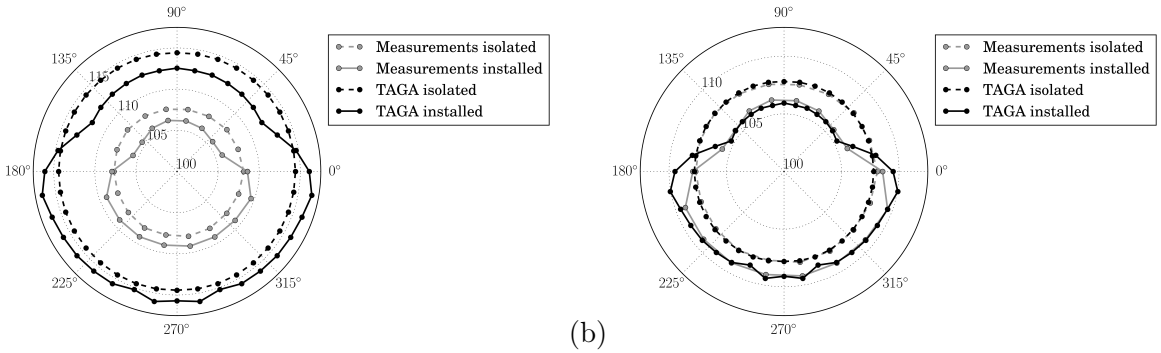

Figure 4.14: OASPL (a) before and (b) after application of a corrective delta for an azimuthal array located at the polar angle $\theta = 90°$.

where the bar denotes here the azimuthal mean value.

Here, $\Delta_{\mathrm{OASPL}} \simeq 6\,\mathrm{dB}$. The same delta, still using the isolated configuations is applied on the installed predictions. The OASPL predictions after the application of the emipirical correction Eq (4.2) are shown in Fig 4.14 (b). With this correction, the installed predictions are now of the same order as the experimental data.

4.2.2 Installation effects

The accuracy of the predictions for installation effects is examined in this subsection. A study on the full azimuth range is done at the Mach number $M = 0.9$. Three axial positions are considered $\theta = 90°$, $\theta = 100°$ and $\theta = 110°$. As shown in Fig 4.15, the measurements more downstream cannot be used because driven by large scale turbulence and there are no measurements from the upstream arc. The plate is far from jet flow, so it can be considered that the source domain is equal for both configurations and only the propagation causes differences between the two cases. In the isolated configuration, the only contribution used is T (Transmission). In the installed configuration T (Transmission), T*R (Transmission then Reflection) and T*D (Transmission then Diffraction) are used, so that the rays that reflect on the flat plate and that are diffracted on the edges of the plate are also taken into account.

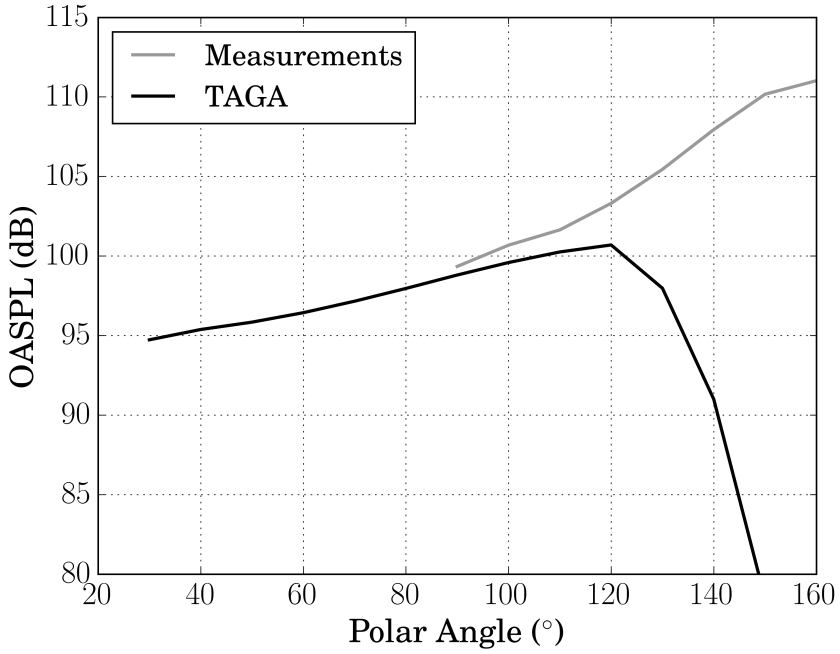

Figure 4.15: Polar evolution of the measured and predicted OASPL in the isolated configuration.

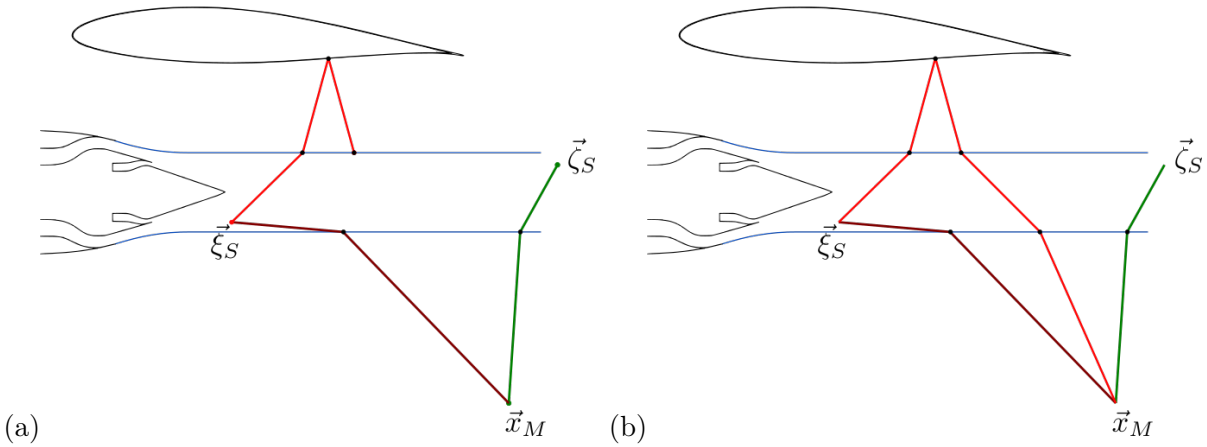

Figure 4.16: Illustration of (a) the jet blockage configuration and (b) its resolution.

A phenomenon of jet blockage appears for observers at an azimuthal angle between 260 and 280 degrees. The three contributions used do not allow the passage of rays through the jet after reflecting on the flat plate. This is illustrated in Fig 4.16 (a). This is not an issue for the other observers. To prevent erroneous predictions, the additional contribution T*R*T*T (a Transmission followed by a Reflection and two Transmissions) is also used at these particular locations. Fig 4.16 (b) shows the updated situation. The increased computation time does not constitute a problem given the few azimuthal angles concerned and the possibility to parallelise the ray tracing calculations.

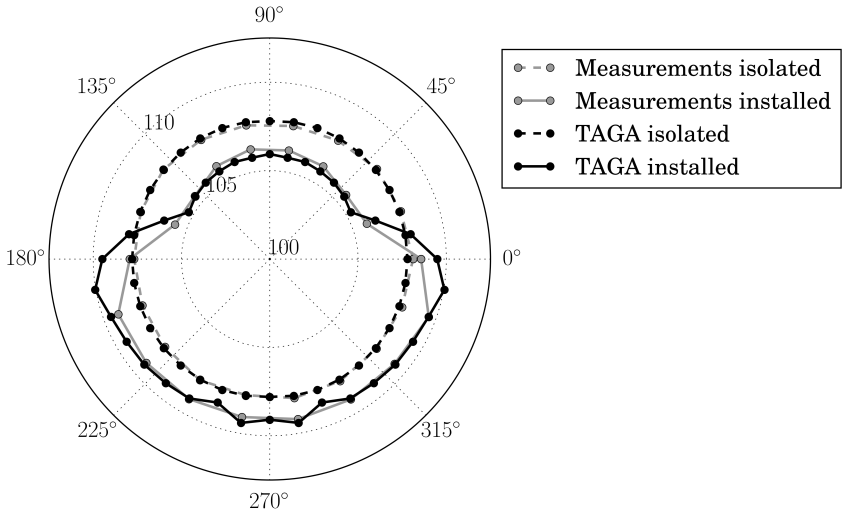

Figure 4.17: OASPL prediction at $\theta = 90°$.

4.2.2.1 Noise predictions at $M = 0.9$ and $\theta = 90°$

One specific case will be commented, namely for the azimuthal microphone array of radius 14.2 D at $\theta = 90°$ for a jet Mach number of 0.9. Fig 4.17 shows the comparison for the OASPL between the measurements and the prediction by TAGA corrected with the delta from Eq (4.2). The flat plate is located at $\phi = 90°$. The azimuthal array can be decomposed into four areas. Table 4.5 shows these areas with the contributions reaching the observers. As a reminder, T stands for a transmission, R a reflection and D a diffraction. Fig 4.17 shows that in terms of OASPL, there is a good agreement for all zones. The zone around the flat plate sides shows an over prediction that could be linked to the diffraction. The OASPL is however a metric that integrates the noise level over the whole frequency range. The Power Spectral Density PSD is considered for more in depth analysis. The predictions are symmetric with respect to the $90° - 270°$ axis, therefore only half the predictions are shown. One point of comparison is presented for each area. The full results are provided in Appendix D.2. The spectra are plotted following the convention provided in Table 4.3. It is reminded that the PSD spectra for both configurations are also scaled using the correction presented in Eq (4.2). This fit only uses the experimental data from the isolated case despite being applied on the installed predictions.

Areas	Angles	Contributions
Above the plate	$[20°; 160°]$	T, T*D
Around the plate sides	$[160°; 200°] \cup [340°; 20°]$	T, T*D, T*R if possible
Under the plate - Sideline	$[200°; 240°] \cup [300°; 340°]$	T, T*R
Under the jet - Cutback	$[240°; 300°]$	T, T*R*T*T

Table 4.5: The four different zones in the azimuthal range.

The isolated predictions are axisymmetric but they are still shown as a reference next to the installed predictions. When corrected with Eq (4.2), there is a good agreement over the whole

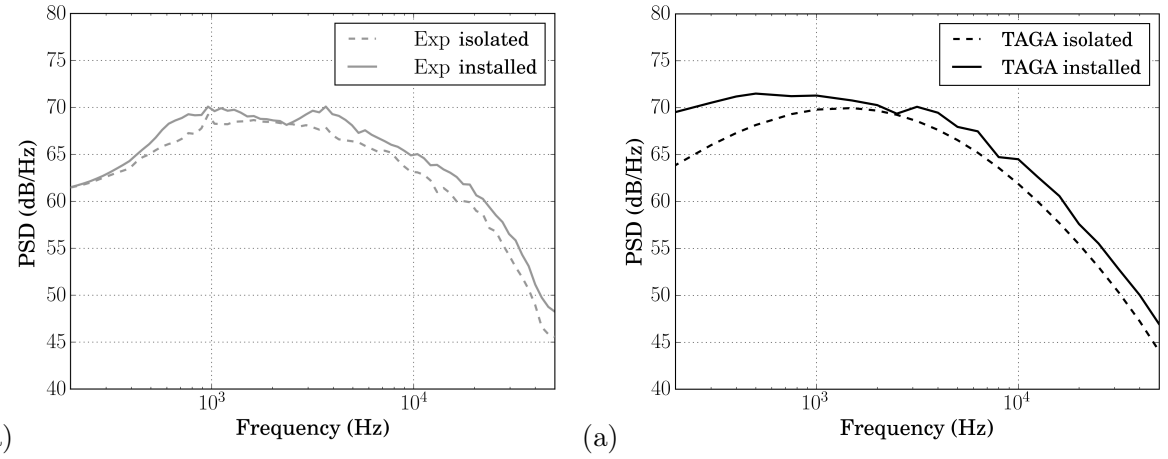

Figure 4.18: PSD for an observer at a polar angle of $\theta = 90°$ and $\phi = 340°$ for (a) the measurements and (b) the predictions.

frequency range with a maximum of 3 dB between the predictions and the measurements. Fig 4.19 shows the isolated predictions by TAGA against the measurements at $\theta = 90°$ and $\phi = 280°$. Overall there is a good agreement after normalisation. The peak frequency is slightly under estimated, the lower frequencies are over predicted while the higher frequencies are a bit under predicted.

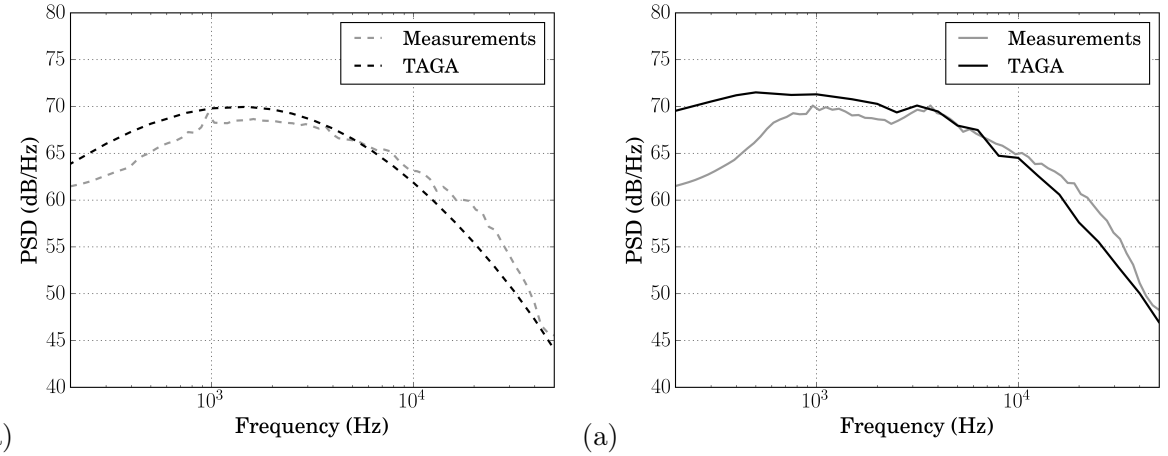

Figure 4.19: PSD for an observer at a polar angle of $\theta = 90°$ and $\phi = 340°$ in (a) the isolated case and (b) the installed case.

Fig 4.18 shows the noise measurements (a) and predictions (b) for an observer under the flat plate, at $\phi = 340°$. Experimentally, it can be seen that the installation effects cause a local decrease in PSD between 2 kHz and 3 kHz followed by a sharp increase around 4 kHz and above. The presence of this secondary peak is explained by an interference phenomenon. Section 4.2.2.3 shows an in-depth analysis of this phenomenon. The TAGA model predicts accurately the local decrease as well as the increase at 4 kHz. The increase is however slightly less pronounced as in the experimental data. The noise level at the peak is also well caught but there is an over estimation under 1 kHz. Investigations showed that this discrepancy is also linked with the interference

phenomenon. This is also discussed in more details in Section 4.2.2.3.

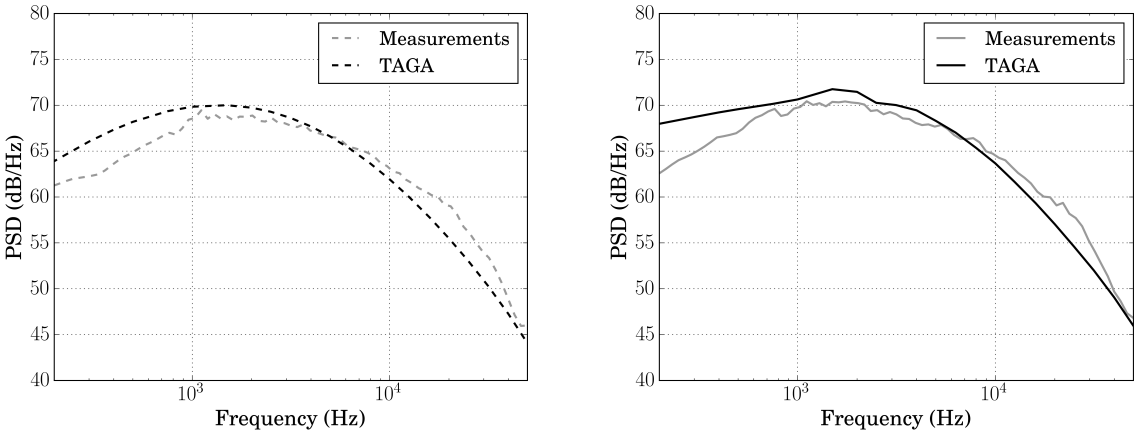

Figure 4.20: PSD for an observer at a polar angle of $\theta = 90°$ and $\phi = 280°$ in (a) the isolated case and (b) the installed case.

The noise predictions for an observer under the jet at $\phi = 280°$ are given in Fig 4.20. The agreement at this position, corresponding to the cutback certification point, is good for frequencies above 1 kHz. TAGA predicts a noise spectrum that matches the experimental data in terms of peak frequency and amplitude. A similar over prediction at lower frequency is however observed. An over prediction of the interference phenomenon between the T and T*R*T*T rays could explain this difference. The shape of the spectrum at high frequencies shows the same weaknesses as in the isolated case but remains a good fit.

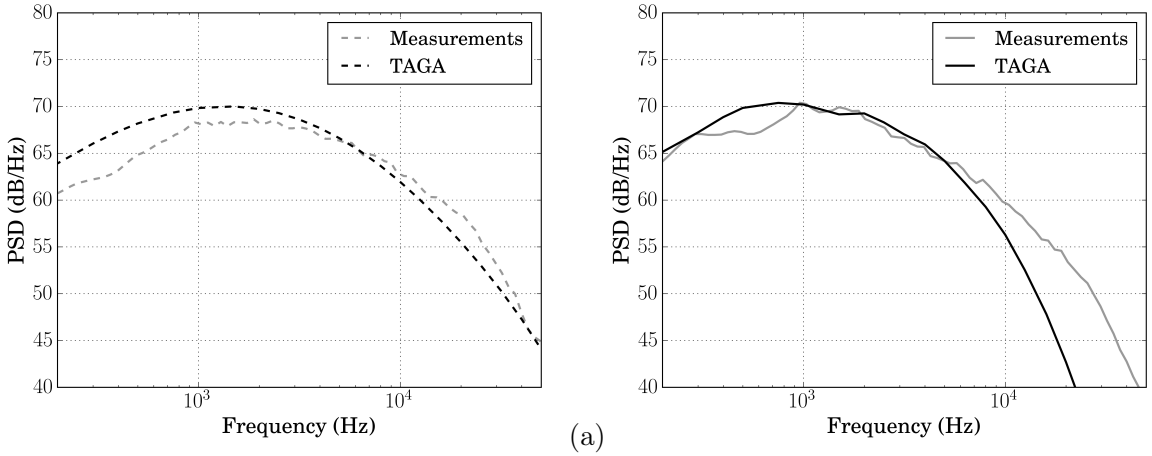

Figure 4.21: PSD for an observer at a polar angle of $\theta = 90°$ and $\phi = 80°$ in (a) the isolated case and (b) the installed case.

The comparison between the noise predictions and the measurements for an observer above the plate at $\phi = 80°$ is shown in Fig 4.21. The introduction of the flat plate leads to a decrease of around 5 dB at 2 kHz and above. This is explained by a shielding by the plate of the sound waves coming from the part of the flow directly after the nozzle. Indeed, this part of the jet plume is known to contain sources contributing to the high frequencies. A sharper decrease of around 10 dB

is predicted by TAGA. This gap between the prediction and the measurements hints at a missing contribution or an erroneous computation of the energy brought by diffracted rays. Under 2 kHz the noise is increased in the measurements but not in the predictions. The predictions match the measurements at low frequencies but it is believed to be a false positive. This increase is explained by an interaction between the plate and the hydrodynamic pressure field around the jet. These fluctuations diffract on the plate edges and propagate a low frequency noise [50] that is not taken into account in the present model. The peak amplitude is well predicted by TAGA when corrected.

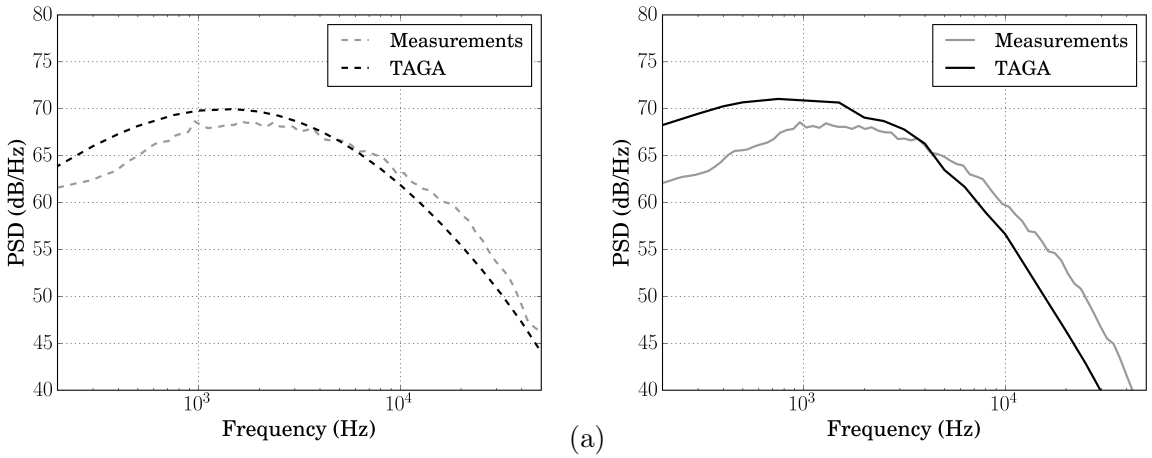

Figure 4.22: PSD for an observer at a polar angle of $\theta = 90°$ and $\phi = 20°$ in (a) the isolated case and (b) the installed case.

Fig 4.22 shows the PSD for an observer slightly above the flat plate. The predicted shielding is over estimated even with the addition of the diffraction on the edges. It is believed that the lower frequency behaviour is analog to what was shown under the plate with an interference between the refracted rays and the diffracted rays. This over prediction at 1 kHz and under leads to an over estimation of the peak amplitude by 2-3 dB.

A study on the full azimuth range at an axial plan located at the nozzle exit was presented. The prediction of installation effects by TAGA was compared with measurements on cold single jet. For observers under the plate, a good agreement is seen for frequencies above 1 kHz. The noise is over predicted for frequencies under this value. Measurements showed a secondary peak for observers at these locations. The noise prediction model catches well the frequency and the amplitude of this secondary peak. The agreement above the flat plate is less satisfactory with stronger discrepancies outside of the hump of the spectrum. Indeed, the shielding is over predicted above 8 kHz, especially well above the plate. At these positions, the increase under 1 kHz, is not predicted because outside of the scope of the model. The predictions between $\phi = 20°$ and $\phi = 160°$ are however less important because not linked to the certification process, see Section 1.1.

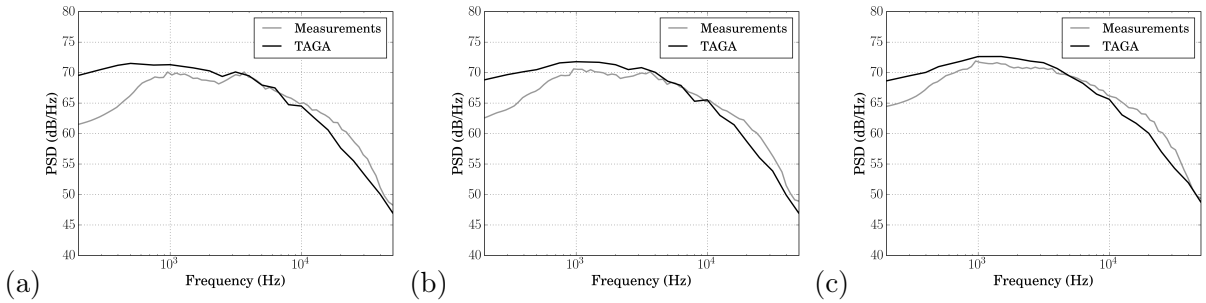

Figure 4.23: Comparison of the PSD in the installed configuration at $M = 0.9$ for an observer at $\phi = 340°$ and (a) $\theta = 90°$, (b) $\theta = 100°$, and (c) $\theta = 110°$.

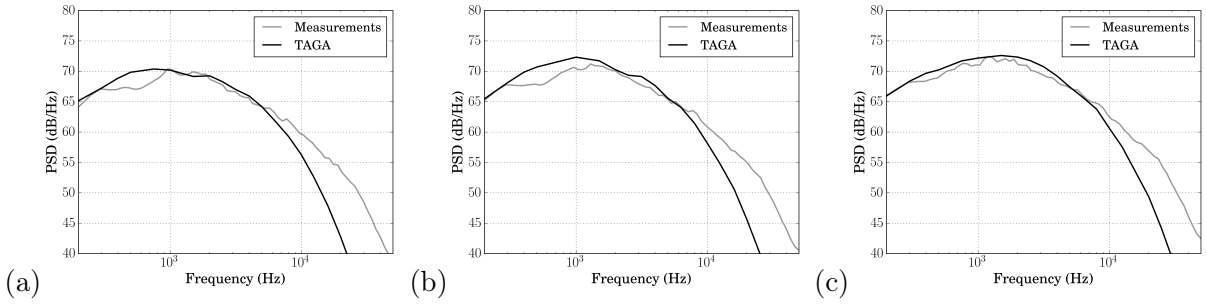

Figure 4.24: Comparison of the PSD in the installed configuration at $M = 0.9$ for an observer at $\phi = 80°$ and (a) $\theta = 90°$, (b) $\theta = 100°$, and (c) $\theta = 110°$.

4.2.2.2 Complementary results

The previous subsection went into details for a jet at $M = 0.9$ and microphones in the axial plan located at the nozzle exit. As mentioned above, more results were obtained during this thesis. The full results are provided in Appendix D.2 but an extract of these results is commented here. TAGA was also tested at axial positions more downstream than $\theta = 90°$, namely $\theta = 100°$ and $\theta = 110°$. Fig 4.23 shows the comparison between TAGA and the measurements at these three polar angles for an observer under the plate while 4.24 shows the comparisons for an observer over the flat plate. For the first category of observers, there is a good agreement for all frequencies over 1 kHz. The differences between the TAGA predictions and the experimental data are of a similar extent for the three polar positions. The secondary peak is also well caught at $\theta = 100°$ and does not appear in either the measurements or the predictions at $\theta = 110°$. With the second category of observers, the peak frequency and amplitude is well caught while the shielding effects is over estimated. Just like the observers under the plate, the differences between the TAGA predictions and the experimental data are of a similar extent for the three polar positions. The conclusions drawn in the previous subsection can therefore be generalised to the two other axial plans.

4.2.2.3 Investigation of the secondary peak in the installed case

At certain azimuthal positions, the presence of a secondary peak can be observed in both the experimental data and the noise predictions. An example is shown in Fig 4.25 for an observer

located slightly under the flat plate, at 340° and at a polar angle of 90°. Whatever the cause of this secondary peak is, it is accurately predicted by the present model. Fig 4.26 shows the PSD for three observers located at a polar angle $\theta = 90°$ and azimuthal angles of $\phi = 330°$; $\phi = 340°$; $\phi = 350°$ with a line at 3150 Hz. This highlights the importance of the position of the observer on the peak frequency. The objective of this subsection is to offer an explanation for this phenomenon through two studies. The first study aims at showing what happens at $\phi = 340°$; $\phi = 350°$, but not at $\phi = 330°$, at a frequency of 3150 Hz. The second one shows what happens at $\phi = 350°$, at 4 kHz and above.

For these predictions, the length scales in the three directions are set equals $l_x = l_y = l_z = l_s$. Under this assumption, Eq (3.87) can be reduced to a form independent of the azimuth ϕ.

$$A_S(\vec{x}_M, \vec{\zeta}_S, \omega) \propto \frac{I_s^2 l_x l_y l_z}{\tau_s} \frac{\exp\left[-\dfrac{\omega^2}{4\ln 2\bar{u}_x^2}\left(l_x^2 + \dfrac{\bar{u}_x^2}{c_{ext}^2}[l_y^2 \sin^2\theta\cos^2\phi + l_z^2 \sin^2\theta \sin^2\phi]\right)\right]}{1 + \left(1 - \dfrac{\bar{u}_x}{c_{ext}}\cos\theta\right)^2 \omega^2\tau_s^2} \tag{4.3}$$

$$A_S(\vec{x}_M, \vec{\zeta}_S, \omega) \propto \frac{I_s^2 l_s^3}{\tau_s} \frac{\exp\left[-\dfrac{\omega^2 l_s^2}{4\ln 2\bar{u}_x^2}\left(1 + \dfrac{\bar{u}_x^2}{c_{ext}^2}\sin^2\theta\right)\right]}{1 + \left(1 - \dfrac{\bar{u}_x}{c_{ext}}\cos\theta\right)^2 \omega^2\tau_s^2} \tag{4.4}$$

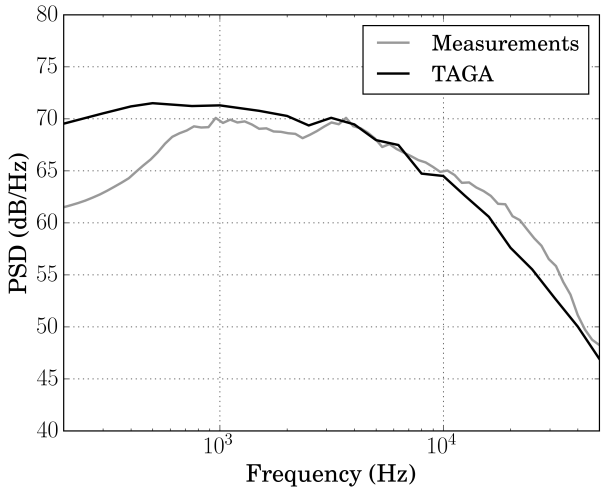

Figure 4.25: Noise prediction at $\theta = 90°$ and $\phi = 340°$.

The source term A_S is not a function of the azimuth ϕ, meaning that A_S is constant for all three observer positions considered in this study, leaving only the propagation term P_S as cause of this phenomenon. This propagation term is pictured in Fig 4.27, 4.28 and 4.29, respectively for

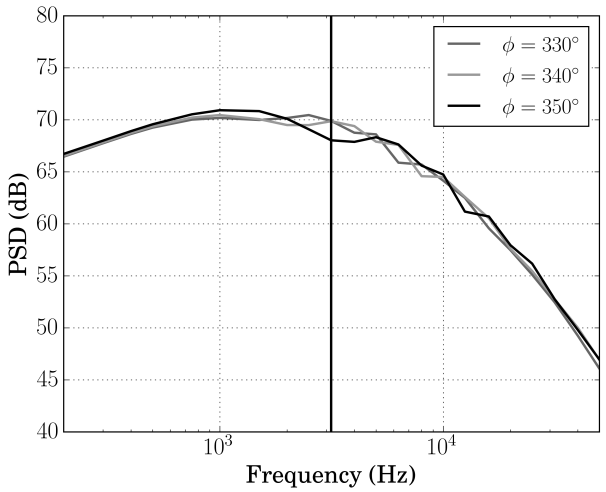

Figure 4.26: Noise prediction at $\theta = 90°$ and $\phi = 330°$; $\phi = 340°$; $\phi = 350°$.

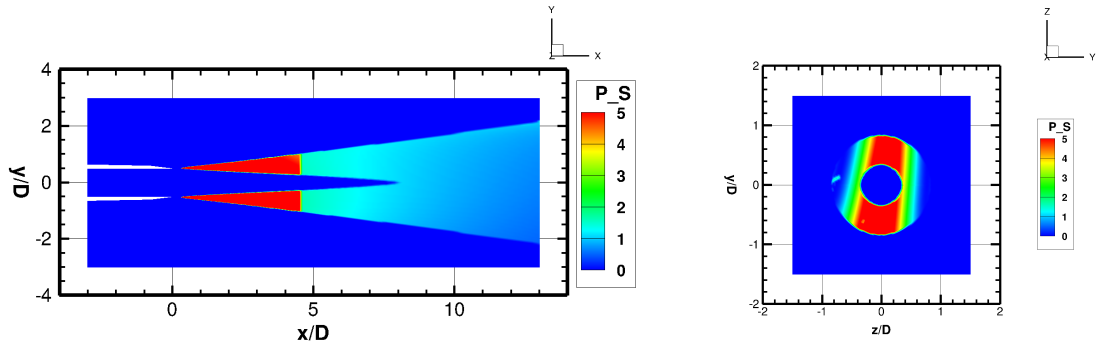

Figure 4.27: Propagation term P_S in the jet plume at (a) $z/D = 0$ and (b) $x/D = 3$ for an observer at $\theta = 90°$ and $\phi = 330°$ for $f = 3150\,\text{Hz}$.

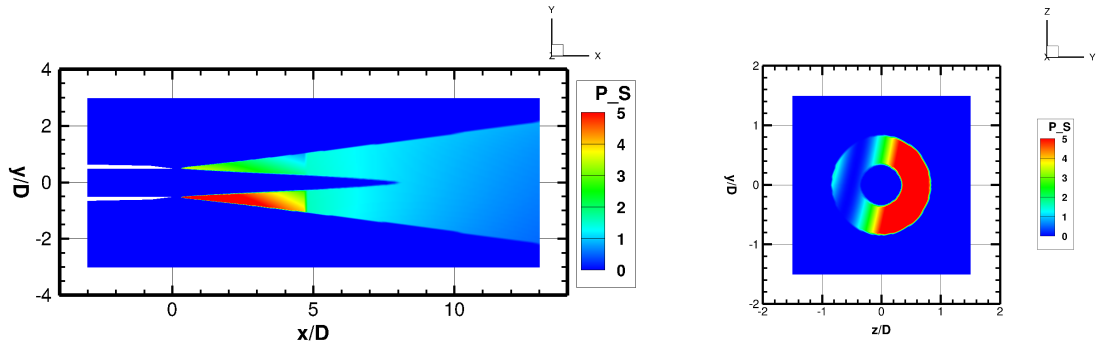

Figure 4.28: Propagation term P_S in the jet plume at (a) $z/D = 0$ and (b) $x/D = 3$ for an observer at $\theta = 90°$ and $\phi = 340°$ for $f = 3150\,\text{Hz}$.

observers at $\phi = 330°$, $\phi = 340°$ and $\phi = 350°$. Fig 4.30 shows I_s at $f = 3150\,\text{Hz}$. Two separate domains can be seen for the axial representations. The domain that is further from the jet nozzle represents the points where only one ray can link the source and the observer: a refracted one. The second domain, closer to the jet nozzle and actually under the plate, represents the points

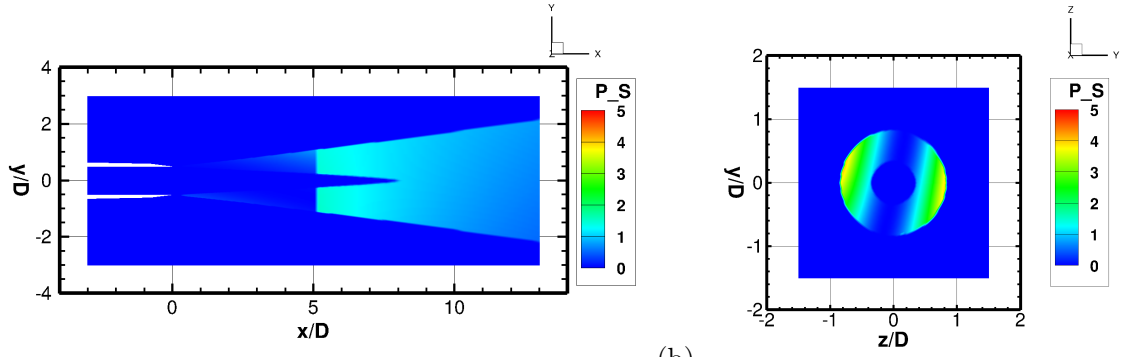

(a) (b)

Figure 4.29: Propagation term P_S in the jet plume at (a) $z/D = 0$ and (b) $x/D = 3$ for an observer at $\theta = 90°$ and $\phi = 350°$ for $f = 3150\,\text{Hz}$.

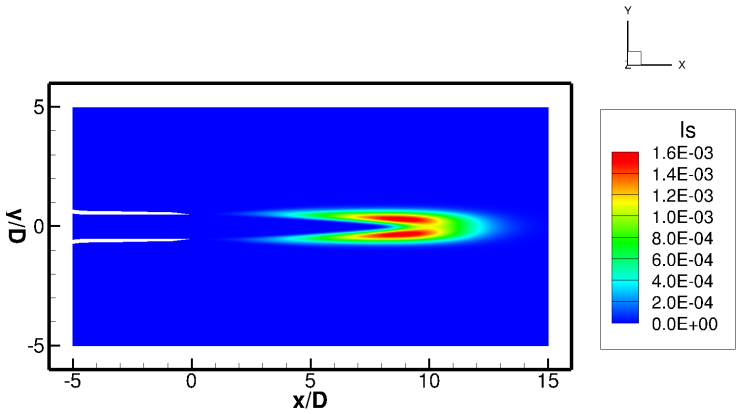

Figure 4.30: I_s for an observer at $\theta = 90°$ at $f = 3150\,\text{Hz}$.

where two rays can link the source and the observer: a refracted one and a refracted then reflected one. There is a discontinuity between the two domains because in these simulations the diffracted rays are not included. The fact that two rays coming from the same source coexist creates a 3D interference pattern. This is especially visible in the cross sections. The interference phenomenon is linked to the phase difference between the two rays which itself is a function of the difference of ray path between the two interfering rays as well as the frequency. Because the observers are relatively close to each other, from Fig 4.27 to Fig 4.29 it is possible to see the fringe move down in pictures (a) and right in pictures (b). In this case, the fringe spacing is of the same order of the jet radius meaning that for a given observer, a destructive fringe can occupy the jet plume like in Fig 4.29 for $\phi = 350°$ leading to a deficit in energy. Similarly, a constructive fringe can occupy the domain like in Fig 4.27 and 4.28 for respectively $\phi = 330°$ and $\phi = 340°$ and thus lead to an increase in energy. It is also interesting to point out that compared to the case where only one refracted ray is possible, a constructive fringe involves a much larger increase of P_S than the loss induced by a destructive fringe.

Let us now fix $\phi = 350°$ and vary the frequency f. Fig 4.31 to Fig 4.35 show the propagation term P_S for f from 2500 Hz to 6300 Hz. Here again the passage of the fringes can be clearly

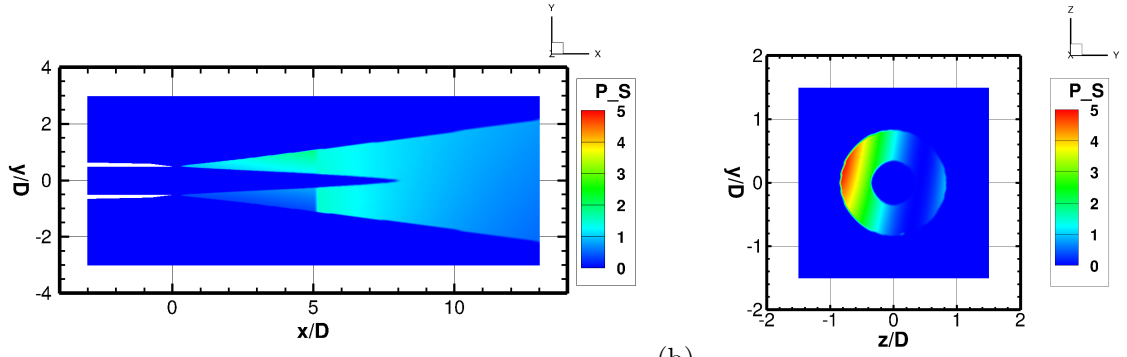

(a) (b)

Figure 4.31: Propagation term P_S in the jet plume at (a) $z/D = 0$ and (b) $x/D = 3$ for an observer at $\theta = 90°$ and $\phi = 350°$ for $f = 2500\,\text{Hz}$.

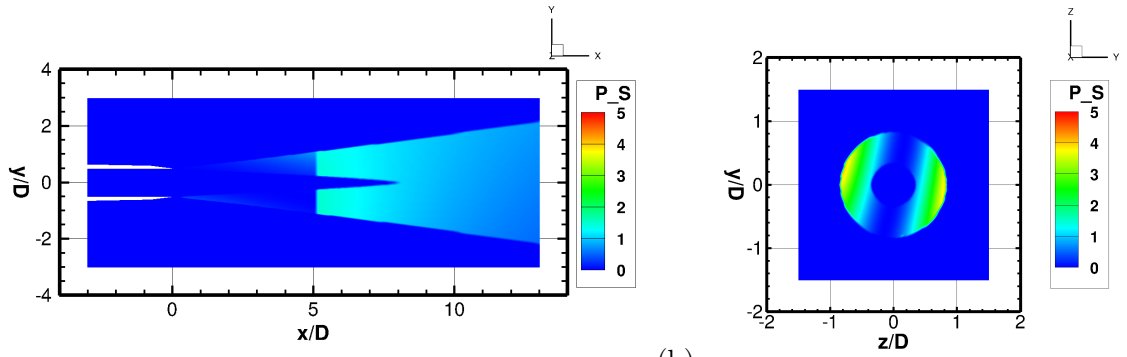

(a) (b)

Figure 4.32: Propagation term P_S in the jet plume at (a) $z/D = 0$ and (b) $x/D = 3$ for an observer at $\theta = 90°$ and $\phi = 350°$ for $f = 3150\,\text{Hz}$.

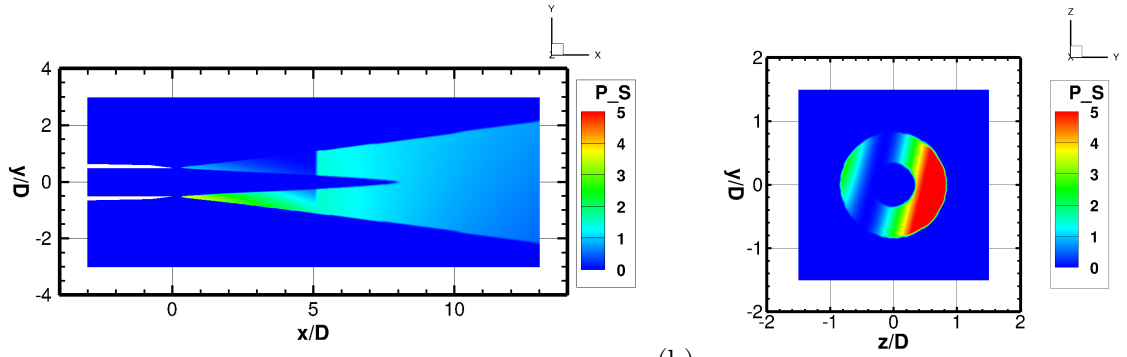

(a) (b)

Figure 4.33: Propagation term P_S in the jet plume at (a) $z/D = 0$ and (b) $x/D = 3$ for an observer at $\theta = 90°$ and $\phi = 350°$ for $f = 4000\,\text{Hz}$.

seen when the frequency evolves. The start of the increase in noise level at $f = 4000\,\text{Hz}$ is easily explained. Indeed, before this value, the zone is dominated by a destructive fringe whereas above 4 kHz a contructive fringe occupies the space.

These comparisons showed the arrival of a constructive fringe with the increase of the frequency but it is fair to assume that this passage of constructive and destructive fringes is a periodic phenomenon that would lead to several peaks instead of just one secondary peak. In

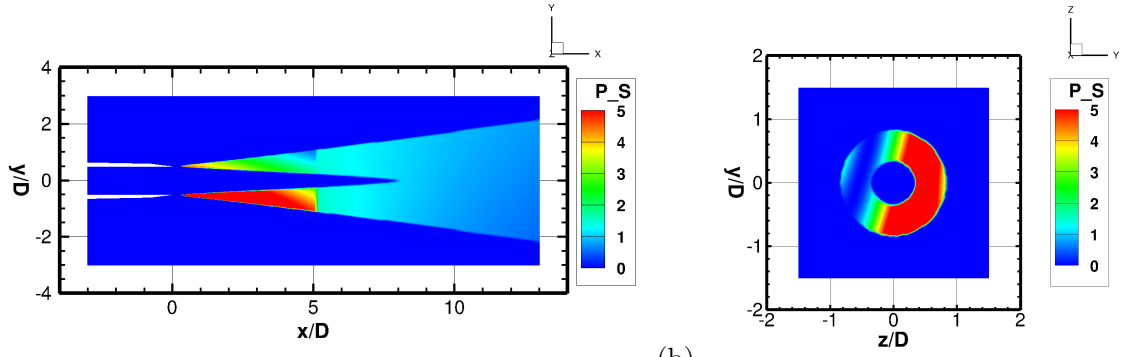

(a) (b)

Figure 4.34: Propagation term P_S in the jet plume at (a) $z/D = 0$ and (b) $x/D = 3$ for an observer at $\theta = 90°$ and $\phi = 350°$ for $f = 5000\,\text{Hz}$.

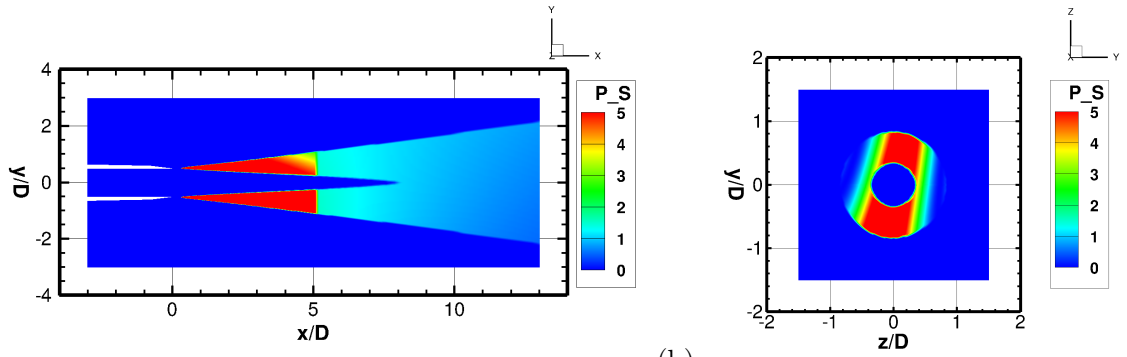

(a) (b)

Figure 4.35: Propagation term P_S in the jet plume at (a) $z/D = 0$ and (b) $x/D = 3$ for an observer at $\theta = 90°$ and $\phi = 350°$ for $f = 6300\,\text{Hz}$.

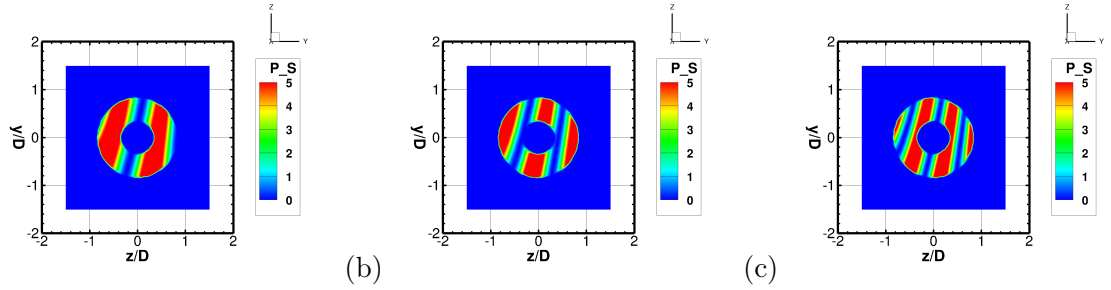

(a) (b) (c)

Figure 4.36: Propagation term P_S in the jet plume at $x/D = 3$ for an observer at $\theta = 90°$ and $\phi = 350°$ for (a) $f = 10000\,\text{Hz}$, (b) $f = 12500\,\text{Hz}$ and (c) $f = 16000\,\text{Hz}$.

reality, the extent of this interference phenomenon is linked to the relative size of the jet plume and the width of the interference fringes. The fringes get thinner with increased frequency, as depicted in Fig 4.36, thus reducing the predominance of either a constructive or destructive interference. The zone under the plate is therefore more homogeneous in terms of P_S and that translates to an increase of PSD that tends to a limit value. The fringe pattern still varies with the frequency which explains the oscillations after the peak, see Fig 4.25. It can be expected that if the frequency discretisation in the spectrum was higher and the plot done in a non-logarithmic scale, these oscillations would be clearer.

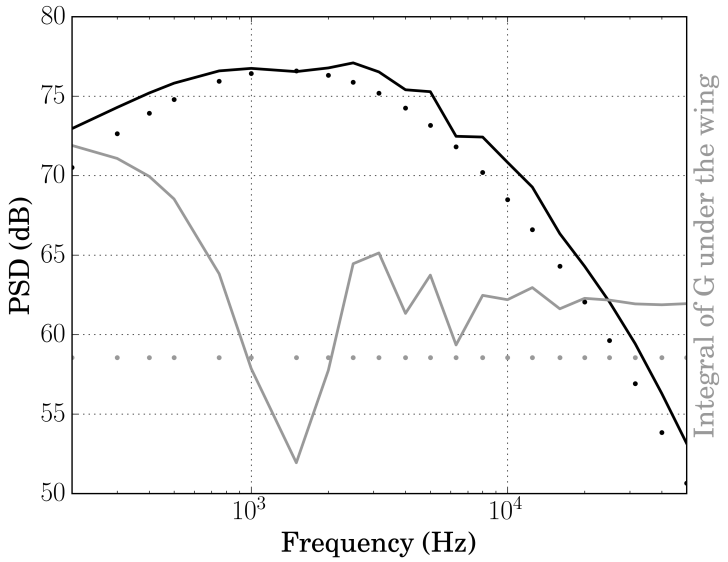

Figure 4.37: Noise prediction (black) compared with the sum of the propagation term under the flat plate (grey) at $\theta = 90°$ and $\phi = 330°$. The full line is the installed case and in dotted line is the isolated case.

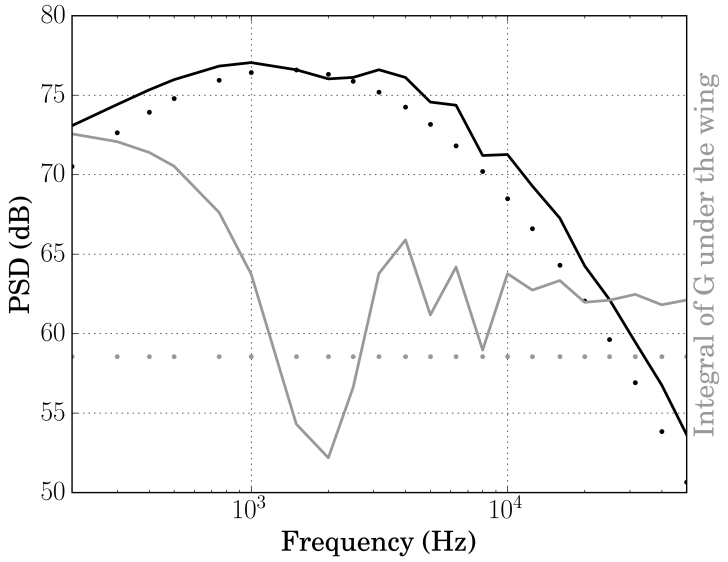

Figure 4.38: Noise prediction (black) compared with the sum of the propagation term under the flat plate (grey) at $\theta = 90°$ and $\phi = 340°$. The full line is the installed case and in dotted line is the isolated case.

To conclude this investigation, both the noise level and the propagation term for the domain under the flat plate are plotted against the frequency in Fig 4.37, 4.38 and 4.39. Plotting the integrated value of the propagation term is equivalent to plotting the power spectral density in the case of $A_S = 1$. The passage of the fringes is quite clear with this representation. There is a good agreement between the increase of the noise level and the nature of the fringes present. The shift of the fringes when the observer is moved is also clear. The limit value of the increase with the reduction of the fringe width is well displayed above 10 kHz. The over predictions observed

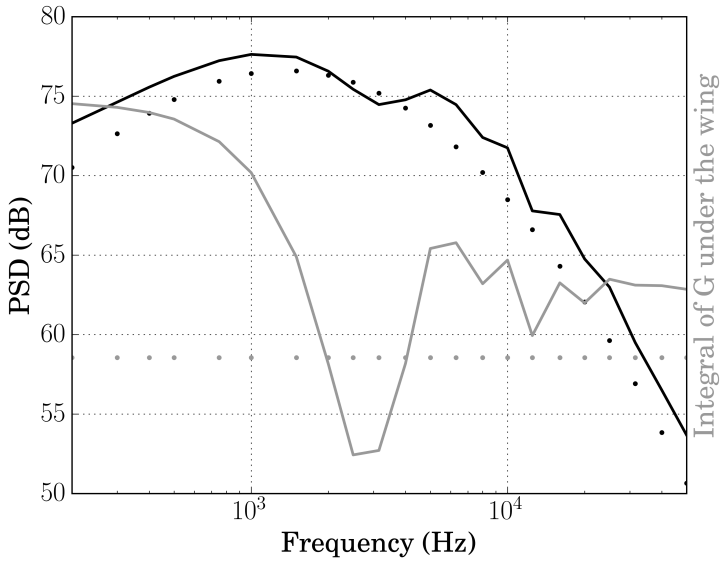

Figure 4.39: Noise prediction (black) compared with the sum of the propagation term under the flat plate (grey) at $\theta = 90°$ and $\phi = 350°$. The full line is the installed case and in dotted line is the isolated case.

at low frequencies in the previous subsection can also be explained. Indeed, a first constructive fringe passes in the zone under the plate at around 200 Hz for all three microphones leading to a sharp increase of the PSD.

4.2.2.4 Use of the model as a scaling tool

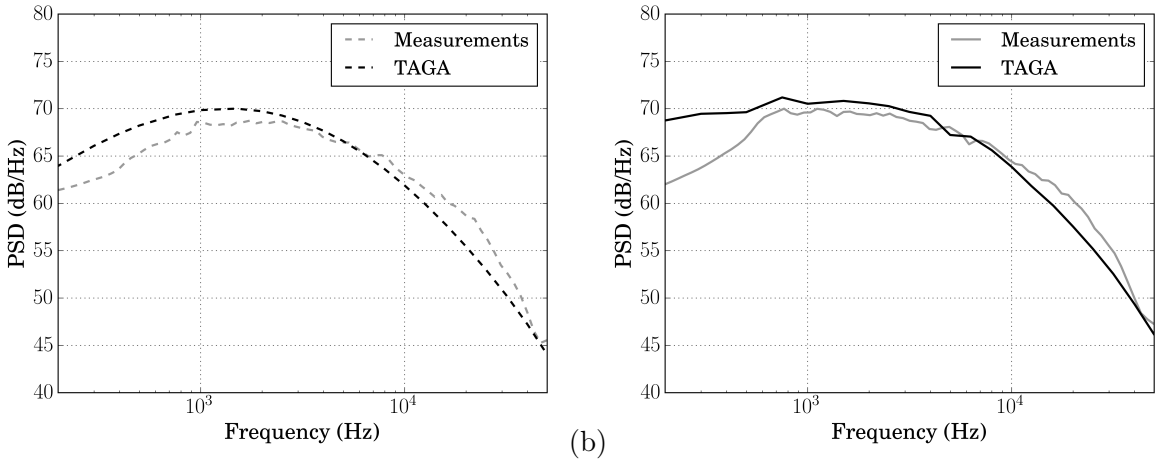

Figure 4.40: Noise prediction at $\theta = 90°$ and $\phi = 320°$ in the (a) isolated case and (b) installed case.

As explained in the literature review, the set of constants governing the traditional calibrating scales are often fitted to the experimental data to improve the results [43][78][55]. This fit can correct the shape of the spectrum as well as its peak frequency. This optimising step can only be done if the experimental measurements are available and in this case, there is little use of

predictions anymore. A new method to improve the predictions is introduced. The results presented in the previous subsections showed that the model developed in this thesis was rather successful but had some key flaws. First, the absolute level is off by several dB leading to the need of a previous correction introduced in Eq (4.2). Next, the shape of the spectrum does not follow the experiment with an over prediction at low frequencies and an under prediction at high frequencies in both the isolated and installed case as shown in Fig 4.40. A parallel can be drawn between the two cases. Indeed, the predictions in both configurations lack accuracy at the same frequency ranges and to the same extent. This means that the evolution of the spectrum with the introduction of the flat plate is well predicted with TAGA. Mathematically, this translates to

$$\mathrm{PSD}_{\mathrm{ins,TAGA}} - \mathrm{PSD}_{\mathrm{iso,TAGA}} \simeq \mathrm{PSD}_{\mathrm{ins,exp}} - \mathrm{PSD}_{\mathrm{iso,exp}} \tag{4.5}$$

with "ins" designing the installed configuration and "iso" the isolated configuration. The scaled noise spectrum for the installed case can therefore be obtained using the noise spectrum of the isolated case and both noise predictions with

$$\mathrm{PSD}_{\mathrm{ins,scaled}} = \left(\mathrm{PSD}_{\mathrm{ins,TAGA}} - \mathrm{PSD}_{\mathrm{iso,TAGA}}\right) + \mathrm{PSD}_{\mathrm{iso,exp}} \tag{4.6}$$

It should be noted that this scaling technique uses the same amount of information as the previous fit done with Eq (4.2). This subsection evaluates the performance of the TAGA model as a scaling tool.

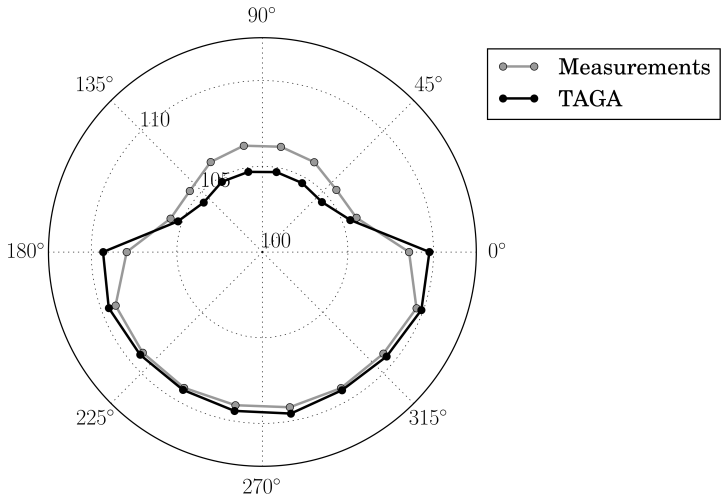

Figure 4.41: Azimuthal evolution of the OASPL for an observer at a polar angle of $\theta = 90°$.

Eq (4.6) is used on the measurements in the isolated case for a Mach number of 0.9. Fig 4.41 shows the OASPL of the measurements in grey and the scaled spectrum in black. As could be expected the pattern resembles the one obtained for the absolute comparisons, see Fig 4.17, with an under prediction of the noise level for observers located above the flat plate, an accurate prediction of the noise level for observers under the plate. Comparing the two OASPL diagrams does not show any improvement. The power spectral density has to be studied for more accurate

comparison between the two corrections.

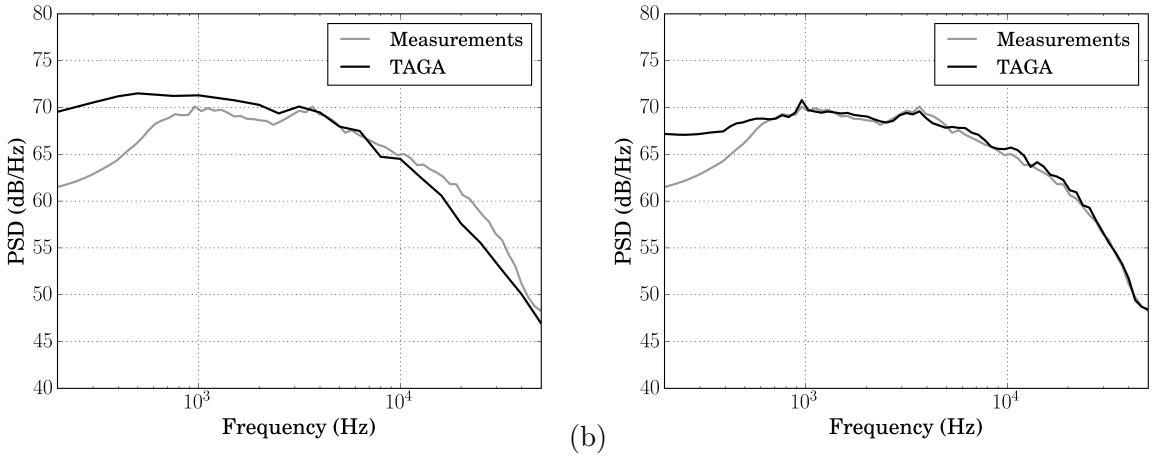

Figure 4.42: PSD for an observer at a polar angle of $\theta = 90°$ and $\phi = 340°$ in the installed case. Predictions using (a) the normalised TAGA results and (b) the scaled TAGA results.

Comparisons for an observer located under the flat plate, at an azimuthal angle of $\phi = 340°$ are shown in Fig 4.42. The use of the measured isolated spectrum as a base provides a better shape for the spectrum and thus increases the frequency range for which the agreement is very good. Just like the normalised predictions, the secondary peak due to the interference phenomenon is well caught in both frequency and amplitude. An over estimation under 1 kHz is seen. A possible explanation could be given by drawing a parallel with the interference patterns. As explained previously, this is due to the presence of a constructive fringe that occurs at the exact frequency range where the over prediction occurs, see Fig 4.38. An incorrect evaluation of this phenomenon coupled with a frequency range outside of the frame of geometrical acoustics could be the cause of this over estimation.

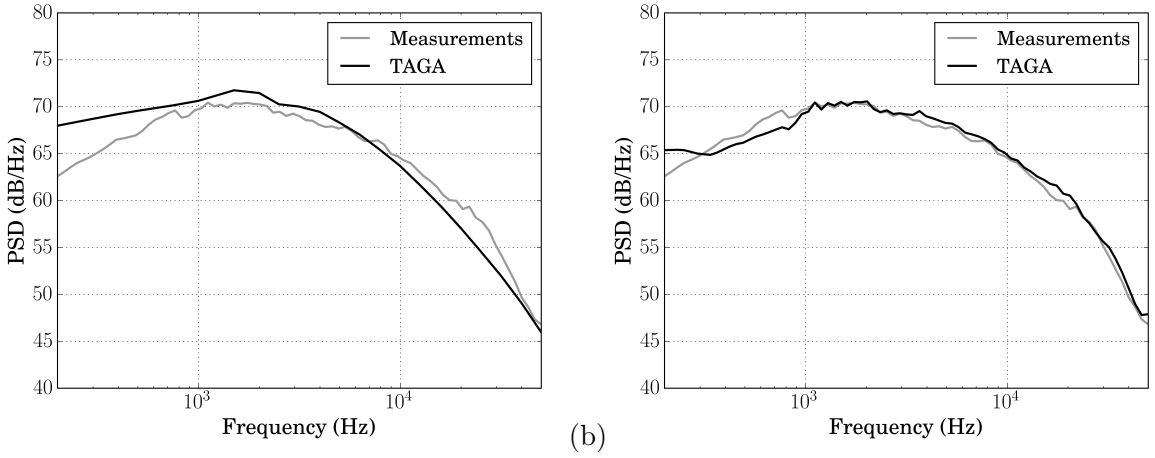

Figure 4.43: PSD for an observer at a polar angle of $\theta = 90°$ and $\phi = 280°$ in the installed case. Predictions using (a) the normalised TAGA results and (b) the scaled TAGA results.

Noise predictions for an observer under the jet at $\phi = 280°$ are pictured in Fig 4.43. The conclusions are the same as for observers located further from the jet. The agreement above

1 kHz is very good with a better prediction of the shape of the spectrum.

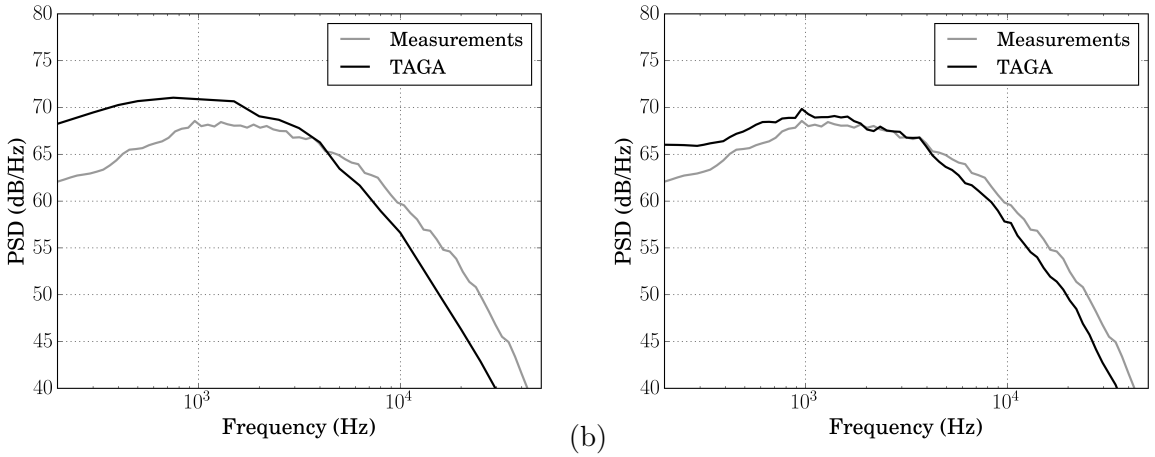

Figure 4.44: PSD for an observer at a polar angle of $\theta = 90°$ and $\phi = 20°$ in the installed case. Predictions using (a) the normalised TAGA results and (b) the scaled TAGA results.

Fig 4.44 shows the PSD for an observer slightly above the plate at $\phi = 20°$. In both version of the TAGA predictions, the agreement is not as good as under the plate with a under estimation at the high frequencies linked to the shielding. The scaling of the PSD allows for a better peak amplitude and reduces the under prediction above 4 kHz. The same behaviour under 1 kHz can be observed.

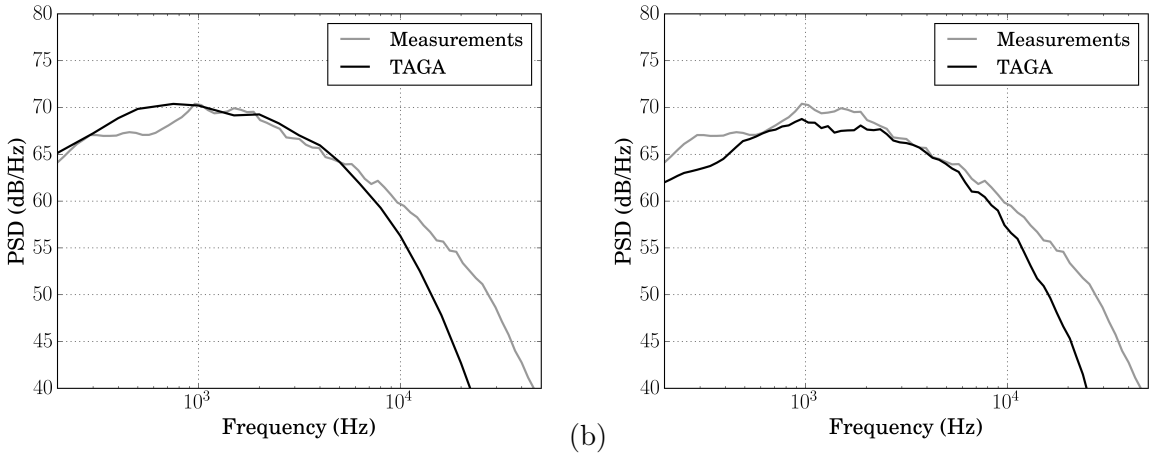

Figure 4.45: PSD for an observer at a polar angle of $\theta = 90°$ and $\phi = 80°$ in the installed case. Predictions using (a) the normalised TAGA results and (b) the scaled TAGA results.

The PSD spectra are plotted in Fig 4.45, at an azimuthal angle of $\phi = 80°$, meaning that the observer is located above the plate. Here, the scaled spectrum agrees slightly more with the measurements than with the previous fit, especially in terms of shape and peak frequency. Nevertheless, this confirms the previously stated drawbacks of this method with an over estimation of the shielding effect above 6 kHz. The agreement under 1 kHz is deteriorated but as mentioned before an interaction between the flat plate and the hydrodynamic pressure field around the jet causes a augmentation of the noise level at these frequencies. This phenomenon is not linked to

fine scale turbulence so the agreement at this frequency range cannot be discussed.

To conclude, the use of the scaling method to predict the installation effect turns out to be more effective than using the absolute predictions corrected with Eq (4.2) mainly due to the change of the shape of the spectrum. Moreover, these improved results come at the same cost as the OASPL correction because both need the measurements for the isolated case. In terms of quality of the predictions, the method is of industrial standard for all observers under the plate. The fact that this process works also shows that the installation effects scale linearly. A possible defect of this method should however be addressed. The performance of the scaling process is conditioned by the quality of the isolated measurement. If they are polluted by experimental errors, these anomalies will appear in the scaled spectra.

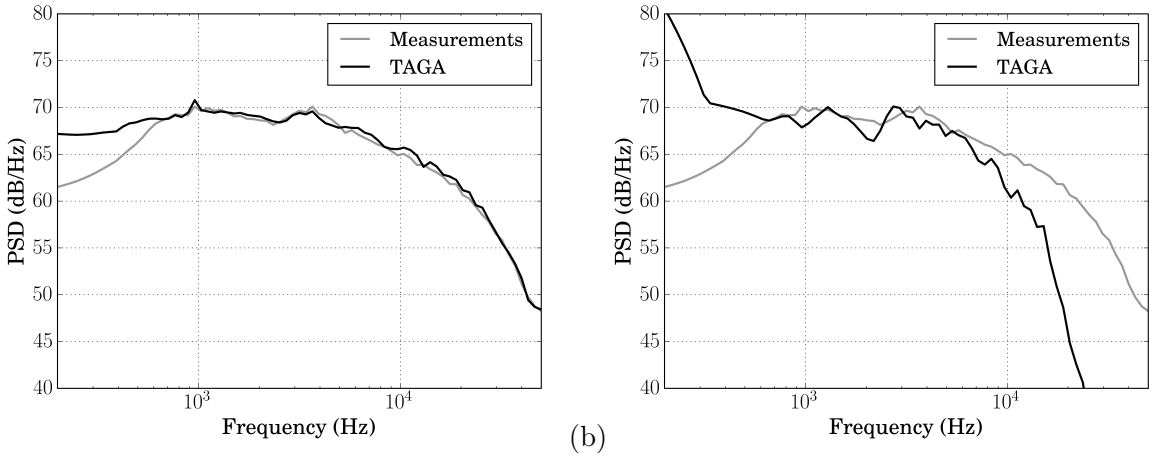

Figure 4.46: PSD for an observer at a polar angle of $\theta = 90°$ and $\phi = 340°$ in the installed case. Results using (a) measurements and (b) a LES for the scaling of the TAGA predictions.

Finally, this scaling process has been performed using experimental data as a base spectrum but it could be done using other type of data. Fig 4.46 shows the comparison between the use of measurements or a LES as a base of the scaling. Between 1 kHz and 10 kHz, both scaling show good results. The cut-off frequency of the LES used is around 10 kHz and makes the comparison impossible above. Considering that no experimental data was used in this prediction, this method shows promising results for an industral application. It is also believed that the use of a well resolved LES could allow the prediction on the full frequency range.

4.3 Noise predictions on a realistic nozzle

4.3.1 EXEJET nozzle

4.3.1.1 Description of the configuration

The second jet used is the EXEJET nozzle designed by Safran. The experiments were conducted at CEPRA19 wind tunnel from Onera, Saclay, France. This dual flow nozzle has a core of diameter 130 mm and a bypass of diameter 220 mm. Various configurations were tested in the

frame of the EXEJET project. Two of them have been selected for this study, namely the isolated configuration with and without chevrons, see Fig 4.47. The measurements as well as the present numerical prediction are both made at conditions matching the sideline certification point, meaning a Mach number for the primary flow of $M_{\text{core}} = 0.68$, for the secondary flow $M_{\text{fan}} = 0.84$ and thus a jet mixing Mach number of $M_{\text{jet}} = 0.78$. The external flow Mach number is $M_{\text{ext}} = 0.23$. This operating point provides realistic flow conditions, a validated jet noise signal and a sizeable flight effect. The noise is measured using a polar microphone arc of radius $R = 6\,\text{m}$. The jet is coaxial even though this is not taken into account in the model and with a temperature ratio $T_{\text{core}}/T_{\text{fan}} = 2.43$. More information can be found in Huber *et al.* [38]. This study being partially confidential, the absolute noise levels are not shown. The following convention will be used for the presentation of the results. The experimental data is plotted in grey and the predicted spectra in black. The round nozzle data is represented with dashed lines and the data from the nozzle with chevrons is in full line. This convention is summarised in the following table.

	Measurements	TAGA
Round nozzle	- - -	- - -
Chevron nozzle	——	——

Table 4.6: Convention used for the plots presented in this section.

(a) 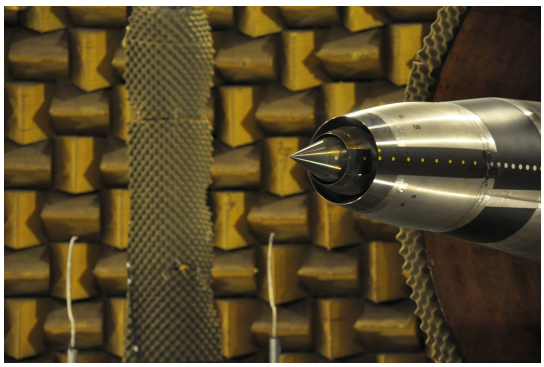 (b) 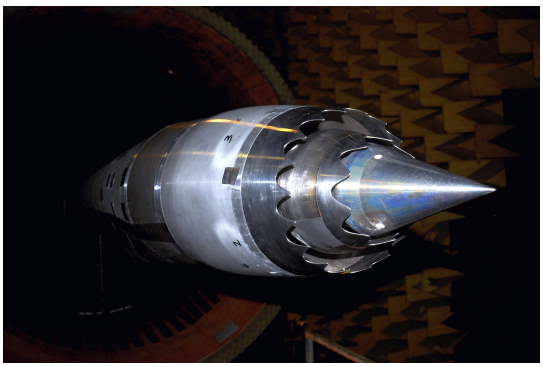

Figure 4.47: EXEJET nozzle (a) without chevrons (b) with chevrons.

4.3.1.2 RANS inputs

The same validation of the refinement of the mesh as performed in Section 4.2 is reproduced for the EXEJET nozzle The results obtained by the TAGA model, with both media set equal, are compared to the analytical solution of the propagation in free field. The difference in dB is plotted in picture Fig 4.49 (a) and the equivalent error margin is plotted in Fig 4.49 (b). The range in which there is a good agreement between the two predicted noise levels is the same as with the single-jet nozzle. Indeed, both power spectral density match between 100 Hz and 10 kHz. There are some discrepancies outside of this range that can be explained by the same reasons presented in Section 4.2. Fig 4.48 shows measurements at a polar angle of $\theta = 90°$ and highlights

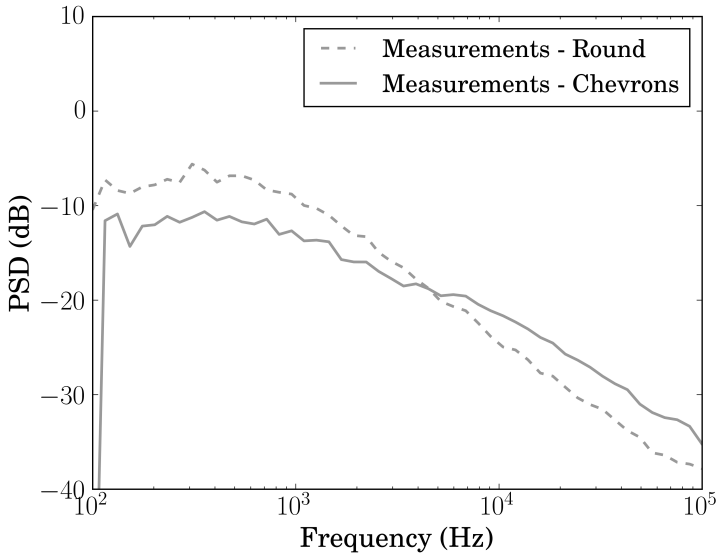

Figure 4.48: Experimental measurements of the PSD at $\theta = 90°$ with and without chevrons.

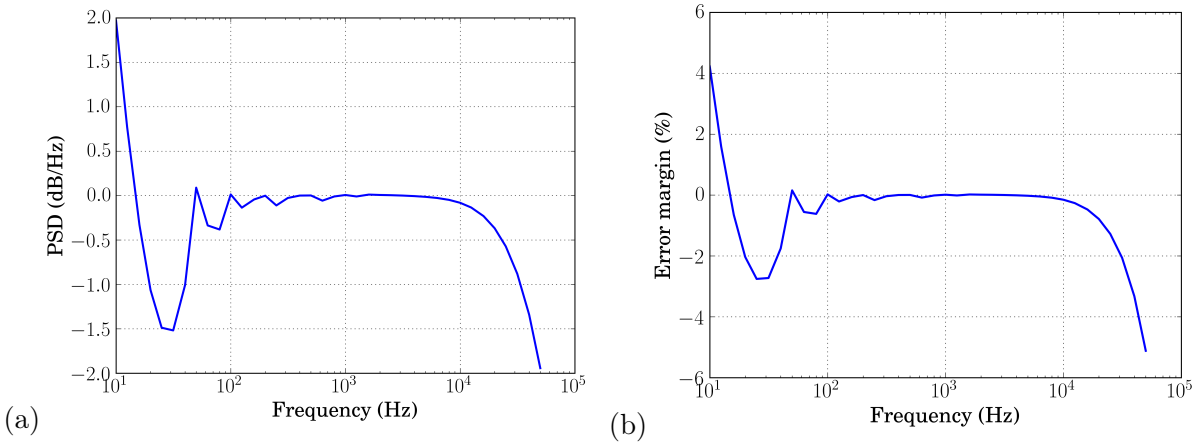

(a) (b)

Figure 4.49: Difference between the PSD using Acti-HF and using the analytical solution. (a) Absolute error (b) Error margin.

the fact that the frequency range on which the mesh is fine enough corresponds to the range of interest of the study.

The validity of the far-field and compactness approximations are also checked. The length scale $L = 3l_s/\sqrt{\ln 2}$ is used again as a measure of the distance of correlation. The same evaluation presented in the previous section is done here at 100 Hz, 1 kHz and 10 kHz. The results are shown in Table 4.7. Over the whole spectrum, L is inferior or greatly inferior to both the diameter of the nozzle and the wavelength. The far-field and compactness approximations are therefore validated.

4.3.2 Refraction effects

The objective of this subsection is the evaluation of refraction effects as predicted by TAGA. Unlike the previous studied nozzle, there are several major differences between the actual flow

	100 Hz	1 kHz	10 kHz
λ	$17\,D$	$1.7\,D$	$0.17\,D$
L	$0.5\,D$	$0.2\,D$	$0.05\,D$

Table 4.7: Estimate of the wavelength λ and the scale length L normalised by the jet nozzle diameter.

and its modelling. The subject is a coaxial jet, which means that considering the first medium containing the jet flow as homogeneous is even more debatable. The presence of entropic sources and density gradients are also expected for such a hot jet, even though the model does not take them into account.

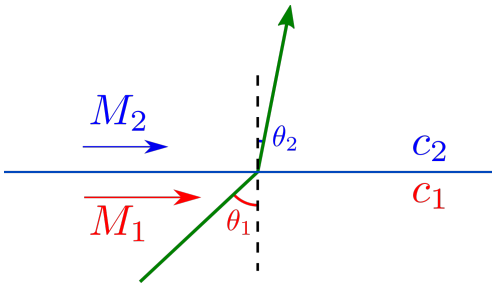

Figure 4.50: Representation of a ray with a refraction

The presence of a cone of silence is a trademark of refraction effects. The value obtained numerically is compared to the theoretical value obtained using the Snell law, reminded below,

$$\frac{c_1}{\sin\theta_1} + V_1 = \frac{c_2}{\sin\theta_2} + V_2 \tag{4.7}$$

where the notation are displayed in Fig 4.50 with $V_1 = M_1 c_1$ and $V_2 = M_2 c_2$. From this equation, the critical angle θ_c corresponding to the cone of silence (COS) can be obtained by setting $\theta_1 = \theta_{\text{jet}} = 90°$. Its expression is given by

$$\theta_c = \arcsin\left(\frac{c_2}{c_1 + (V_1 - V_2)}\right) \tag{4.8}$$

In this case $V_1 = V_{\text{jet}} = 291$, $V_2 = V_{\text{ext}} = 91$, $c_1 = c_{\text{jet}} = 368$ and $c_2 = c_{\text{ext}} = 333$. That gives the theoretical value $\theta_c = 36°$. From Fig 4.50, the angle for which the cone of silence appears is linked to this critical angle by $\theta_{\text{COS}} = \theta_c + 90° = 126°$. Fig 4.51 shows the polar evolution of the OASPL. The cone of silence begins to appear downstream for angles larger than 100° but the predicted noise level drops above 120°. This behaviour agrees well with the theoretical value of the cone of silence $\theta_{\text{COS}} = 126°$. This decrease in energy is not present in the experimental data because downstream, the large scale jet mixing noise dominates the spectrum. This noise mechanism is not affected by the refraction in the same way as fine scale turbulence because of the size and the nature of these structures. Indeed their characteristic lengths are too large

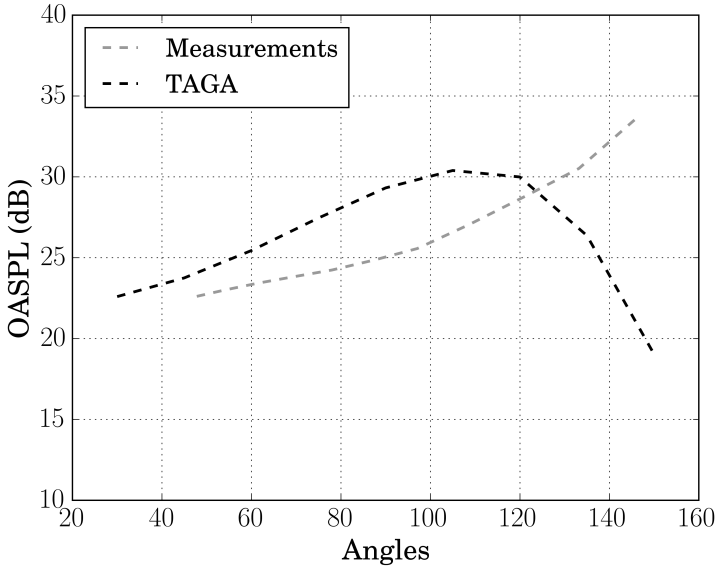

Figure 4.51: Polar evolution of the measured and predicted OASPL in the configuration without chevrons.

compared to the jet plume and therefore they radiate noise directly outside of the mixing layer and not through it. In terms of evolution, before the apparition of the cone of silence, the increase in OASPL is of 0.45 dB every 10° in the measurements whereas the increase rate is twice as much with 0.9 dB every 10° according to TAGA.

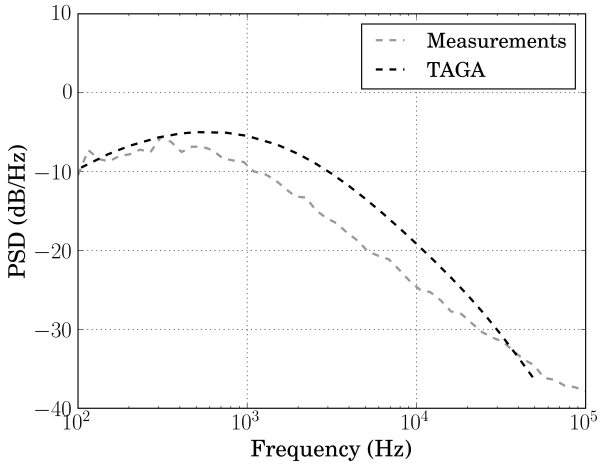

Figure 4.52: PSD for an observer at a polar angle of $\theta = 90°$.

The predicted power spectral density is now compared to the experimental data. Fig 4.52 shows the results at $\theta = 90°$. This position can be considered free of the contribution of jet mixing noise from large scale turbulence. In a similar manner as the single jet predictions, the shape of the spectrum is close but does not match the experimental data, it is even more the case with the EXEJET nozzle. The shape of the spectrum is directly linked to the source modelling so the discrepancies can be due to any combination of the following causes. First, neither the model function of the autocorrelation of the source terms nor the scaling parameters take into account

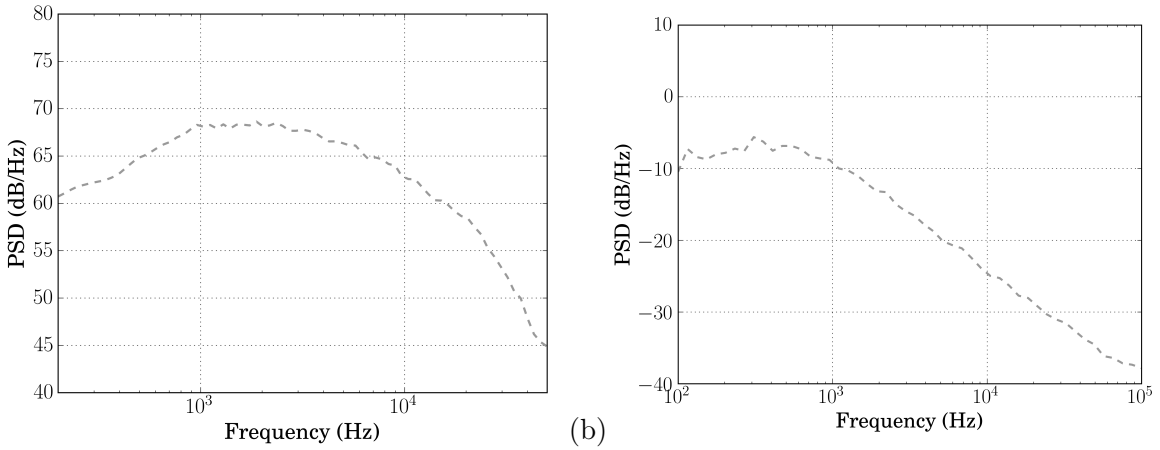

Figure 4.53: PSD for an observer at a polar angle of $\theta = 90°$ for (a) the single jet (b) the coaxial jet.

the variation of density in hot jets as introduced by Tam *et al.* [81]. It is however suprising that in [78], their model scales well with heated jets although, by construction, the effects linked to the temperature are not present. Then, the constants used for the scaling parameters were obtained by Tam [78] by best fit on single jets. It is possible that the introduction of a primary flow changes enough the behaviour of the mixing layer that a new set of constants is needed to maintain an accurate description of the turbulence. The comparison of a spectrum of the single jet with one of the coaxial jet, in Fig 4.53, highlights this change of shape. In this study the peak amplitude is however well enough caught by the model so that there is no need of a correction like in Section 4.2.

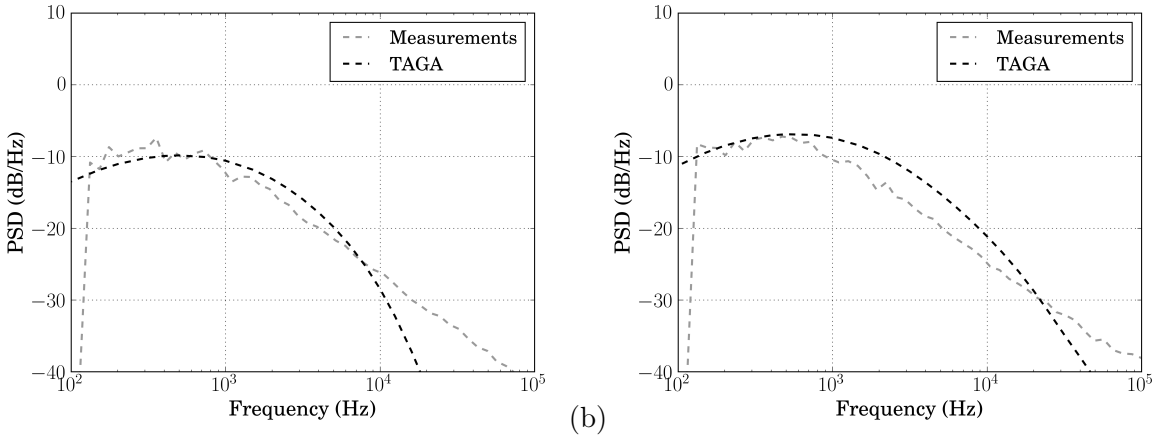

Figure 4.54: PSD for an observer at a polar angle of (a) $\theta = 45°$ and (b) $\theta = 75°$.

The results are presented using the convention reminded in Table 4.6. The predictions for two microphones located at $\theta = 45°$ and $\theta = 75°$ are presented in Fig 4.54. Although the peak amplitude is caught well enough by the model, there is an over prediction of the peak frequency. The shape of the spectrum is also off, especially at high frequency. This is explained by the shielding, by the nozzle, of the zone responsible for high to very high frequency. Less rays are

blocked when the polar angle increases, hence the rise of the noise level over 10 kHz for $\theta = 75°$ relatively to $\theta = 45°$.

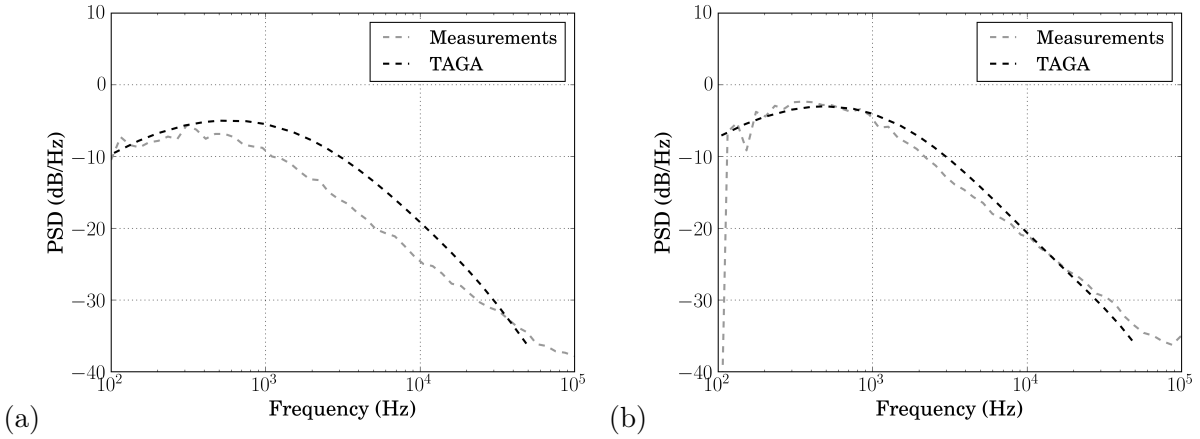

Figure 4.55: PSD for an observer at a polar angle of (a) $\theta = 90°$ and (b) $\theta = 120°$.

The results for $\theta = 90°$ and $\theta = 120°$ are presented in Fig 4.55. The agreement in terms of peak amplitude is still good and the peak frequency is still over predicted. For these observers, the decrease of the noise level after the peak with TAGA gets more linear and although the slope is steeper than in the experiment, the right behaviour is predicted. With this improvement comes a good overall prediction of the spectrum shape for observers located in this zone.

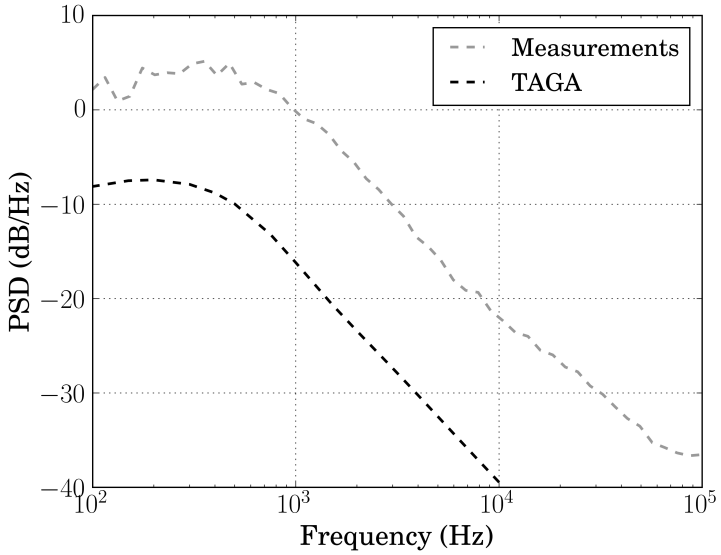

Figure 4.56: PSD for an observer at a polar angle of $\theta = 150°$.

Fig 4.56 shows the comparison between the predictions and the experimental data for an observer placed downstream, past the cone of silence. In the measurements, an inflection around 4 kHz for $\theta = 150°$ can be seen, suggesting the emergence of the large scale turbulence spectrum. This additional source, which is not taken into account in the model, coupled with the noise reduction in the cone of silence, induces a noticeable deficit in energy of 10 dB over the whole frequency range for $\theta = 150°$. Given the trends presented in Fig 4.51, the poor agreement above

a polar angle of 105°-120° was expected.

In this section was presented the predictions of refraction effects with a polar study on the EXEJET nozzle. Compared to the previous nozzle, there is a wider range of differences between the real jet plume and the modelled flow in TAGA, as mentioned previously in this subsection. Considering the amount of aspects not included in the prediction model and the fact that no fit was done to improve the calculations, the results can be considered encouraging. The right trend of the polar evolution of the OASPL is predicted with the presence of the cone of silence at a value close to the theory. Moreover, the peak amplitude is overall well caught at all positions below 120°. In their paper, Tam *et al.* [81] stated that their updated model showed very promising results on coaxial jets. It would be interesting to see if this new formulation could lead to improved predictions.

4.3.3 Predictions with chevrons

In this subsection, the model is used to predict the effects of chevrons on nozzles. The scaling method introduced in Sec 4.2 showed great results. The satisfying performance is in part due to the use of a base spectrum of the same nozzle, which produces a spectrum with a shape that is very close to the experimental data. The relative impact of the introduction of chevrons as computed by TAGA is therefore applied on the measurements of the round nozzle giving the following formula for the scaled spectrum,

$$\mathrm{PSD}_{\mathrm{chevrons,scaled}} = \left(\mathrm{PSD}_{\mathrm{chevrons,TAGA}} - \mathrm{PSD}_{\mathrm{round,TAGA}}\right) + \mathrm{PSD}_{\mathrm{round,exp}} \tag{4.9}$$

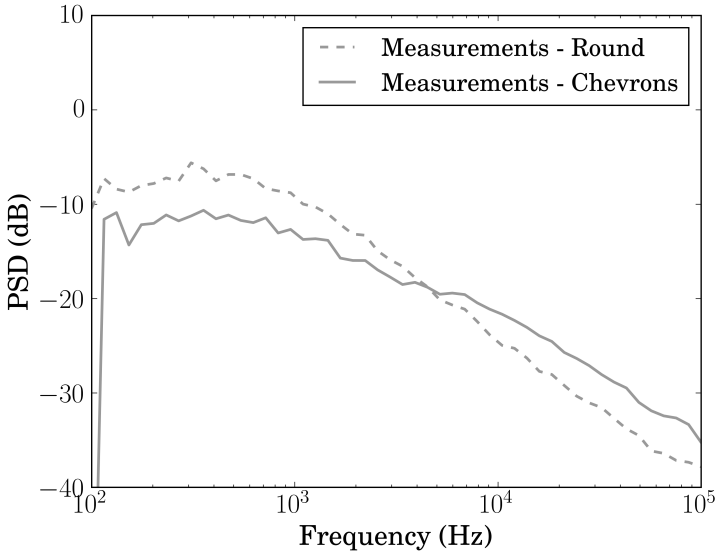

Figure 4.57: Comparison of measured PSD of the round and chevron nozzle at a polar angle of $\theta = 90°$.

The introduction of chevrons leads to an increase of the turbulent kinetic energy near the nozzle exit forcing the mixing of the jet in the external flow, early in the jet plume. This increase

of the turbulence field has a second impact. With the improvement of the mixing, the potential core is reduced and the turbulent kinetic energy field is attenuated further downstream [21]. In terms of power spectral density, these two modifications in the topology of the flow translate respectively to an increase of the noise level at high frequencies. Fig 4.57 shows the comparison at $\theta = 90°$ between the round and chevron nozzle. Both modifications of the spectrum are present with a reduction of around 5 dB at the peak and a relatively constant increase of 3 dB above 5 kHz.

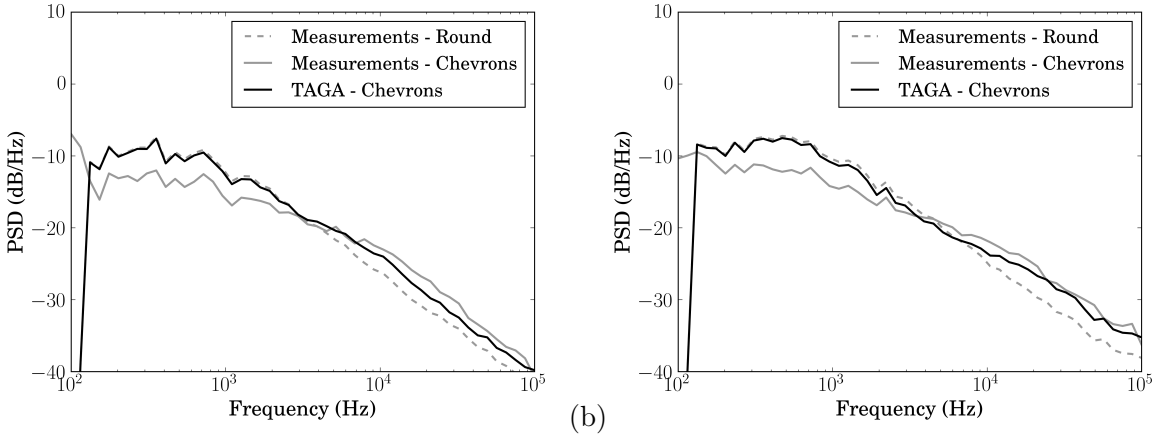

Figure 4.58: PSD for an observer at a polar angle of (a) $\theta = 45°$ and (b) $\theta = 75°$.

The results are presented using the convention reminded in Table 4.6. The results for microphones located at $\theta = 45°$ and $\theta = 75°$ are presented in Fig 4.58. Of the two expected impacts of the installation of chevrons, only the increase at high frequency is present. Fig 4.59 shows a map of the turbulent kinetic energy field k_t for both nozzles. Above is the nozzle with chevrons and below is the round nozzle. As explained above, there is a local increase right after the nozzle exit followed by a reduction of k_t around the potential core. In terms of source domain, that translates to the results presented in Fig 4.60 for the peak frequency $f = 400$ Hz and in Fig 4.61 for the frequency $f = 10000$ Hz. The increase of the source amplitude at high frequency at the nozzle exit is noticeable in Fig 4.61. A_S is more important above for the nozzle with chevrons as below for the round nozzle. At the frequency of the peak, the reduction of the source term A_S is however not as clear as with the k_t field. Both source domains are similar with only a slight reduction with the introduction of the chevrons. This will lead to a negligble reduction of the noise level at the peak in the spectra. At the time of writing, no definitive explanation can be given for the absence of noise reduction at the hump of the spectrum. On the one hand, it is unknown if the RANS computations are accurate by not predicting a heaver reduction of k_t more around the potential core. On the other hand, the source model from the Tam and Auriault could also be at fault too because only the strong variations of k_t translate to a modification of the source amplitude A_S.

The noise predictions for microphones at $\theta = 90°$, $\theta = 120°$ and $\theta = 150°$ are shown in Fig 4.62 and Fig 4.63. The conclusions drawn for observers located upstream can be generalised

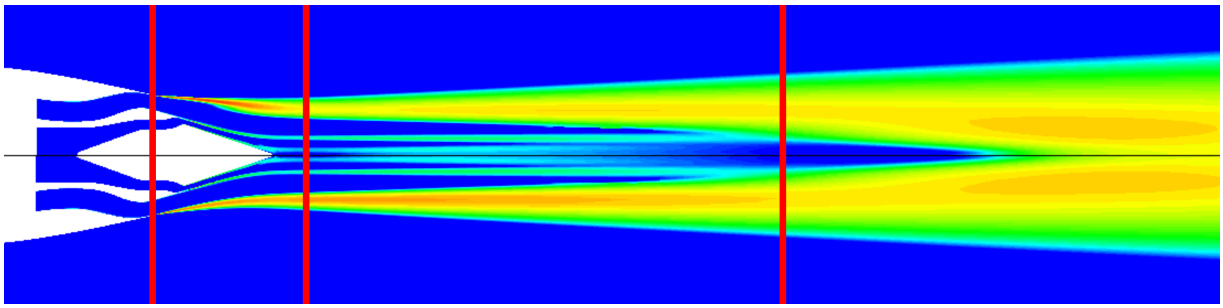

Figure 4.59: Map of the turbulent kinetic energy field k_t for the nozzle with chevrons (above) and the round nozzle (below).

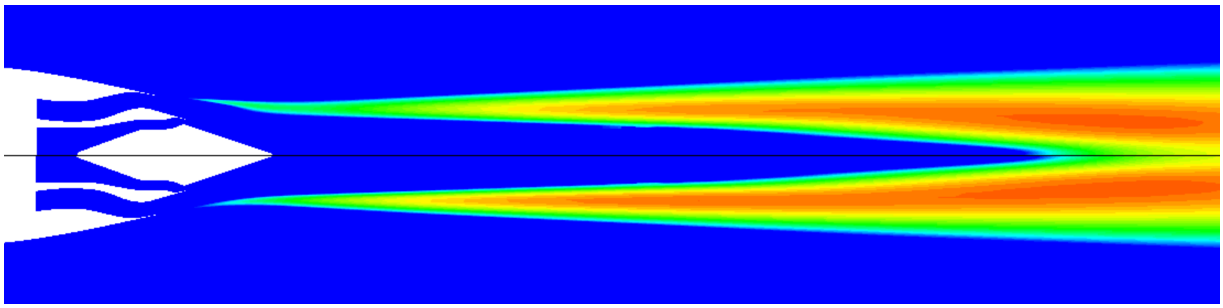

Figure 4.60: Map of the source term A_S at $f = 4000\,\mathrm{Hz}$ for the nozzle with chevrons (above) and the round nozzle (below).

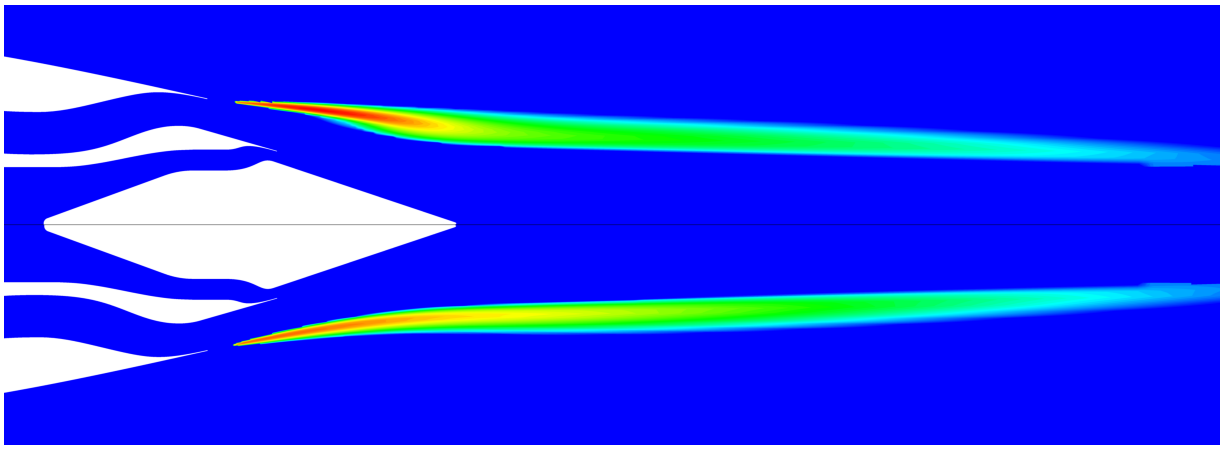

Figure 4.61: Map of the source term A_S at $f = 10000\,\mathrm{Hz}$ for the nozzle with chevrons (above) and the round nozzle (below).

for these polar positions. The noise level at the peak matches the one from the round nozzle meaning that TAGA does not predict any difference between the two nozzles. Concerning the noise amplification at higher frequencies, the level is also well caught with around a 3 dB increase. The start of this amplification is however still late with an increase of this difference with the polar angle.

The use of TAGA as a scaling tool for the prediction of the installation of chevrons has been presented in this subsection. If the TAGA model was unable to predict the noise reduction at low frequencies, good results were obtained regarding the high frequency behaviour. As of now

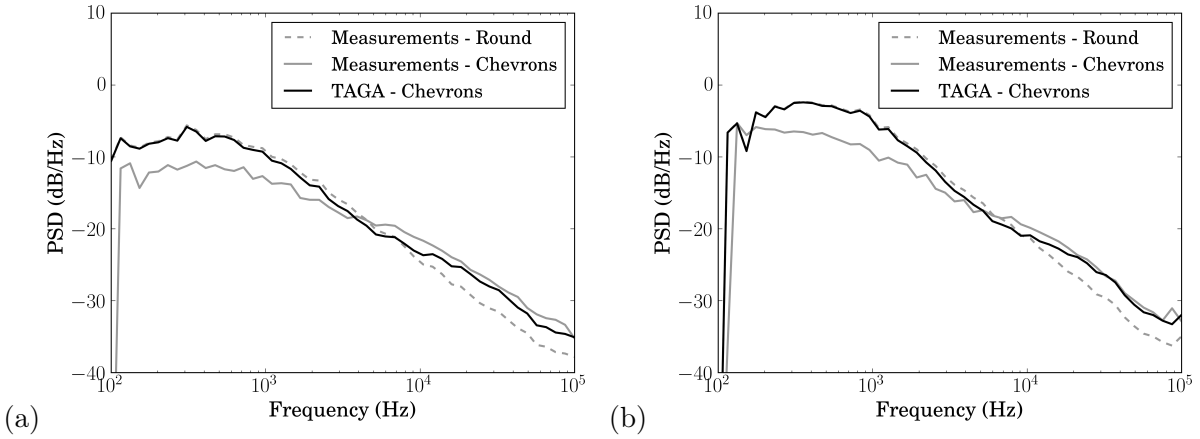

Figure 4.62: PSD for an observer at a polar angle of (a) $\theta = 90°$ and (b) $\theta = 120°$.

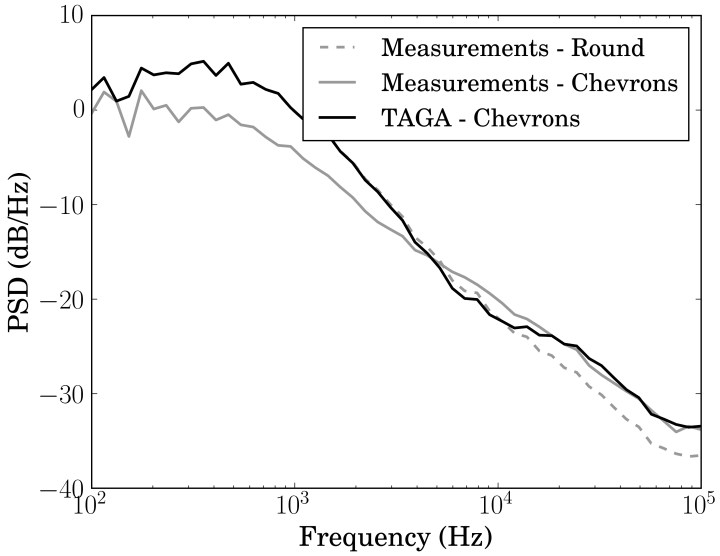

Figure 4.63: PSD for an observer at a polar angle of $\theta = 150°$.

the noise prediction model does not seem mature enough for this kind of study. In a similar way as done by Bodard *et al.* [14] absolute predictions using a LES and relative predictions using this model could be used to predict respectively the low and high frequencies. Preliminary results are given in Fig 4.64 with the LES under 5 kHz and TAGA above. With this new method, there are encouraging results for all frequencies over 300 kHz. This would also allow the use of a less resolved LES as what would be needed for predictions on the full frequency range.

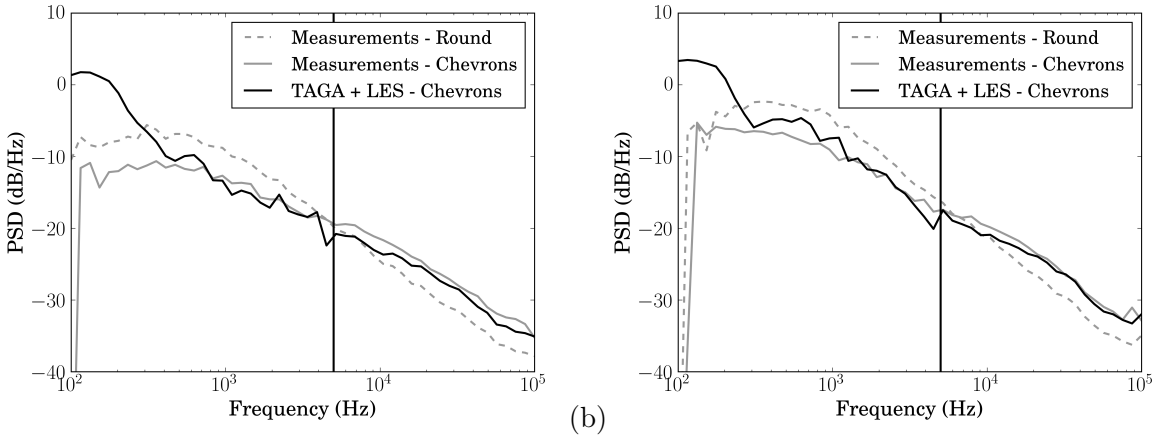

(a) (b)

Figure 4.64: PSD for an observer at a polar angle of (a) $\theta = 90°$ and (b) $\theta = 120°$ using a hybrid formulation of TAGA and a LES.

5 Conclusion and perspectives

5.1 Summary

The objective of this study was to introduce a prediction model for jet mixing noise, and more specifically for fine scale turbulence. This model had to take into account mean flow effects, namely the convection and refraction of the sound waves in the jet flow. Installation effects had to be included too, in particular the reflection, diffraction and shielding of the sound waves caused by the wing. The investigation of realistic three dimensional configurations should be possible within a reasonable computing time.

The second Chapter introduced the concept of acoustic analogies. Although several versions had been derived over the past few years, it was pointed out that similarities in the mathematical formulation could be identified. Indeed, two main parts appear in the expression of the power spectral density. The first element is the autocorrelation of the source term from the chosen analogy. A review of the literature showed that a statistical modelling of this source correlation fed with data from a RANS computation constituted an efficient way of obtaining this first term. The second element in the formula of the PSD accounts for the propagation of the sound waves and its expression corresponds to the solution of the differential equation of the desired acoustic analogy. It was explained that an analytical resolution was only possible for models assuming the flow is uniform whereas models with more detailed flow descriptions required heavy numerical means. Considering the available methods and the industrial framework, it was chosen to use the work performed by Tam and Auriault [78] as a starting point and to substitute the adjoint Green function used for the computation of the propagation by the use of geometrical acoustics applied to a simplified propagation medium.

The prediction model has been analytically derived in a third Chapter built in two major steps. First, the methodology introduced by Tam and Auriault [78] has been carefully analysed. The linearised Euler equations forced by a tailored source term were used as a starting point. The resolution was performed using adjoint Green functions and allowed the expression of the fluctuating pressure and subsequently the power spectral density in an integral form. A model function of the source autocorrelation was substituted in that integral to permit the computation of the source amplitude. Tam and Auriault then recast the mathematical formulation to perform

one of the two spatial integration by means of far field and compactness approximations, thus cutting down the computational cost of this method. In the original work, the PSD was finally obtained by numerically computing the adjoint fluctuating pressure. Second, it is shown how the methodology could be altered to save the cost of this numerical calculation. The first step was to simplify the flow description by approximating the propagation medium into two homogeneous media, namely the jet itself and the external flow. The pressure in the far field was then expressed using geometrical acoustics. Next, a modified formulation of the Tam and Auriault model has been derived to isolate that the propagation term in the alternative formulation could be computed using a ray tracing tool instead of the costly numerical resolution of the adjoint pressure in the original formulation. The name TAGA (Tam Auriault - Geometrical Acoustics) was given to this prediction model.

The newly developed model was applied to several configurations in Chapter four. It was chosen to predict jet mixing noise on two types of nozzles. The first jet is a cold single jet and constitutes a good validation case because of its simplicity. The second, from the EXEJET research program, is a hot coaxial jet that is closer to an industrial nozzle. The prediction of installation effects was first investigated through a study on the whole azimuthal range for the single jet. The jet Mach number was $M = 0.9$ and a flat plate located at 2 D was used to introduce installation effects. The results on the installed configuration were first presented with a correction on the absolute level. This offset is the difference between the OASPL of the predictions and the experimental data in the isolated configuration. Although the shape of the spectrum did not exactly fit the measurements, a good agreement was found for observers located under the plate and for frequencies above 1 kHz. The shielding by the plate seemed however over predicted by TAGA leading to an under estimation at high frequency. The analysis of the results highlighted a peak in the experimental data that was well captured by the model. An in-depth investigation of the predictions showed an interference phenomenon between rays that exit the jet plume and rays that reflect on the wing. The presence of either a constructive or a destructive interference fringe coincided with respectively the local increase or decrease of noise level in the experimental data, indicating that it was indeed the right interpretation of the phenomenon. An improved approach for the computation of noise levels for installed configurations was then introduced. The difference between the installed and isolated predictions is added to the measured isolated spectrum. The use of this technique improved the agreement both in terms of peak frequency and shape of the spectrum. The updated results showed excellent results for microphones under the wing at 1 kHz and above, while the same issues linked to the shielding at high frequencies remained. This new approach for the presentation of the results showed that the improvement of the shape of the spectrum could be done without fitting the scaling parameters in the model. The EXEJET configuration was used for the evaluation of refraction effects. Although TAGA provided an accurate prediction of the cone of silence, the shape of the spectra showed a poor agreement with the experimental data. It is believed that these issues were caused by the disparities between the real jet flow and the reduction to homogeneous media in TAGA. The last study was the

prediction of the effect of chevrons on jet mixing noise. The scaling method was used again to improve the shape of the predicted spectra. Chevrons induce a reduction of the peak amplitude and an increase of the PSD at high frequency. Only the latter effect was accurately predicted with a good agreement of the extent of the noise amplification.

Overall, the results were deemed satisfactory, especially so with the predictions of installation effects and despite the amount of simplifications done regarding the description of the flow. The introduction of a method with a good ratio between performance and cost has been successful. Indeed, the target in terms of restitution time was reached with the possibility to obtain results on a full test matrix in under a week.

5.2 Main results

The main contributions of the present manuscript are the following,

- A new model named TAGA has been introduced. The model developed by Tam and Auriault [78] has been reformulated using a simplified flow description to allow for the resolution of the propagation with geometrical acoustics. The account of mean flow and installation effects are therefore possible while maintaining a low computation time.

- TAGA showed good results for the prediction of jet mixing noise from fine scale turbulence when applied on installed jets. The agreement found with the experimental data was especially great for the whole azimuthal range under the flat plate, which includes the three certification positions.

- The use of TAGA as a scaling tool allowed to reach industrial standards for the quality of noise predictions with a maximum deviation of 1 dB for the frequency range of interest. A unique set of constants in the scaling parameters has been used during the whole study, giving accurate results without fit.

- The presence of a hump in the experimental data from installed jets, for observer located slightly under the flat plate, has been explained. The interference between rays refracting through the mixing layer and rays reflecting on the plate has been highlighted. This phenomenon was well caught both in terms of frequency and amplitude by TAGA.

- The prediction of the cone of silence due to refraction effects was achieved and a good match was found with the theoretical value for the polar angle corresponding to the cone edge. Although the base flow does not fully describe the complexity of a realistic nozzle, encouraging results were found for noise predictions of coaxial nozzles. The prediction of chevrons effects has been partially carried out with a reasonable estimation of the high frequency noise level increase.

- In terms of computation time, the target has been reached. As an illustration, the 114 calculations performed for the study presented in Section 4.2 were produced within a week time.

The work performed has been the topic of two conference papers,

- **Martelet, Y.**, Suratteau, J.-Y., Pont, G., and Bailly, C. (2019). Prediction of fine-scale jet mixing noise using geometrical acoustics. In *25th AIAA/CEAS Aeroacoustics Conference*, pp. 1–18.
- **Martelet, Y.** and Bailly, C. (2018). Prediction of fine scale jet mixing noise refraction effects using a two-step propagation technique. In *EURONOISE 2018*, pp. 135-142.

5.3 Perspectives

Although the TAGA model displayed satisfactory results in the different configurations studied, there is room for improvements. The model function and the scaling parameters used by Tam and Auriault could arguably be replaced by more recent and more advanced formulations which would hopefully lead to better results. Such formulations have been mentioned in Section 2.4. As an illustration, among the weaknesses pointed out in Chapter four, the poor agreement in terms of shape of the predicted spectra for the realistic nozzle is especially problematic. Indeed, in the frame of an industrial use, better performance are expected on hot coaxial jet. The first lead to investigate would be the implementation of the extension of the Tam and Auriault model by Tam *et al.* [81]. This updated model was developed to include the impact of density gradients from high-temperature jets. Moreover, in their conclusion, they also mention encouraging results regarding predictions on dual-stream jets. The use of scaling parameters function of the frequency as done by Self [71] [72] is also contemplated. Another lead in the improvement of the source modelling comes from the work by Karabasov *et al.* [40]. By deducing the constants used in the scaling parameters from the data from a LES, they obtained good results and remarkably so at positions were jet mixing noise from large scale turbulence dominates. This technique would also improve the robustness of the method for absolute predictions.

Further applications of the model would also answer some questions left opened. First, the single jet nozzle used in the study presented in Section 4.2 had the disadvantage of not having experimental data at polar angles under $\theta = 90°$. The assessment of refraction effects had therefore to be performed on a coaxial jet. This assessment should be repeated on a simpler nozzle to confirm that the less satisfactory results were due to the use of a nozzle outside of the model's range and not due to an issue with TAGA or Acti-HF. Furthermore, only the configuration with a flat plate far enough from the jet has been examined. By moving the plate closer, additional noise sources shall appear in the experimental data. A first estimation of the validity range of the model could be deduced by a parametric study consisting in the variation of the distance between the plate and the jet axis. The prediction of installation effects was successfully displayed

in the case of a flat plate. The introduction of a real wing in place of this plate is the next step for the validation of the method. On the matter of the implementation of the model, some improvements were already mentioned in Section 4.1. Indeed the production of the interface delimiting the jet and the external flow is done manually at the moment. This is also the case for the velocity data used for the definition of the homogeneous medium surrounding the jet. With the automatisation of these two steps, not only would the robustness of the method be increased but the flow definition would be also be improved. The issue with the over prediction of the shielding also has yet to be addressed. This could be explained by a physical effect that is not included in the TAGA model. It could also be due to an issue in the diffraction module of the ray tracing tool. Further investigations in that direction should remove that uncertainty.

Finally, one important limitation of the TAGA model for jet mixing noise prediction is the absence of the contribution from large scale turbulence. At the moment, the noise predictions are limited to observers located upstream and slightly above 90°. The addition of this noise mechanism would extend the model to the rearward polar angles. It is however unlikely that the method developed in this thesis could include this noise mechanism. Indeed, the hypothesis of compactness of the sources in the frame of geometrical acoustics seem incompatible with the size of the turbulent structures considered. The use of TAGA in coordination with another model focused on large scale jet mixing noise would be a more reasonable approach.

A Introduction to the Green and adjoint Green functions

A few mathematical tools are used in the core of this report. They are detailed in the following section to provide the reader with all the notions necessary to understand the calculations performed in the development of the different prediction models. First the Green functions and in particular the vectorial Green functions are introduced then the adjoint problem and the adjoint Green functions are presented.

A.1 Definition of the Green function

The introduction of the Green function has been motivated by the idea of solving a problem independently of its forcing term [69]. They can therefore be defined as the response to an impulse excitation of a boundary value problem. They are especially used in order to solve differential equations. An example of their use is given.

Let L be a linear operator such as

$$L(f(\vec{x},t)) = S(\vec{x},t) \tag{A.1}$$

The Green function f^G is defined this way

$$L(f^G(\vec{x},\vec{\xi};t,t_1)) = \delta(\vec{x}-\vec{\xi})\delta(t-t_1) \tag{A.2}$$

Upon finding f^G, f can be obtained using the convolution of the Green function and the source term S with

$$f(x,t) = \int_{\vec{\xi}}\int_{t_1} f^G(\vec{x},\vec{\xi};t,t_1)S(\vec{\xi},t_1)\mathrm{d}\vec{\xi}\mathrm{d}t_1 \tag{A.3}$$

The use of the Green function is then interesting on two levels. First, because f^G is independent of S, the same solution can be used for different excitation thus saving numerous resolutions of equations. Moreover the resolution itself is often easier since the source term is only an impulse.

A.2 Use of vectorial Green functions to solve a system of equation

The Green function has been presented in the previous subsection. The example given was for only one function f but in some case, several functions can intervene thus forming a vector of state variable. In this case, there are more than one differential equation governing the physics but the Green functions can still be introduced for the resolution of such problems.

That technique can be interpreted as a resolution by superposition. Instead of considering all the sources at once, the system is solved by considering only one source and switching off the others. This is repeated until all the different sources have been considered. Finally, all the elementary solutions are superposed so that it accounts for the real problem. For example, solving

$$\begin{aligned} L_1(f(\vec{x},t),g(\vec{x},t)) &= S_1(\vec{x},t) \\ L_2(f(\vec{x},t),g(\vec{x},t)) &= S_2(\vec{x},t) \end{aligned} \tag{A.4}$$

where L_1 and L_2 are two linear operators, can be done by first solving these two systems

$$\begin{aligned} L_1\left(f^{(1)}(\vec{x},\vec{\xi};t,t_1),g^{(1)}(\vec{x},\vec{\xi};t,t_1)\right) &= \delta(\vec{x}-\vec{\xi})\delta(t-t_1) \\ L_2\left(f^{(1)}(\vec{x},\vec{\xi};t,t_1),g^{(1)}(\vec{x},\vec{\xi};t,t_1)\right) &= 0 \end{aligned} \tag{A.5}$$

and

$$\begin{aligned} L_1\left(f^{(2)}(\vec{x},\vec{\xi};t,t_1),g^{(2)}(\vec{x},\vec{\xi};t,t_1)\right) &= 0 \\ L_2\left(f^{(2)}(\vec{x},\vec{\xi};t,t_1),g^{(2)}(\vec{x},\vec{\xi};t,t_1)\right) &= \delta(\vec{x}-\vec{\xi})\delta(t-t_1) \end{aligned} \tag{A.6}$$

Although there are now two systems, the resolution is easier overall. After finding $f^{(1)}$, $f^{(2)}$, $g^{(1)}$ and $g^{(2)}$, the solutions of the initial system are obtained with the convolution between the source terms at the right hand side of Sys (A.4) and the Green functions for either f or g, giving

$$f(\vec{x},t) = \int_{\vec{\xi}}\int_{t_1}\left[f^{(1)}(\vec{x},\vec{\xi};t,t_1)S_1(\vec{\xi},t_1) + f^{(2)}(\vec{x},\vec{\xi};t,t_1)S_2(\vec{\xi},t_1)\right]\mathrm{d}\vec{\xi}\mathrm{d}t_1 \tag{A.7}$$

$$g(\vec{x},t) = \int_{\vec{\xi}}\int_{t_1}\left[g^{(1)}(\vec{x},\vec{\xi};t,t_1)S_1(\vec{\xi},t_1) + g^{(2)}(\vec{x},\vec{\xi};t,t_1)S_2(\vec{\xi},t_1)\right]\mathrm{d}\vec{\xi}\mathrm{d}t_1 \tag{A.8}$$

A.3 Definition of the adjoint problem and the adjoint Green function

Finally, the adjoint problem is defined. Let L be a linear differential operator, f a state variable and S a source term so that $L(f(\vec{x},\vec{\xi})) = S(\vec{x},\vec{\xi})$ or in short $L(f) = S$. The adjoint operator L^a and the adjoint state variable f^a are defined this way [75]

$$\langle f^a, L(f)\rangle = \langle L^a(f^a), f\rangle \tag{A.9}$$

with $\langle ., . \rangle$ a scalar product. Note that when working in the complex domain this scalar product is also Hermitian. An adjoint source S^a can be defined in a similar manner as S so that $L^a(f^a) = S^a$.

It can be noted that L^a, f^a and therefore S^a are not unique but dependent on the choice of the scalar product. By introducing the Green function f^G solution of L there is $L(f^G(\vec{x}, \vec{\xi})) = \delta(\vec{x} - \vec{\xi})$ and in a similar way $L^a(f^{a,G}(\vec{x}, \vec{\xi})) = \delta(\vec{x} - \vec{\xi})$.

In the case of a scalar equation, meaning that f^G and therefore $f^{a,G}$ are scalars and not vectors, a relation between the direct and adjoint Green functions can be obtained as demonstrated in [75]

$$f^{a,G}(\vec{x}, \vec{\xi}) = \left[f^G(\vec{\xi}, \vec{x}) \right]^* \tag{A.10}$$

where * is the complex conjugate.

B Geometrical acoustics

B.1 Introduction of geometrical acoustics

At a frequency high enough, it can be assumed that the amplitude and the direction of propagation vary only slightly over distances of the order of the wavelength as explained by Landau and Lifshitz [44]. In this case the sound wave can be assimilated as a plane wave. In the frame of this approximation, geometrical acoustics describe the wave propagation as a ray which respects geometrical rules that are explained in this appendix.

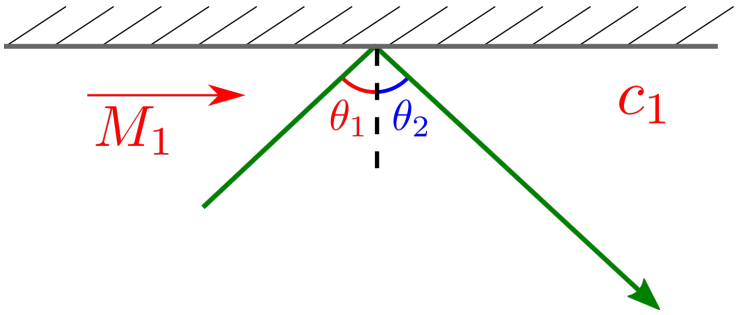

Figure B.1: Representation of a ray with a total reflection

The surrounding medium can change the wave path in several ways. First, the presence of a surface will induce a reflection of the wave, an example is pictured in Fig B.1. The angle between the incident ray and the normal to the surface is equal to the angle between the reflected ray and the normal to the surface. Giving

$$\theta_1 = \theta_2 \tag{B.1}$$

Depending on the type of interface, there can be a total reflection meaning that the amplitude of the wave stays the same between the incident and the reflected rays or there can be a dissipation of energy with the split of the incident wave into a reflected wave and a transmitted one. The passage from one medium to another is called a refraction and is pictured in Fig B.2

In this case, the relation between the two refraction angles is given by the Snell-Descartes law, with $V_1 = M_1 c_1$ and $V_2 = M_2 c_2$,

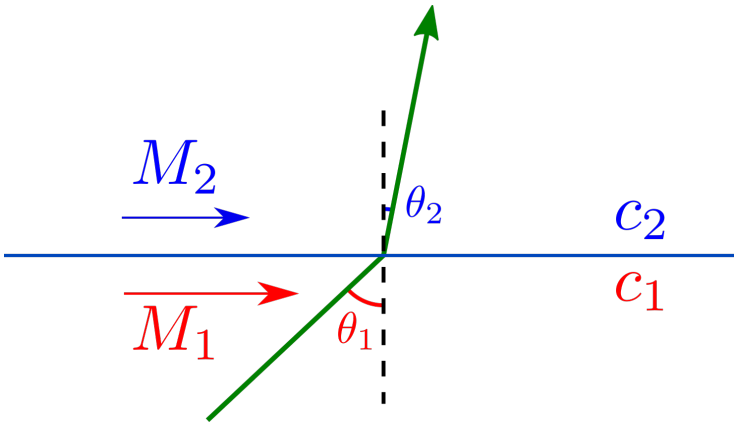

Figure B.2: Representation of a ray with a refraction

$$\frac{c_1}{\sin\theta_1} + V_1 = \frac{c_2}{\sin\theta_2} + V_2 \tag{B.2}$$

This formula is only true in the case of two coplanar velocities. If this is not the case, the incident ray, the refracted ray and the normal to the surface are not coplanar anymore and the Snell-Descartes law has to be recast as,

$$\frac{c_1}{\sin\theta_1} + V_{1,proj} = \frac{c_2}{\sin\theta_2} + V_{2,proj} \tag{B.3}$$

with V_{proj} the projected velocity on either of the refraction plans. The refraction plan contains one of the rays and the normal to the surface.

As seen in Eq (B.2), the path of the way is deviated depending on the properties of both media. In the case of sources in the jet, the situation in terms of indices of media is such that the ray will diverge their path away from the jet axis. It will give a directivity to the noise mechanism by highly reducing the noise level downstream. This is described as a cone of silence in Tam *et al.* [80].

B.2 Expression of the pressure after a refraction or a reflection

In this section, the mathematical formulation of the pressure after any number of reflection or refraction is presented. For simplicity the term event is used to designate either a reflection of a refraction. Obviously the nature of the event has an impact on the formula but a standardised term will help the understanding.

B.2.1 The transmission and reflection coefficients

The impact of the refraction and the reflection on the wave path has been explained, now the effect on the amplitude is also described. As mentionned above, by going through a change of

medium and switching propagation indices, the ray is split in two parts. Both are attenuated by a factor. The reflection factor K_R is given in Section 11.1 from [59] in the case of a ray going from a medium 1 to a medium 2.

$$K_R = \frac{\rho_2 c_2^2 \sin(2\phi_1) - \rho_1 c_1^2 \sin(2\phi_2)}{\rho_2 c_2^2 \sin(2\phi_1) + \rho_1 c_1^2 \sin(2\phi_2)} \tag{B.4}$$

with

$$K_T = 1 + K_R \tag{B.5}$$

The refraction (or transmission) factor K_T is then

$$K_T = \frac{2\rho_2 c_2^2 \sin(2\phi_1)}{\rho_2 c_2^2 \sin(2\phi_1) + \rho_1 c_1^2 \sin(2\phi_2)} \tag{B.6}$$

Note that in [59], the angle ϕ used is the one between the ray and the surface. There is therefore the following relations between the two angles

$$\theta = 90 - \phi \tag{B.7}$$

It is straightforward to see that in case of a fully reflective surface $K_R = -1$ and $K_T = 0$.

B.2.2 The divergence coefficient

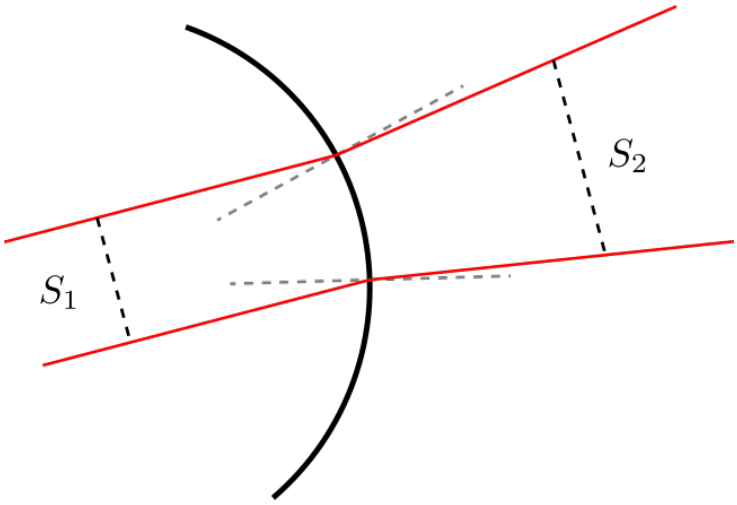

Figure B.3: Simple 2D representation of the divergence of the pencil ray induced by the refraction through a curved interface

A last effect has to be taken into account which is the fact that when passing through a curved interface or reflecting on a curved surface, the section of the pencil ray changes as pictured in Figure B.3. This is described by Deschamps [29]. There is the following relation between the two

sections S_1 and S_2 respectively before and after the refraction or reflection

$$S_2 = K_D S_1 \tag{B.8}$$

The divergence coefficient is expressed that way

$$K_D = \sqrt{\frac{r_1^e r_2^e}{(r_1^e + s)(r_2^e + s)}} \tag{B.9}$$

with r^e being the radii of curvature of the emerging (or reflected) wave and with s the distance between the location of the event to the observer. In the case of multiple events, s is the distance between the location of the considered event and the location of the next one. In a homogeneous medium it is readily seen that the classical attenuation in $1/r$ is found because the incident and emerging radii of curvature are identical. In the case of a curved interface between two media, these radii are not equal.

The calculation to obtain the radii of curvatures are detailed in Deschamps [29] and will not be presented here for conciseness.

B.2.3 Expression of the pressure

The practical computation of the pressure fluctuations is explained in details, among others, in Pathak *et al.* [61]. For one ray going from $\vec{\xi}_S$ to $\vec{x}_M$ passing by $\vec{x}_R$ where a refraction or a reflection happens, as illustrated respectively in Fig. B.4 and Fig. B.5, the pressure in $\vec{x}_M$ can be expressed in function of the pressure in $\vec{x}_R$ with,

$$\hat{p}'(\vec{x}_M;\omega) = \hat{p}'(\vec{x}_{R^-};\omega) K_D K_T \hat{\Phi}(\vec{x}_M, \vec{x}_{R^+};\omega) \tag{B.10}$$

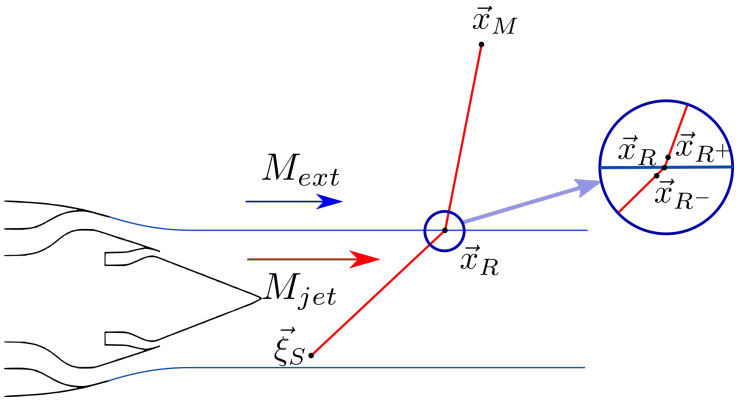

Figure B.4: Representation of a ray being refracted through the mixing layer

where $\vec{x}_{R^-}$ is a point on the wave path right before the interface between the two media and thus before the event and $\vec{x}_{R^+}$ is a point on the wave path right after the interface between the two media and thus after the event.

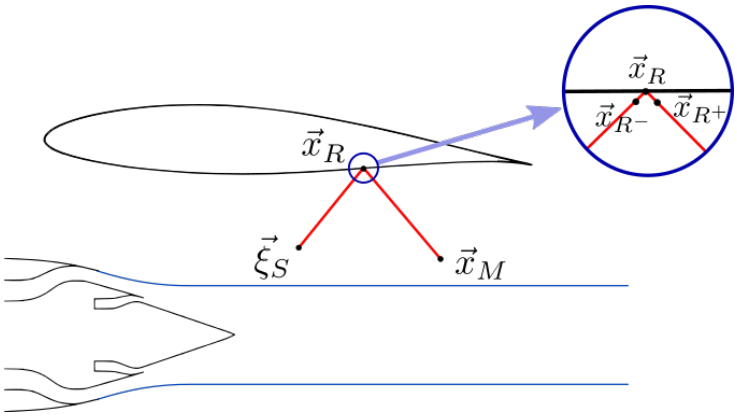

Figure B.5: Representation of a ray being reflected on a wing

$\hat{\Phi}$ is a phase jump expressed, in the case of a flow in the x direction, as

$$\hat{\Phi}(\vec{x}_M, \vec{x}_{R^+}; \omega) = e^{ik'\left[|\vec{x}'_M - \vec{x}'_{R^+}| + M_{\text{ext}}(\vec{x}'_{M,x} - \vec{x}'_{R^+,x})\right]} \tag{B.11}$$

with M_{ext} the Mach number of the medium in which the second part of the ray is located. The following change of variable, dependent on the Mach number of the medium in which the corresponding point is located, is introduced.

$$x = x'\sqrt{1 - M_{\text{ext}}^2} \tag{B.12}$$

$$y = y' \tag{B.13}$$

$$z = z' \tag{B.14}$$

$$k = k'\sqrt{1 - M_{\text{ext}}^2} \tag{B.15}$$

with $k = 2\pi/\lambda$ the wavenumber.

For one ray, the pressure can be written as

$$\hat{p}'(\vec{x}_M, \omega) = I(\vec{\xi}_S, \omega)\hat{G}(\vec{x}_M, \vec{\xi}_S; \omega) \tag{B.16}$$

with I the amplitude of the source and $\hat{G}$ the propagation function from the source to the observer taking into account all the changes induced by the events as shown in Eq (B.10). Once this is done for each ray, the pressure at the location of the observer is obtained with the summation of all the contribution of each ray.

B.2.4 Application of the ray theory: Practical case

A realistic case is taken in order to show the practical use of the ray theory. Let's consider the situation pictured in Fig. B.6 of three rays coming from two source points $\vec{\xi}_S$ and $\vec{\zeta}_S$ of respective

amplitude $I(\vec{\xi}_S, \omega)$ and $I(\vec{\zeta}_S, \omega)$. One ray is going out of the jet, impacting the wing and going through the jet before reaching the observer $\vec{x}_M$ while the others are exiting the jet and reaching $\vec{x}_M$.

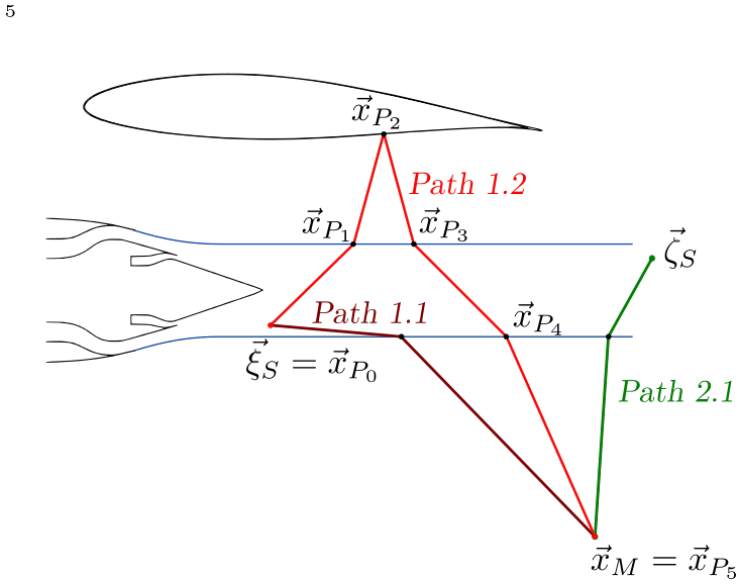

Figure B.6: Practical case of a ray with mutliple refractions and reflections

The pressure in $\vec{x}_M$ is expressed using Eq (B.16) giving the following formula

$$\hat{p}'(\vec{x}_M, \omega) = I(\vec{\xi}_S, \omega)\left(\hat{G}_{1.1}(\vec{x}_M, \vec{\xi}_S; \omega) + \hat{G}_{1.2}(\vec{x}_M, \vec{\xi}_S; \omega)\right) + I(\vec{\zeta}_S, \omega)\hat{G}_{2.1}(\vec{x}_M, \vec{\zeta}_S; \omega) \tag{B.17}$$

with $\hat{G}_n$ the propagation term for each path. As an illustration, this term for the path 1.2 will be explicited.

Using Eq (B.10) for each event

$$\hat{p}'(\vec{x}_M, \omega) = \hat{p}'(\vec{x}_{P_4^-}, \omega) K_D(\vec{x}_{P_4}) K_T(\vec{x}_{P_4}) \hat{\Phi}_{ext}(\vec{x}_M, \vec{x}_{P_4^+}, \omega) \tag{B.18}$$

$$\hat{p}'(\vec{x}_{P_4^-}, \omega) = \hat{p}'(\vec{x}_{P_3^-}, \omega) K_D(\vec{x}_{P_3}) K_T(\vec{x}_{P_3}) \hat{\Phi}_{ext}(\vec{x}_{P_4^-}, \vec{x}_{P_3^+}, \omega) \tag{B.19}$$

$$\hat{p}'(\vec{x}_{P_3^-}, \omega) = \hat{p}'(\vec{x}_{P_2^-}, \omega) K_D(\vec{x}_{P_2}) K_T(\vec{x}_{P_2}) \hat{\Phi}_{ext}(\vec{x}_{P_3^-}, \vec{x}_{P_2^+}, \omega) \tag{B.20}$$

$$\hat{p}'(\vec{x}_{P_2^-}, \omega) = \hat{p}'(\vec{x}_{P_1^-}, \omega) K_D(\vec{x}_{P_1}) K_T(\vec{x}_{P_1}) \hat{\Phi}_{ext}(\vec{x}_{P_2^-}, \vec{x}_{P_1^+}; \omega) \tag{B.21}$$

with $K_T(\vec{x}_{P_2}) = 1$ because in $\vec{x}_{P_2}$ there is a total reflection and not a refraction.

Let's introduce the following notation

$$\hat{K}(\vec{x}_{P_{n+1}}, \vec{x}_{P_n}; \omega) = K_D(\vec{x}_{P_n}) K_T(\vec{x}_{P_n}) \hat{\Phi}(\vec{x}_{P_{n+1}^-}, \vec{x}_{P_n^+}; \omega) \tag{B.22}$$

where K_D and K_T are calculated with the correct formula depending on the nature of the event.

$$\hat{p}'_{1.2}(\vec{x}_M,\omega) = \hat{p}'(\vec{x}_{P_4^-},\omega)\hat{K}(\vec{x}_M,\vec{x}_{P_4};\omega) \tag{B.23}$$

$$\hat{p}'(\vec{x}_{P_4^-},\omega) = \hat{p}'(\vec{x}_{P_3^-},\omega)\hat{K}(\vec{x}_{P_4},\vec{x}_{P_3};\omega) \tag{B.24}$$

$$\hat{p}'(\vec{x}_{P_3^-},\omega) = \hat{p}'(\vec{x}_{P_2^-},\omega)\hat{K}(\vec{x}_{P_3},\vec{x}_{P_2};\omega) \tag{B.25}$$

$$\hat{p}'(\vec{x}_{P_2^-},\omega) = \hat{p}'(\vec{x}_{P_1^-},\omega)\hat{K}(\vec{x}_{P_2},\vec{x}_{P_1};\omega) \tag{B.26}$$

leading to

$$\hat{p}'_{1.2}(\vec{x}_M,\omega) = \hat{p}'(\vec{x}_{P_1^-},\omega)\prod_{n=1}^{4}\hat{K}(\vec{x}_{P_{n+1}},\vec{x}_{P_n};\omega) \tag{B.27}$$

Finally, the last step is the propagation from $\vec{\xi}_S$ to $\vec{x}_{P_1^-}$, which is done with the convected Helmholtz equation. That gives, for a source amplitude in $\vec{\xi}_S$ noted $I(\vec{\xi}_S,\omega)$ and the solution to the CHE noted $\hat{G}(\vec{\xi}_S,\vec{x}_{P_1^-},\omega)$

$$\hat{p}'_{1.2}(\vec{x}_M,\omega) = I(\vec{\xi}_S,\omega)\hat{G}(\vec{\xi}_S,\vec{x}_{P_1^-};\omega)\prod_{n=1}^{4}\hat{K}(\vec{x}_{P_{n+1}},\vec{x}_{P_n};\omega) = I(\vec{\xi}_S,\omega)\hat{G}_{1.2}(\vec{x}_M,\vec{\xi}_S;\omega) \tag{B.28}$$

B.2.5 Formula in the general case

Now that a practical case has been presented, the formula in the general case can be deduced. Eq (B.16) can be written in the general case of N sources as

$$\hat{p}'(\vec{x}_M,\omega) = \sum_{n=1}^{N} I(\vec{\xi}_{S_n},\omega)\sum_{r=1}^{N_n}\hat{G}_r(\vec{x}_M,\vec{\xi}_{S_n};\omega) \tag{B.29}$$

where N_n is the number of rays starting from the source point $\vec{\xi}_{S_n}$ and reaching the observer $\vec{x}_M$.

By using a volume of sources and thus a volumic amplitude for each source it leads to the following integral formulation

$$\hat{p}'(\vec{x}_M,\omega) = \int_{\vec{\xi}_S} I(\vec{\xi}_S,\omega)\sum_{r=1}^{N(\vec{\xi}_S)}\hat{G}_r(\vec{x}_M,\vec{\xi}_S;\omega)\mathrm{d}\vec{\xi}_S \tag{B.30}$$

with the transfer function $\hat{G}$ being

$$\hat{G}(\vec{\xi}_S,\vec{x}_M,\omega) = \sum_{r=1}^{N(\vec{\xi}_S)}\hat{G}_r(\vec{x}_M,\vec{\xi}_S;\omega) \tag{B.31}$$

In the time domain, that makes

$$p'(\vec{x}_M,t) = \int_{\vec{\xi}_S}\int_{\omega}\int_{t_1} I(\vec{\xi}_S,\omega)\hat{G}(\vec{\xi}_S,\vec{x}_M;\omega)e^{-i\omega(t-t_1)}\mathrm{d}\vec{\xi}_S\mathrm{d}\omega\mathrm{d}t_1 \tag{B.32}$$

C Calculations

C.1 Model from Tam and Auriault - Integrations according to t_1, t_2 and ω_1

The integration of Eq (3.40) according to t_1, t_2 and ω_1 is performed.

$$\hat{S}(\vec{x}_M,\omega) = \int_{\omega_1}\int_{\vec{\xi}_S}\int_{\vec{\zeta}_S}\int_{t_1}\int_{t_2} \hat{p}^a(\vec{\xi}_S,\vec{x}_M;\omega_1)\hat{p}^a(\vec{\zeta}_S,\vec{x}_M;\omega)\frac{I_s^2}{\tau_s^2} \exp\left(-\frac{|\xi_x-\zeta_x|}{\bar{u}_x\tau_s} - \ln 2\left[\frac{[(\xi_x-\zeta_x)-\bar{u}_x(t_1-t_2)]^2}{l_s^2} + \frac{(\xi_y-\zeta_y)^2}{l_s^2} + \frac{(\xi_z-\zeta_z)^2}{l_s^2}\right]\right) e^{i\omega_1 t_1 + i\omega t_2}\mathrm{d}\omega_1\mathrm{d}\vec{\xi}_S\mathrm{d}\vec{\zeta}_S\mathrm{d}t_1\mathrm{d}t_2 \tag{C.1}$$

The integration according to t_1 and t_2 are first taken care of.

$$I = \int_{t_1}\int_{t_2} \exp\left(i\omega_1 t_1\right)\exp(i\omega t_2)\exp\left(-\frac{\ln 2}{l_s^2}[(\xi_x-\zeta_x)-\bar{u}_x(t_1-t_2)]^2\right)\mathrm{d}t_1\mathrm{d}t_2 \tag{C.2}$$

The following change of variable is done.

$$s = (t_1-t_2) - \frac{\xi_x-\zeta_x}{\bar{u}_x} \tag{C.3}$$

With s in place of t_1, I becomes

$$I = \int_s\int_{t_2} \exp\left(i\omega_1\left[s+t_2+\frac{\xi_x-\zeta_x}{\bar{u}_x}\right]\right)e^{i\omega t_2}\exp\left(-\frac{\ln 2}{l_s^2}(\bar{u}_x s)^2\right)\mathrm{d}s\mathrm{d}t_2 \tag{C.4}$$

The integrals can now be separated.

$$I = \exp\left(i\omega_1 \left[\frac{\xi_x - \zeta_x}{\bar{u}_x}\right]\right) \int_{t_2} e^{i(\omega+\omega_1)t_2} \mathrm{d}t_2 \int_s \exp\left(-\frac{\ln 2}{l_s^2}(\bar{u}_x s)^2 + i\omega_1 s\right) \mathrm{d}s \tag{C.5}$$

The integration according to t_2 is done using the Fourier transform of the Dirac function given in Eq (3.35). The simplified form of I is

$$I = 2\pi\delta(\omega_1 + \omega) \exp\left(i\omega_1 \left[\frac{\xi_x - \zeta_x}{\bar{u}_x}\right]\right) \int_{-\infty}^{\infty} \exp\left(-\frac{\ln 2}{l_s^2}(\bar{u}_x s)^2 + i\omega_1 s\right) \mathrm{d}s \tag{C.6}$$

The following manipulation is done to regroup the terms in s.

$$\begin{aligned} -\frac{\ln 2}{l_x^2}(\bar{u}_x s)^2 + i\omega_1 s &= -\frac{\ln 2}{l_s^2}\bar{u}_x^2 \left(s^2 - i\omega_1 s \frac{l_s^2}{\bar{u}_x^2 \ln 2}\right) \\ &= -\frac{\ln 2}{l_s^2}\bar{u}_x^2 \left(s - i\frac{\omega_1 l_s^2}{2\bar{u}_x^2 \ln 2}\right)^2 - \frac{1}{4}\frac{\omega_1^2 l_s^2}{\bar{u}_x^2 \ln 2} \end{aligned} \tag{C.7}$$

The following change of variable is done to highlight a Gaussian integral.

$$\tilde{s} = s - i\frac{\omega_1 l_s^2}{2\bar{u}_x^2 \ln 2} \tag{C.8}$$

With the new variable $\tilde{s}$, the integral becomes

$$I = 2\pi\delta(\omega_1 + \omega) \exp\left(i\omega_1 \left[\frac{\xi_x - \zeta_x}{\bar{u}_x}\right] - \frac{1}{4}\frac{\omega_1^2 l_s^2}{\bar{u}_x^2 \ln 2}\right) \int_{-\infty}^{\infty} \exp\left(-\frac{\ln 2}{l_s^2}\bar{u}_x^2 \tilde{s}^2\right) \mathrm{d}\tilde{s} \tag{C.9}$$

The value of a Gaussian integral is given by the following property

$$\int_{-\infty}^{\infty} \exp^{-ax^2} \mathrm{d}x = \sqrt{\frac{\pi}{a}} \tag{C.10}$$

which gives

$$I = 2\pi\delta(\omega_1 + \omega) \exp\left(i\omega_1 \left[\frac{\xi_x - \zeta_x}{\bar{u}_x}\right] - \frac{1}{4}\frac{\omega_1 l_s^2}{\bar{u}_x^2 \ln 2}\right) \sqrt{\frac{\pi l_s^2}{\bar{u}_x^2 \ln 2}} \tag{C.11}$$

$$I = 2\pi \left(\frac{\pi}{\ln 2}\right)^{1/2} \delta(\omega_1 + \omega) \exp\left(i\omega_1 \left[\frac{\xi_x - \zeta_x}{\bar{u}_x}\right] - \frac{1}{4}\frac{\omega_1 l_s^2}{\bar{u}_x^2 \ln 2}\right) \frac{l_s}{\bar{u}_x} \tag{C.12}$$

So, by setting this into Eq (3.40) it follows

$$\hat{S}(\vec{x}_M,\omega) = 2\pi\left(\frac{\pi}{\ln 2}\right)^{1/2}\int_{\omega_1}\int_{\vec{\xi}_S}\int_{\vec{\zeta}_S}\hat{p}^a(\vec{\xi}_S,\vec{x}_M;\omega_1)\hat{p}^a(\vec{\zeta}_S,\vec{x}_M;\omega)\frac{I_s^2 l_s}{\bar{u}_x\tau_s^2}$$
$$\exp\left[-\frac{\omega_1^2 l_s^2}{(4\ln 2)\bar{u}_x^2}-\frac{|\xi_x-\zeta_x|}{\bar{u}_x\tau_s}\right]$$
$$\exp\left[-\ln 2\left[\frac{(\xi_y-\zeta_y)^2}{l_s^2}+\frac{(\xi_z-\zeta_z)^2}{l_s^2}\right]+\frac{i\omega_1(\xi_x-\zeta_x)}{\bar{u}_x}\right]$$
$$\delta(\omega_1+\omega)\mathrm{d}\omega_1\mathrm{d}\vec{\xi}_S\mathrm{d}\vec{\zeta}_S \tag{C.13}$$

The integration according to ω_1 is straightforward, giving

$$\hat{S}(\vec{x}_M,\omega) = 2\pi\left(\frac{\pi}{\ln 2}\right)^{1/2}\int_{\vec{\xi}_S}\int_{\vec{\zeta}_S}\frac{I_s^2 l_s}{\tau_s^2\bar{u}_x}\hat{p}^a(\vec{\xi}_S,\vec{x}_M;-\omega)\hat{p}^a(\vec{\zeta}_S,\vec{x}_M;\omega)$$
$$\exp\left[-\frac{\omega^2 l_s^2}{(4\ln 2)\bar{u}_x^2}-\frac{|\xi_x-\zeta_x|}{\bar{u}_x\tau_s}\right]$$
$$\exp\left[-\ln 2\left[\frac{(\xi_y-\zeta_y)^2}{l_s^2}+\frac{(\xi_z-\zeta_z)^2}{l_s^2}\right]-\frac{i\omega(\xi_x-\zeta_x)}{\bar{u}_x}\right]\mathrm{d}\vec{\xi}_S\mathrm{d}\vec{\zeta}_S \tag{C.14}$$

C.2 Model from Tam and Auriault - Integration according to $\vec{\xi}_S$

The integration of Eq (3.48) according to $\vec{\xi}_S$ needs to be taken care of.

$$\hat{S}(\vec{x}_M,\omega) = 2\pi\left(\frac{\pi}{\ln 2}\right)^{1/2}\int_{\vec{\xi}_S}\int_{\vec{\zeta}_S}\frac{I_s^2 l_s}{\tau_s^2\bar{u}_x}|\hat{p}^a(\vec{\zeta},\vec{x}_M;\omega)|^2\exp\left[i\frac{\omega}{c_{ext}}\cos\theta(\xi_x-\zeta_x)\right]$$
$$\exp\left[-\frac{\omega^2 l_s^2}{(4\ln 2)\bar{u}_x^2}-\frac{|\xi_x-\zeta_x|}{\bar{u}_x\tau_s}\right]$$
$$\exp\left[-\ln 2\left[\frac{(\xi_y-\zeta_y)^2}{l_s^2}+\frac{(\xi_z-\zeta_z)^2}{l_s^2}\right]-\frac{i\omega(\xi_x-\zeta_x)}{\bar{u}_x}\right]\mathrm{d}\vec{\xi}_S\mathrm{d}\vec{\zeta}_S \tag{C.15}$$

Three variable changes on the coordinates of $\vec{\xi}_S$ are done $X=\xi_x-\zeta_x$, $Y=\xi_y-\zeta_y$, $Z=\xi_z-\zeta_z$. The terms in Y and Z are isolated and taken care of first.

$$I = \int_Y \int_Z \exp\left(- \ln 2 \left[\frac{Y^2}{l_s^2} + \frac{Z^2}{l_s^2} \right] \right) \mathrm{d}Y \mathrm{d}Z \tag{C.16}$$

The value of a Gaussian integral is given by the following property

$$\int_{-\infty}^{\infty} \exp^{-ax^2} \mathrm{d}x = \sqrt{\frac{\pi}{a}} \tag{C.17}$$

The integration according to Y and Z are then done.

$$I = l_s^2 \frac{\pi}{\ln 2} \tag{C.18}$$

For the integration according to X, a separation between positive and negative values is first done, giving

$$I = \int_{-\infty}^{\infty} \exp\left(-\frac{|X|}{\bar{u}_x \tau_s} - \frac{i\omega X}{\bar{u}_x} \left(1 - \frac{\bar{u}_x}{c_{ext}} \cos\theta \right) \right) \mathrm{d}X \tag{C.19}$$

$$\begin{aligned} I = &\int_0^{\infty} \exp\left(\left[-\frac{1}{\bar{u}_x \tau_s} - \frac{i\omega}{\bar{u}_x} \left(1 - \frac{\bar{u}_x}{c_{ext}} \cos\theta \right) \right] X \right) \mathrm{d}X \\ &+ \int_{-\infty}^{0} \exp\left(\left[\frac{1}{\bar{u}_x \tau_s} - \frac{i\omega}{\bar{u}_x} \left(1 - \frac{\bar{u}_x}{c_{ext}} \cos\theta \right) \right] X \right) \mathrm{d}X \end{aligned} \tag{C.20}$$

The integration of the exponential is done for both integrals.

$$\begin{aligned} I = &\frac{-1}{\frac{1}{\bar{u}_x \tau_s} + \frac{i\omega}{\bar{u}_x} \left(1 - \frac{\bar{u}_x}{c_{ext}} \cos\theta \right)} \left[\exp\left(\left[-\frac{1}{\bar{u}_x \tau_s} - \frac{i\omega}{\bar{u}_x} \left(1 - \frac{\bar{u}_x}{c_{ext}} \cos\theta \right) \right] X \right) \right]_0^{\infty} \\ &+ \frac{1}{\frac{1}{\bar{u}_x \tau_s} - \frac{i\omega}{\bar{u}_x} \left(1 - \frac{\bar{u}_x}{c_{ext}} \cos\theta \right)} \left[\exp\left(\left[\frac{1}{\bar{u}_x \tau_s} - \frac{i\omega}{\bar{u}_x} \left(1 - \frac{\bar{u}_x}{c_{ext}} \cos\theta \right) \right] X \right) \right]_{-\infty}^{0} \end{aligned} \tag{C.21}$$

There is

$$\left| \exp\left(\frac{-i\omega}{\bar{u}_x} \left(1 - \frac{\bar{u}_x}{c_{ext}} \cos\theta \right) X \right) \right| = 1 \tag{C.22}$$

and

$$\lim_{X\to\infty} \exp\left(-\frac{1}{\bar{u}_x \tau_s} X \right) = 0 \tag{C.23}$$

The primitive in ∞ is obtained using the following limit value.

$$\lim_{X\to\infty} \exp\left(-\frac{1}{\bar{u}_x \tau_s} X \right) \exp\left(\frac{-i\omega}{\bar{u}_x} \left(1 - \frac{\bar{u}_x}{c_{ext}} \cos\theta \right) X \right) = 0 \tag{C.24}$$

and subsequently

$$\lim_{X\to-\infty} -\exp\left(\frac{1}{\bar{u}_x \tau_s} X \right) \exp\left(\frac{-i\omega}{\bar{u}_x} \left(1 - \frac{\bar{u}_x}{c_{ext}} \cos\theta \right) X \right) = 0 \tag{C.25}$$

The value of I is finally obtained with

$$\begin{aligned} I =& \frac{1}{\frac{1}{\bar{u}_x \tau_s} + \frac{i\omega}{\bar{u}_x} \left(1 - \frac{\bar{u}_x}{c_{ext}} \cos\theta \right)} + \frac{1}{\frac{1}{\bar{u}_x \tau_s} - \frac{i\omega}{\bar{u}_x} \left(1 - \frac{\bar{u}_x}{c_{ext}} \cos\theta \right)} \\ =& \frac{\frac{2}{\bar{u}_x \tau_s}}{\frac{1}{\bar{u}_x^2 \tau_s^2} + \frac{\omega^2}{\bar{u}_x^2} \left(1 - \frac{\bar{u}_x}{c_{ext}} \cos\theta \right)^2} \end{aligned} \tag{C.26}$$

$$I = \frac{2\bar{u}_x \tau_s}{1 + \omega^2 \tau_s^2 \left(1 - \frac{\bar{u}_x}{c_{ext}} \cos\theta \right)^2} \tag{C.27}$$

The spatial integration according to $\vec{\xi}_S$ is done and Eq (3.48) can now be written in this final form

$$\hat{S}(\vec{x}_M,\omega) = 4\pi\left(\frac{\pi}{\ln 2}\right)^{3/2}\int_{\vec{\zeta}_S}\frac{I_s^2 l_s^3}{\tau_s}|\hat{p}^a(\vec{\zeta}_S,\vec{x}_M;\omega)|^2\frac{\exp\left[-\dfrac{\omega^2 l_s^2}{4\ln 2\bar{u}_x^2}\right]}{1+\left(1-\dfrac{\bar{u}_x}{c_{ext}}\cos\theta\right)^2\omega^2\tau_s^2}\mathrm{d}\vec{\zeta}_S \tag{C.28}$$

C.3 Sound propagation using geometrical acoustics - Integration according to $\vec{\xi}_S$

The integration of Eq (3.83) according to $\vec{\xi}_S$ needs to be taken care of.

$$\begin{aligned}\hat{S}(\vec{x}_M,\omega) =& 2\pi\left(\frac{\pi}{\ln 2}\right)^{1/2}\int_{\vec{\xi}_S}\int_{\vec{\zeta}_S}\frac{I_s^2 l_x}{\tau_s^2\bar{u}_x}|\hat{p}^a(\vec{\zeta},\vec{x}_M;\omega)|^2\\ &\exp\left[i\frac{\omega}{c_{ext}}\left(\cos\theta(\xi_x-\zeta_x)+\sin\theta\cos\phi(\xi_y-\zeta_y)+\sin\theta\sin\phi(\xi_z-\zeta_z)\right)\right]\\ &\exp\left[-\frac{\omega^2 l_x^2}{(4\ln 2)\bar{u}_x^2}-\frac{|\xi_x-\zeta_x|}{\bar{u}_x\tau_s}\right]\\ &\exp\left[-\ln 2\left[\frac{(\xi_y-\zeta_y)^2}{l_y^2}+\frac{(\xi_z-\zeta_z)^2}{l_z^2}\right]-\frac{i\omega(\xi_x-\zeta_x)}{\bar{u}_x}\right]\mathrm{d}\vec{\xi}_S\mathrm{d}\vec{\zeta}_S\end{aligned} \tag{C.29}$$

Three variable changes on the coordinates of $\vec{\xi}_S$ are done $X=\xi_x-\zeta_x$, $Y=\xi_y-\zeta_y$, $Z=\xi_z-\zeta_z$. The terms in Y and Z are isolated and taken care of first.

$$I=\int_Y\int_Z\exp\left(-\ln 2\left[\frac{Y^2}{l_y^2}+\frac{Z^2}{l_z^2}\right]\right)\exp\left(-i\frac{\omega}{c_{ext}}[Y\sin\theta\cos\phi+Z\sin\theta\sin\phi]\right)\mathrm{d}Y\mathrm{d}Z \tag{C.30}$$

The following manipulation is done to regroup the terms in Y.

$$-\frac{\ln 2}{l_y^2}Y^2-i\frac{\omega}{c_{ext}}Y\sin\theta\cos\phi=-\frac{\ln 2}{l_y^2}\left(Y-i\frac{\omega l_y^2\sin\theta\cos\phi}{2c_{ext}\ln 2}\right)^2-\frac{\omega^2 l_y^2\sin^2\theta\cos^2\phi}{4c_{ext}^2\ln 2} \tag{C.31}$$

The change of variable $\tilde{Y}=Y-\dfrac{i\omega l_y^2}{2c_{ext}\ln 2}\sin\theta\cos\phi$ is done to highlight a Gaussian integral.

In the same way $\tilde{Z} = Z - \dfrac{i\omega l_z^2}{2c_{ext}\ln 2}\sin\theta\sin\phi$. That gives the following updated form for I.

$$I = \int_{\tilde{Y}}\int_{\tilde{Z}} \exp\left(-\ln 2\left[\frac{\tilde{Y}^2}{l_y^2} + \frac{\tilde{Z}^2}{l_z^2}\right]\right) \exp\left(-\frac{\omega^2}{4c_{ext}^2\ln 2}\left[l_y^2\sin^2\theta\cos^2\phi + l_z^2\sin^2\theta\sin^2\phi\right]\right) \mathrm{d}\tilde{Y}\mathrm{d}\tilde{Z} \tag{C.32}$$

The value of a Gaussian integral is given by the following property

$$\int_{-\infty}^{\infty} \exp^{-ax^2}\,\mathrm{d}x = \sqrt{\frac{\pi}{a}} \tag{C.33}$$

The integration according to $\tilde{Y}$ and $\tilde{Z}$ are then done.

$$I = l_y l_z \frac{\pi}{\ln 2}\exp\left(-\frac{\omega^2}{4c_{ext}^2\ln 2}\left[l_y^2\sin^2\theta\cos^2\phi + l_z^2\sin^2\theta\sin^2\phi\right]\right) \tag{C.34}$$

For the integration according to X, a separation between positive and negative values is first done, giving

$$I = \int_{-\infty}^{\infty} \exp\left(-\frac{|X|}{\bar{u}_x\tau_s} - \frac{i\omega X}{\bar{u}_x}\left(1 - \frac{\bar{u}_x}{c_{ext}}\cos\theta\right)\right)\mathrm{d}X \tag{C.35}$$

$$\begin{aligned} I = &\int_0^{\infty} \exp\left(\left[-\frac{1}{\bar{u}_x\tau_s} - \frac{i\omega}{\bar{u}_x}\left(1 - \frac{\bar{u}_x}{c_{ext}}\cos\theta\right)\right]X\right)\mathrm{d}X \\ &+ \int_{-\infty}^{0} \exp\left(\left[\frac{1}{\bar{u}_x\tau_s} - \frac{i\omega}{\bar{u}_x}\left(1 - \frac{\bar{u}_x}{c_{ext}}\cos\theta\right)\right]X\right)\mathrm{d}X \end{aligned} \tag{C.36}$$

The integration of the exponential is done for both integrals.

$$\begin{aligned} I = &\frac{-1}{\dfrac{1}{\bar{u}_x\tau_s} + \dfrac{i\omega}{\bar{u}_x}\left(1 - \dfrac{\bar{u}_x}{c_{ext}}\cos\theta\right)}\left[\exp\left(\left[-\frac{1}{\bar{u}_x\tau_s} - \frac{i\omega}{\bar{u}_x}\left(1 - \frac{\bar{u}_x}{c_{ext}}\cos\theta\right)\right]X\right)\right]_0^{\infty} \\ &+ \frac{1}{\dfrac{1}{\bar{u}_x\tau_s} - \dfrac{i\omega}{\bar{u}_x}\left(1 - \dfrac{\bar{u}_x}{c_{ext}}\cos\theta\right)}\left[\exp\left(\left[\frac{1}{\bar{u}_x\tau_s} - \frac{i\omega}{\bar{u}_x}\left(1 - \frac{\bar{u}_x}{c_{ext}}\cos\theta\right)\right]X\right)\right]_{-\infty}^{0} \end{aligned} \tag{C.37}$$

There is

$$\left| \exp\left(\frac{-i\omega}{\bar{u}_x} \left(1 - \frac{\bar{u}_x}{c_{ext}} \cos\theta \right) X \right) \right| = 1 \tag{C.38}$$

and

$$\lim_{X \to \infty} \exp\left(-\frac{1}{\bar{u}_x \tau_s} X \right) = 0 \tag{C.39}$$

The primitive in ∞ is obtained using the following limit value.

$$\lim_{X \to \infty} \exp\left(-\frac{1}{\bar{u}_x \tau_s} X \right) \exp\left(\frac{-i\omega}{\bar{u}_x} \left(1 - \frac{\bar{u}_x}{c_{ext}} \cos\theta \right) X \right) = 0 \tag{C.40}$$

and subsequently

$$\lim_{X \to -\infty} -\exp\left(\frac{1}{\bar{u}_x \tau_s} X \right) \exp\left(\frac{-i\omega}{\bar{u}_x} \left(1 - \frac{\bar{u}_x}{c_{ext}} \cos\theta \right) X \right) = 0 \tag{C.41}$$

The value of I is finally obtained with

$$\begin{aligned} I =& \frac{1}{\frac{1}{\bar{u}_x \tau_s} + \frac{i\omega}{\bar{u}_x} \left(1 - \frac{\bar{u}_x}{c_{ext}} \cos\theta \right)} + \frac{1}{\frac{1}{\bar{u}_x \tau_s} - \frac{i\omega}{\bar{u}_x} \left(1 - \frac{\bar{u}_x}{c_{ext}} \cos\theta \right)} \\ =& \frac{\frac{2}{\bar{u}_x \tau_s}}{\frac{1}{\bar{u}_x^2 \tau_s^2} + \frac{\omega^2}{\bar{u}_x^2} \left(1 - \frac{\bar{u}_x}{c_{ext}} \cos\theta \right)^2} \end{aligned} \tag{C.42}$$

$$I = \frac{2\bar{u}_x \tau_s}{1 + \omega^2 \tau_s^2 \left(1 - \frac{\bar{u}_x}{c_{ext}} \cos\theta \right)^2} \tag{C.43}$$

The spatial integration according to $\vec{\xi}_S$ is done and Eq (3.83) is finally recast as

$$\hat{S}(\vec{x}_M,\omega) = 4\pi \left(\frac{\pi}{\ln 2}\right)^{3/2} \int_{\vec{\zeta}_S} \frac{I_s^2 l_x l_y l_z}{\tau_s} |\hat{p}^a(\vec{\zeta}_S,\vec{x}_M;\omega)|^2 \frac{\exp\left[-\frac{\omega^2}{4\ln 2\bar{u}_x^2}\left(l_x^2 + \frac{\bar{u}_x^2}{c_{ext}^2}[l_y^2\sin^2\theta\cos^2\phi + l_z^2\sin^2\theta\sin^2\phi]\right)\right]}{1+\left(1-\frac{\bar{u}_x}{c_{ext}}\cos\theta\right)^2 \omega^2\tau_s^2} \mathrm{d}\vec{\zeta}_S \tag{C.44}$$

D Results

D.1 Analysis of the RANS computations

The hotwire measurements [17] are compared to the value given by the RANS computations.

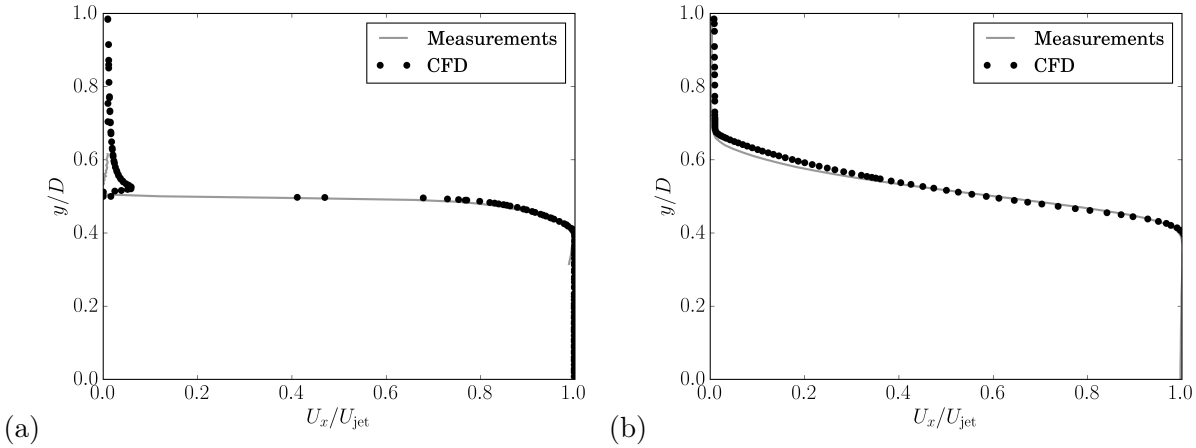

Figure D.1: Comparisons of the axial mean velocity from the measurements and the RANS computations at (a) $x = 0\,D$ (b) $x = 1\,D$.

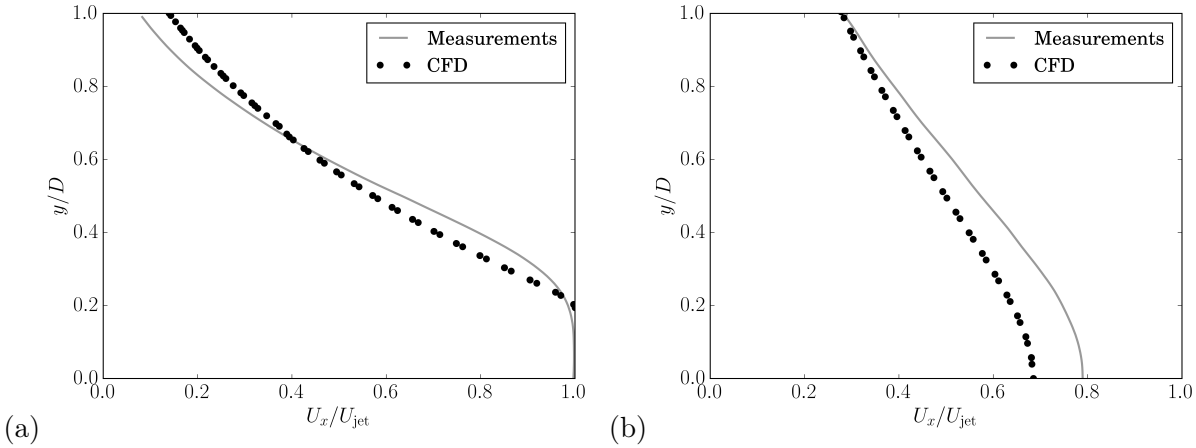

Figure D.2: Comparisons of the axial mean velocity from the measurements and the RANS computations at (a) $x = 5\,D$ (b) $x = 10\,D$.

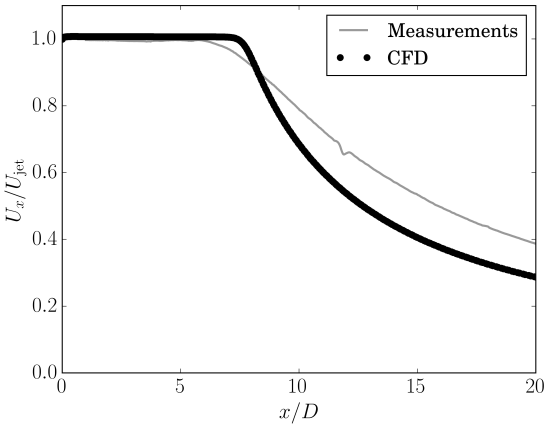

(a)

Figure D.3: Comparisons of the axial mean velocity from the measurements and the RANS computations alonxg the x axis.

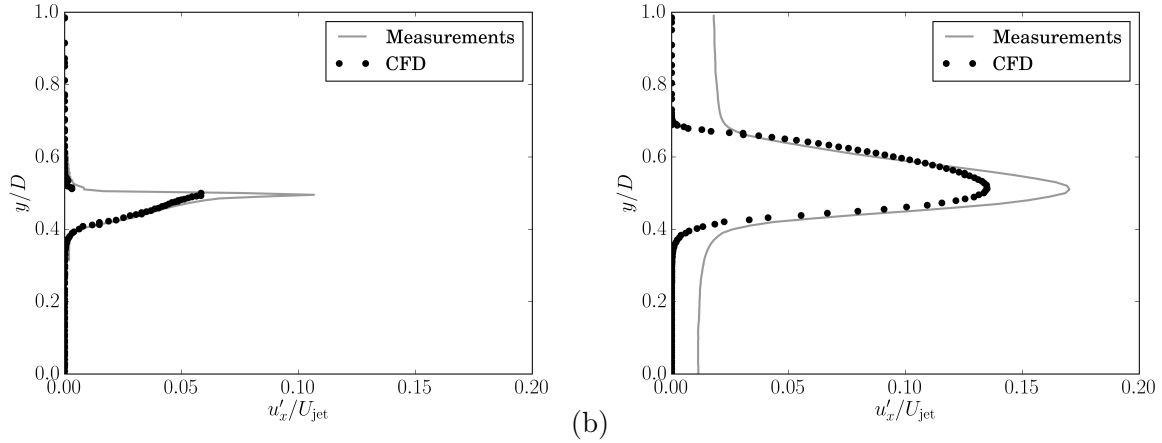

(a) (b)

Figure D.4: Comparisons of the axial fluctuating velocity from the measurements and the RANS computations at (a) $x = 0\,D$ (b) $x = 1\,D$.

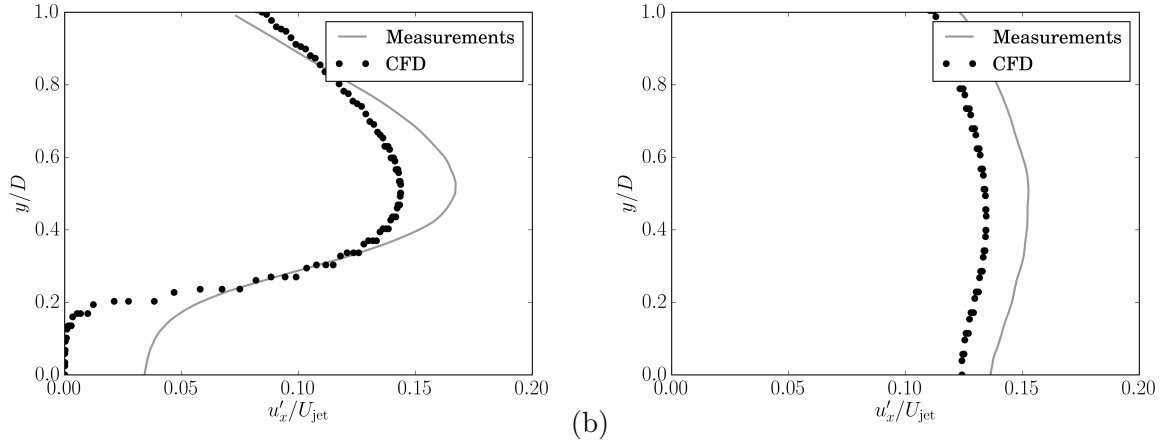

(a) (b)

Figure D.5: Comparisons of the axial fluctuating velocity from the measurements and the RANS computations at (a) $x = 5\,D$ (b) $x = 10\,D$.

There is a good agreement between the value provided by the RANS computation and the measurements for both the mean and fluctuating velocities.

D.2 Noise predictions on the single nozzle

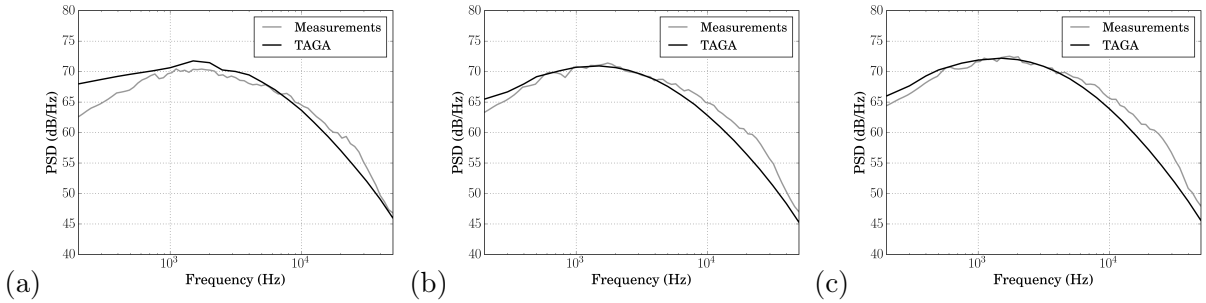

Figure D.6: Comparison of the PSD in the installed configuration at $M = 0.9$ for an observer at $\phi = 280°$ and (a) $\theta = 90°$, (b) $\theta = 100°$, and (c) $\theta = 110°$

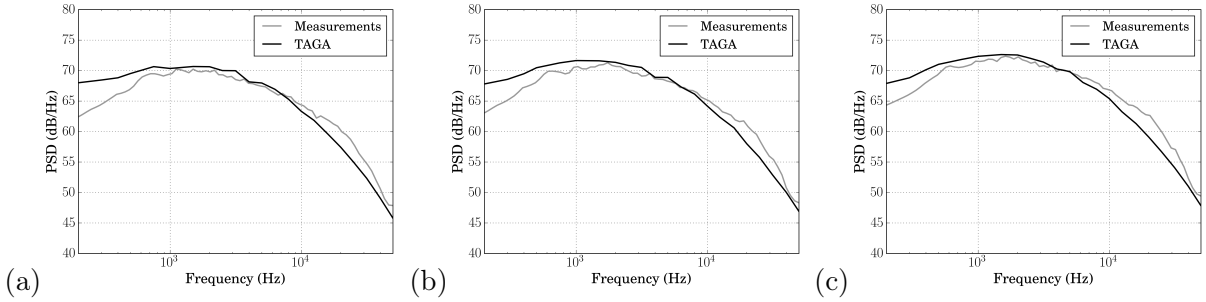

Figure D.7: Comparison of the PSD in the installed configuration at $M = 0.9$ for an observer at $\phi = 300°$ and (a) $\theta = 90°$, (b) $\theta = 100°$, and (c) $\theta = 110°$

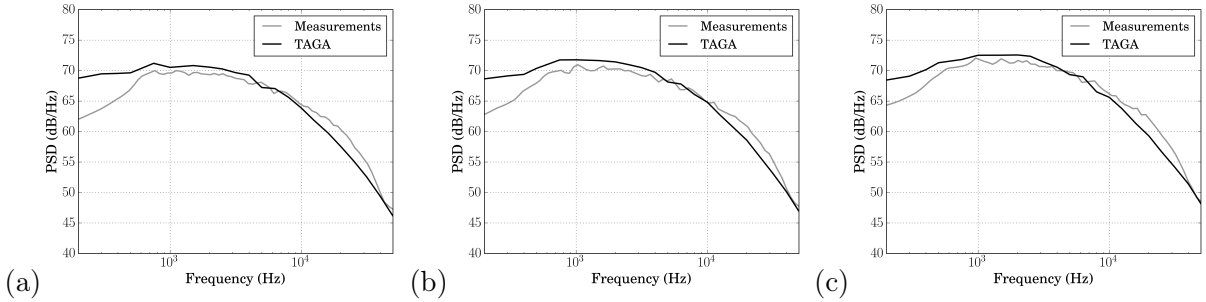

Figure D.8: Comparison of the PSD in the installed configuration at $M = 0.9$ for an observer at $\phi = 320°$ and (a) $\theta = 90°$, (b) $\theta = 100°$, and (c) $\theta = 110°$

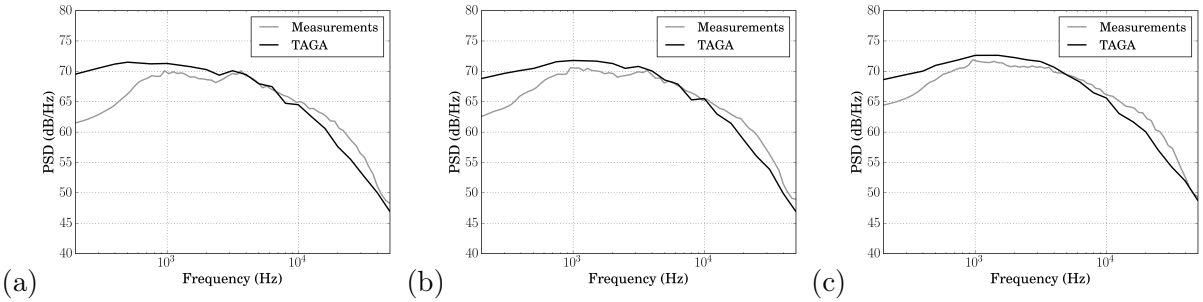

Figure D.9: Comparison of the PSD in the installed configuration at $M = 0.9$ for an observer at $\phi = 340°$ and (a) $\theta = 90°$, (b) $\theta = 100°$, and (c) $\theta = 110°$

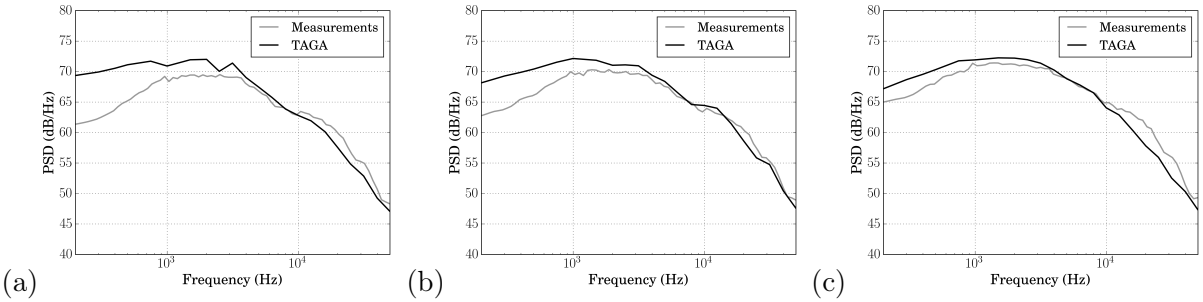

Figure D.10: Comparison of the PSD in the installed configuration at $M = 0.9$ for an observer at $\phi = 360°$ and (a) $\theta = 90°$, (b) $\theta = 100°$, and (c) $\theta = 110°$

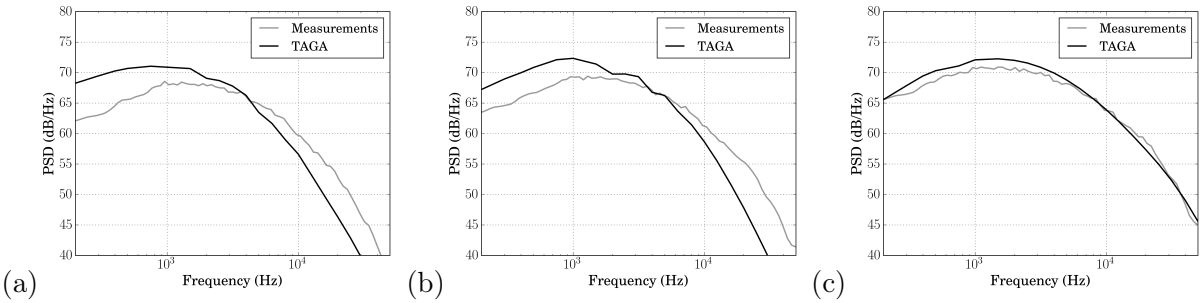

Figure D.11: Comparison of the PSD in the installed configuration at $M = 0.9$ for an observer at $\phi = 20°$ and (a) $\theta = 90°$, (b) $\theta = 100°$, and (c) $\theta = 110°$

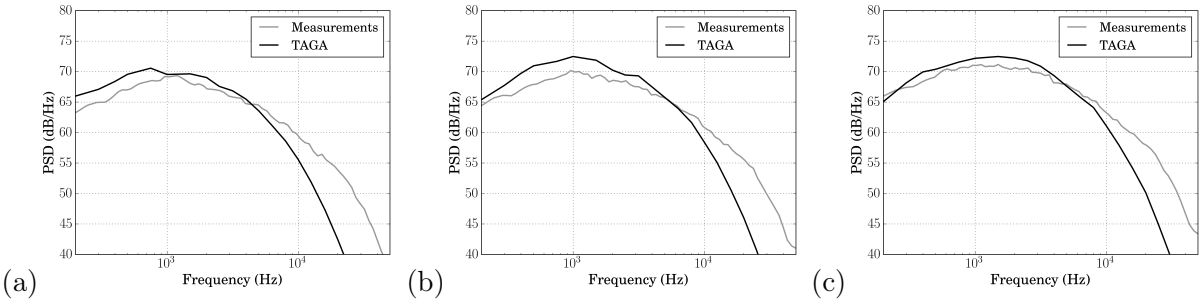

Figure D.12: Comparison of the PSD in the installed configuration at $M = 0.9$ for an observer at $\phi = 40°$ and (a) $\theta = 90°$, (b) $\theta = 100°$, and (c) $\theta = 110°$

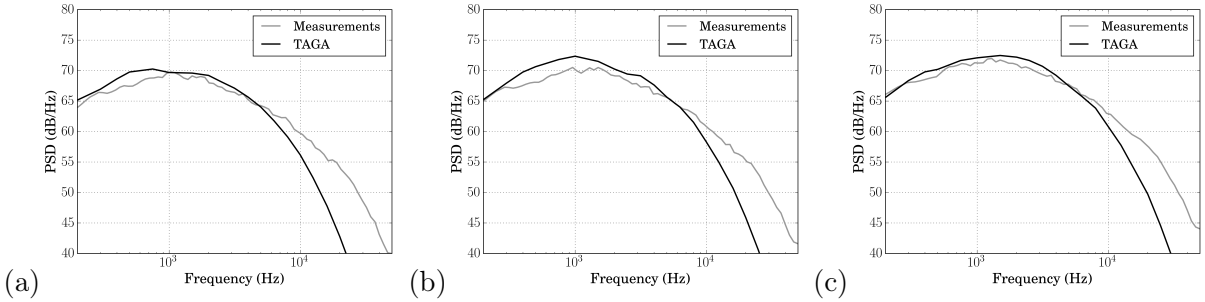

Figure D.13: Comparison of the PSD in the installed configuration at $M = 0.9$ for an observer at $\phi = 60°$ and (a) $\theta = 90°$, (b) $\theta = 100°$, and (c) $\theta = 110°$

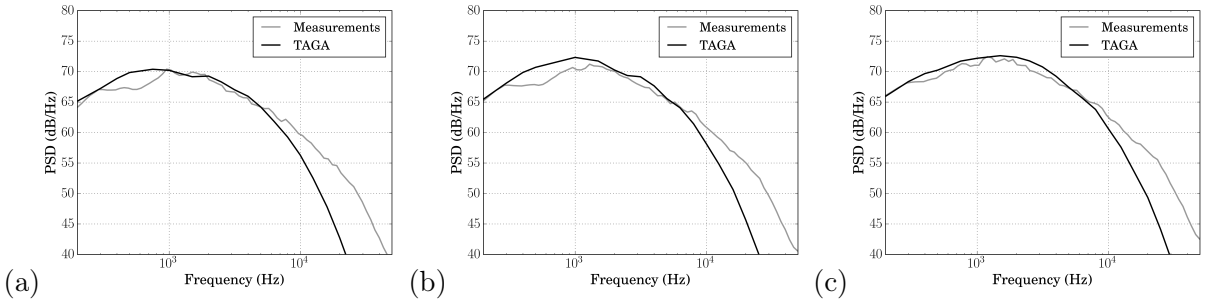

Figure D.14: Comparison of the PSD in the installed configuration at $M = 0.9$ for an observer at $\phi = 80°$ and (a) $\theta = 90°$, (b) $\theta = 100°$, and (c) $\theta = 110°$

Bibliography

[1] (2017). French trademark N.134009261.

[2] Amiet, R. K. (1978). Refraction of sound by a shear layer. *Journal of Sound and Vibration*, 58(4):467–482.

[3] Antares Development Team (2012–2020). Antares Documentation Release 1.15.0.

[4] Azarpeyvand, M. and Self, R. H. (2009). Improved jet noise modeling using a new time-scale. *The Journal of the Acoustical Society of America*, 126(3):1015–1025.

[5] Bailly, C., Bogey, C., and Candel, S. M. (2010). Modelling of sound generation by turbulent reacting flows. *International Journal of Aeroacoustics*, 9(4-5):461–489.

[6] Bailly, C. and Juve, D. (1999). A stochastic approach to compute subsonic noise using linearized Euler's equations. In *5th AIAA/CEAS Aeroacoustics Conference and Exhibit*, page 1872.

[7] Bailly, C., Lafon, P., and Candel, S. (1994). Computation of subsonic and supersonic jet mixing noise using a modified k-ϵ model for compressible free shear flows. *Acta Acustica*, 2(2):101–112.

[8] Balsa, T. F. (1976). The far field of high frequency convected singularities in sheared flows, with an application to jet-noise prediction. *Journal of Fluid Mechanics*, 74(2):193–208.

[9] Balsa, T. F. (1977). The acoustic field of sources in shear flow with application to jet noise: convective amplification. *Journal of Fluid Mechanics*, 79(1):33–47.

[10] Balsa, T. F. and Gliebe, P. R. (1977). Aerodynamics and noise of coaxial jets. *AIAA Journal*, 15(11):1550–1558.

[11] Batchelor, G. K. (1953). *The Theory of Homogeneous Turbulence*. Cambridge Science Classics. Cambridge University Press.

[12] Bechara, W., Bailly, C., Lafon, P., and Candel, S. M. (1994). Stochastic approach to noise modeling for free turbulent flows. *AIAA Journal*, 32(3):455–463.

[13] Blokhintzev, D. (1946). The propagation of sound in an inhomogeneous and moving medium I. *The Journal of the Acoustical Society of America*, 18(2):322–328.

[14] Bodard, G., Bailly, C., and Vuillot, F. (2009). Matched hybrid approaches to predict jet noise by using large eddy simulation. In *15th AIAA/CEAS Aeroacoustics Conference (30th AIAA Aeroacoustics Conference)*.

[15] Bogey, C. and Marsden, O. (2016). Simulations of initially highly disturbed jets with experiment-like exit boundary layers. *AIAA Journal*, 54(2):1299–1312.

[16] Brenner, P. (1991). Three-dimensional aerodynamics with moving bodies applied to solid propellant. In *27th Joint Propulsion Conference*, page 2304.

[17] Brès, G. A., Jordan, P., Jaunet, V., Le Rallic, M., Cavalieri, A. V., Towne, A., Lele, S. K., Colonius, T., and Schmidt, O. T. (2018). Importance of the nozzle-exit boundary-layer state in subsonic turbulent jets. *Journal of Fluid Mechanics*, 851:83–124.

[18] Bridges, J. and Brown, C. (2004). Parametric testing of chevrons on single flow hot jets. In *10th AIAA/CEAS Aeroacoustics Conference*, page 2824.

[19] Bridges, J. and Wernet, M. (2003). Measurements of aeroacoustic sound sources in turbulent jets. In *9th AIAA/CEAS Aeroacoustics Conference and Exhibit*, page 3130.

[20] Brouwer, H. H. and Nijboer, R. J. (2005). Computation of fine-scale turbulence jet noise. NLR-CR-2005-053, NLR.

[21] Callender, B., Gutmark, E. J., and Martens, S. (2005). Far-field acoustic investigation into chevron nozzle mechanisms and trends. *AIAA journal*, 43(1):87–95.

[22] Candel, S. M. (1977). Numerical solution of conservation equations arising in linear wave theory: application to aeroacoustics. *Journal of Fluid Mechanics*, 83(3):465–493.

[23] Candel, S. M. (1983). Sound source radiation in two-dimensional shear flow. *AIAA Journal*, 21(2):221–227.

[24] CFM (2004). Aircraft engine noise. Rome Aeronautical Engineering University.

[25] Chandrasekhar, S. (1950). The theory of axisymmetric turbulence. *Philosophical Transactions of the Royal Society of London. Series A, Mathematical and Physical Sciences*, 242(855):557–577.

[26] Darecki, M., Edelstenne, C., Enders, T., Fernandez, E., Hartman, P., Herteman, J.-P., Kerkloh, M., King, I., Ky, P., Mathieu, M., Orsi, G., Schotman, G., Smith, C., and Wörner, J.-D. (2011). Flightpath 2050 europes vision for aviation. *Off. Eur.*

[27] Davies, P. O. A. L., Fisher, M. J., and Barratt, M. J. (1962). The characteristics of the turbulence in the mixing region of a round jet. *Journal of Fluid Mechanics*, 15(3):337–367.

[28] Depuru Mohan, N. K., Dowling, A. P., Karabasov, S. A., Xia, H., Graham, O., Hynes, T. P., and Tucker, P. G. (2015). Acoustic sources and far-field noise of chevron and round jets. *AIAA Journal*, 53(9):2421–2436.

[29] Deschamps, G. A. (1972). Ray techniques in electromagnetics. *Proceedings of the IEEE*, 60(9):1022–1035.

[30] Dickson, N. (2013). ICAO noise standards. In *ICAO Symposium on Aviation and Climate Change*, volume 202.

[31] Doty, M. and McLaughlin, D. (2002). Two-point correlations of density gradient fluctuations in high speed jets using optical deflectometry. In *40th AIAA Aerospace Sciences Meeting & Exhibit*, page 367.

[32] Favre, A. (1965). Equations des gaz turbulents compressibles. *Journal de Mécanique*, 3:361–390.

[33] Fleury, C., Bailly, C., Jondeau, E., Michard, M., and Juvé, D. (2008). Space-time correlations in two subsonic jets using dual particle image velocimetry measurements. *AIAA Journal*, 46(10):2498–2509.

[34] Freund, J. B. (2001). Noise sources in a low-reynolds-number turbulent jet at mach 0.9. *Journal of Fluid Mechanics*, 438:277–305.

[35] Goldstein, M. E. (1976). Aeroacoustics. *New York, McGraw-Hill International Book Co., 1976. 305 p.*

[36] Goldstein, M. E. and Leib, S. J. (2008). The aeroacoustics of slowly diverging supersonic jets. *Journal of Fluid Mechanics*, 600:291–337.

[37] Harper-Bourne, M. (1999). Jet near-field noise prediction. In *5th AIAA/CEAS Aeroacoustics Conference and Exhibit*, page 1838.

[38] Huber, J., Drochon, G., Pintado-Peno, A., Cléro, F., and Bodard, G. (2014). Large-scale jet noise testing, reduction and methods validation "EXEJET": 1. project overview and focus on installation. In *20th AIAA/CEAS Aeroacoustics Conference, Atlanta GA, USA*, page 3032.

[39] Ilário, C. R., Azarpeyvand, M., Rosa, V., Self, R. H., and Meneghini, J. R. (2017). Prediction of jet mixing noise with lighthill's acoustic analogy and geometrical acoustics. *The Journal of the Acoustical Society of America*, 141(2):1203–1213.

[40] Karabasov, S. A., Afsar, M. Z., Hynes, T. P., Dowling, A. P., McMullan, W. A., Pokora, C. D., Page, G. J., and McGuirk, J. J. (2010). Jet noise: acoustic analogy informed by large eddy simulation. *AIAA Journal*, 48(7):1312–1325.

[41] Khavaran, A. (1999). Role of anisotropy in turbulent mixing noise. *AIAA Journal*, 37(7):832–841.

[42] Khavaran, A., Kenzakowski, D. C., and Mielke-Fagan, A. F. (2010). Hot jets and sources of jet noise. *International Journal of Aeroacoustics*, 9(4-5):491–532.

[43] Khavaran, A., Krejsa, E. A., and Kim, C. M. (1994). Computation of supersonic jet mixing noise for an axisymmetric convergent-divergent nozzle. *Journal of Aircraft*, 31(3):603–609.

[44] Landau, L. D. and Lifshitz, E. M. (1987). *Fluid Mechanics*. Number vol. 6. Elsevier Science.

[45] Leifsson, L. T. (2005). *Multidisciplinary design optimization of low-noise transport aircraft*. PhD thesis, Virginia Tech.

[46] Lighthill, M. J. (1952). On sound generated aerodynamically I. General theory. *Proceedings of the Royal Society of London. Series A. Mathematical and Physical Sciences*, 211(1107):564–587.

[47] Lilley, G. M. (1958). *On the Noise from Air Jets*. ARC-20376. Aeronautical Research Council.

[48] Lilley, G. M. (1972). The generation and radiation of supersonic jet noise. Vol. IV-Theory of turbulence generated jet noise, noise radiation from upstream sources, and combustion noise. part II: Generation of sound in a mixing region. Technical Report AFAPL-TR-72-53, Air Force Aero Propulsion Laboratory.

[49] Lizarazu, D. and Sengisen, A. (2010). Rearward fan noise installation effects. Intern presentation.

[50] Lyu, B., Dowling, A. P., and Naqavi, I. (2017). Prediction of installed jet noise. *Journal of Fluid Mechanics*, 811:234–268.

[51] Mani, R. G. P. R., Gliebe, P. R., and Balsa, T. F. (1978). High velocity jet noise source location and reduction. *Federal Aviation Administration Report, FAA-RD-76-II*.

[52] Mc Laughlin, P., Self, R., Powles, C., Wrighton, C., Strange, P., and Moore, A. (2008). High frequency jet noise installation effects for an under wing mounted aircraft. In *14th AIAA/CEAS Aeroacoustics Conference (29th AIAA Aeroacoustics Conference)*, page 2997.

[53] Menter, F. R. (1994). Two-equation eddy-viscosity turbulence models for engineering applications. *AIAA Journal*, 32(8):1598–1605.

[54] Michel, U. (2010). Noise reduction by aircraft innovations. German Aerospace Center (DLR).

[55] Miller, S. A. E. (2014). Toward a comprehensive model of jet noise using an acoustic analogy. *AIAA Journal*, 52(10):2143–2164.

[56] Morfey, C. L. and Joseph, P. F. (2001). Shear layer refraction corrections for off-axis sources in a jet flow. *Journal of Sound and Vibration*, 239(4):819–848.

[57] Morris, P. J. and Boluriaan, S. (2004). The prediction of jet noise from CFD data. In *10th AIAA/CEAS Aeroacoustics Conference*, volume 3, pages 2009–2019.

[58] Morris, P. J. and Farassat, F. (2002). Acoustic analogy and alternative theories for jet noise prediction. *AIAA Journal*, 40(4):671–680.

[59] Morse, P. M. and Ingard, K. U. (1968). *Theoretical Acoustics*. Princeton University Press, Princeton, New Jersey.

[60] Paliath, U. and Morris, P. (2004). Prediction of jet noise from circular beveled nozzles. In *11th AIAA/CEAS Aeroacoustics Conference*, page 3096.

[61] Pathak, P., Burnside, W., and Marhefka, R. (1980). A uniform GTD analysis of the diffraction of electromagnetic waves by a smooth convex surface. *IEEE Transactions on Antennas and Propagation*, 28(5):631–642.

[62] Phillips, O. M. (1960). On the generation of sound by supersonic turbulent shear layers. *Journal of Fluid Mechanics*, 9(1):1–28.

[63] Piantanida, S., Jaunet, V., Huber, J., Wolf, W. R., Jordan, P., and Cavalieri, A. V. G. (2016). Scattering of turbulent-jet wavepackets by a swept trailing edge. *The Journal of the Acoustical Society of America*, 140(6):4350–4359.

[64] Pont, G., Brenner, P., Cinnella, P., Maugars, B., and Robinet, J.-C. (2017). Multiple-correction hybrid k-exact schemes for high-order compressible RANS-LES simulations on fully unstructured grids. *Journal of Computational Physics*, 350:45–83.

[65] Powles, C., J. and Tester B., J. (2007). ISVR/AI-F benchmark report: Scattering of sound from a monopole source by a steady cylindrical jet. Technical report, University of Southampton.

[66] Raizada, N. and Morris, P. (2006). Prediction of noise from high speed subsonic jets using an acoustic analogy. In *12th AIAA/CEAS Aeroacoustics Conference (27th AIAA Aeroacoustics Conference)*, page 2596.

[67] Redonnet, S., Manoha, E., and Kenning, O. (2004). Numerical simulation of the downstream fan noise and jet noise of a coaxial jet with a shielding surface. In *10th AIAA/CEAS Aeroacoustics Conference*, page 2991.

[68] Ribner, H. S. (1969). Quadrupole correlations governing the pattern of jet noise. *Journal of Fluid Mechanics*, 38(1):1–24.

[69] Roach, G. F. (1982). *Green's functions*. Cambridge University Press.

[70] Rosa, V. H., Deschamps, C. J., Salazar, J. P., and Ilario da Silva, C. R. (2013). Comparison of RANS-based methods for the prediction of noise emitted by subsonic turbulent jets. In *19th AIAA/CEAS Aeroacoustics Conference*, page 2276.

[71] Self, R. H. (2004). Jet noise prediction using the lighthill acoustic analogy. *Journal of Sound and Vibration*, 275(3-5):757–768.

[72] Self, R. H. (2005). A RANS CFD coupled model for predicting coaxial jet noise. Technical report, University of Southampton.

[73] Self, R. H. and Azarpeyvand, M. (2008). Utilization of turbulent energy transfer rate timescale in aeroacoustics with application to heated jets. *International Journal of Aeroacoustics*, 7(2):83–102.

[74] Semiletov, V. and Karabasov, S. A. (2016). On the properties of fluctuating turbulent stress sources for high-speed jet noise. In *22nd AIAA/CEAS Aeroacoustics Conference*, page 2867.

[75] Stone, M. and Goldbart, P. (2012). *Mathematics for Physics A Guided Tour for Graduate Students*. Cambridge University Press, Cambridge, United Kingdom.

[76] Tam, C. K. W. (2001). On the failure of the acoustic analogy theory to identify the correct noise sources. In *7th AIAA/CEAS Aeroacoustics Conference and Exhibit*, page 2117.

[77] Tam, C. K. W. and Auriault, L. (1998). Mean flow refraction effects on sound radiated from localized sources in a jet. *Journal of Fluid Mechanics*, 370:149–174.

[78] Tam, C. K. W. and Auriault, L. (1999). Jet mixing noise from fine-scale turbulence. *AIAA Journal*, 37(2):145–153.

[79] Tam, C. K. W. and Ganesan, A. (2004). A modified ke turbulence model for calculating the mean flow and noise of hot jets. In *41st Aerospace Sciences Meeting and Exhibit*, page 1064.

[80] Tam, C. K. W., Golebiowski, M., and Seiner, J. M. (1996). On the two components of turbulent mixing noise from supersonic jets. *AIAA Paper*, page 1716.

[81] Tam, C. K. W., Pastouchenko, N. N., and Viswanathan, K. (2005). Fine-scale turbulence noise from hot jets. *AIAA Journal*, 43(8):1675–1683.

[82] Tam, C. K. W., Viswanathan, K., Ahuja, K. K., and Panda, J. (2008). The sources of jet noise: experimental evidence. *Journal of Fluid Mechanics*, 615:253–292.

[83] Viswanathan, K. (2004). Aeroacoustics of hot jets. *Journal of Fluid Mechanics*, 516:39–82.

dernière page de la thèse

AUTORISATION DE SOUTENANCE

Vu les dispositions de l'arrêté du 25 mai 2016,

Vu la demande du directeur de thèse

Monsieur C. BAILLY

et les rapports de

M. G. GHORBANIASL
Professor - Von Vrije Universiteit Brussel - Faculty of Applied Sciences
Department of Mechanical Engineering - Triomflaan 43 - Room TL43/2.08 - B-1050 Brussels
Belgique

et de

M. S. MILLER
Associate Professor - University of Florida - Dept. of Mechanical & Aerospace Engineering
PO Box 116250 Gainesville - FL 32611-6250 - Etats-Unis

Monsieur MARTELET Yann

est autorisé à soutenir une thèse pour l'obtention du grade de **DOCTEUR**

Ecole doctorale MECANIQUE, ENERGETIQUE, GENIE CIVIL ET ACOUSTIQUE

Fait à Ecully, le 27 février 2020

P/Le directeur de l'E.C.L.
Le directeur des Etudes

Service Scolarité

Grégory VIAL